

Louisiana State University

LSU Scholarly Repository

LSU Doctoral Dissertations

Graduate School

12-20-2022

Light-Weight Structural Optimization Through Biomimicry, Machine Learning, and Inverse Design

Adithya Challapalli

Louisiana State University and Agricultural and Mechanical College

Follow this and additional works at: https://repository.lsu.edu/gradschool_dissertations

Recommended Citation

Challapalli, Adithya, "Light-Weight Structural Optimization Through Biomimicry, Machine Learning, and Inverse Design" (2022). *LSU Doctoral Dissertations*. 6030.

https://repository.lsu.edu/gradschool_dissertations/6030

This Dissertation is brought to you for free and open access by the Graduate School at LSU Scholarly Repository. It has been accepted for inclusion in LSU Doctoral Dissertations by an authorized graduate school editor of LSU Scholarly Repository. For more information, please contact gradetd@lsu.edu.

**LIGHT-WEIGHT STRUCTURAL OPTIMIZATION THROUGH BIOMIMICRY,
MACHINE LEARNING AND INVERSE DESIGN**

A Dissertation

Submitted to the Graduate Faculty of the
Louisiana State University and
Agricultural and Mechanical College
in partial fulfillment of the
requirements for the degree of
Doctor of Philosophy

in

The Department of Engineering Science

by
Adithya Challapalli
M. S., University of North Texas, 2015
May 2023

Acknowledgements

I would like to express my sincere gratitude to my advisor, Dr. Guoqiang Li for his guidance and support both in my professional and personal life. His clemency and perseverance aided me to continuously learn from my mistakes and progress throughout my time at LSU. My PhD process along with giving me abundance of knowledge and exposure on diverse topics, taught me the ability to learn and sustain in different situations. My gratitude extends to my advisory committee members for taking their valuable time and suggestions. I also would like to thank all my team members for their support in my research.

Table of Contents

Acknowledgements.....	ii
Abstract.....	iv
Chapter 1. Introduction.....	1
Chapter 2. Light Weight Architectures.....	4
Chapter 3. Biomimicry.....	9
3.1. Buckling capacities analysis of the biomimicry columns.....	11
3.2. Experimental validation.....	12
Chapter 4. Data Driven Artificial Intelligence.....	14
4.1. Machine learning.....	15
4.2. Database formation.....	18
4.3. Fingerprinting.....	21
4.4. Machine learning prediction.....	27
Chapter 5. Optimization.....	38
5.1. Improvisation of biomimicry columns.....	38
5.2. Improvisation of lattice truss unit cells.....	42
Chapter 6. Inverse Design.....	52
6.1. Improvisation for superior load carrying capacity.....	53
6.2. Improvisation of cellular unit architectures for superior energy mitigation.....	62
Chapter 7. Shape Memory Architectures with Record High Recovery Stress.....	76
7.1. Materials and Methods.....	80
7.2. Results.....	101
Chapter 8. Summary.....	111
References.....	115
Vita.....	125

Abstract

In load-bearing lightweight architectures, cellular materials were frequently utilized. While octahedron, tetrahedron, and octet truss lattice truss were built for lightweight architectures with stretching and flexural dominance, it can be believed that new cells could easily be designed that might perform much better than the present ones in terms of mechanical and architectural characteristics. Machine learning-based structure scouting and design improvisation for better mechanical performance is a growing field of study. Additionally, biomimicry—the science of imitating nature's elements—offers people a wealth of resources from which to draw motivation as they work to create a better quality of life.

Here, utilizing machine learning approaches, novel lattice truss unit cellular architectures with enhanced architectural characteristics were designed. An inverse design methodology employing generative adversarial networks is suggested to investigate and improvise the lightweight lattice truss unit cellular architectures. The proposed framework was utilized to identify various lattice truss unit cellular architectures with load carrying capacities 40–120% greater than those of octet unit cells. A further 130–160% raise in buckling load bearing capacity was made possible by substituting porous biomimicry columns for the solid trusses in the lightweight lattice truss unit cellular architectures.

This dissertation's main goal is to investigate various improvisation strategies for creating lightweight architectures, particularly when using data analysis and machine learning methods. Lightweight cellular architectures with thin-walls and lattice truss unit cellular architectures with improved shape memory capabilities were created using the knowledge gleaned from numerous of the research projects mentioned in the preceding paragraphs load-bearing architectures and devices, lightweight architecture with shape memory and with better strength, better stretchability, and better elastic stress recovery are widely desired. As compared to the bulk shape memory polymeric cylinders, the cellular architectures with thin walls show 200% betterer elastic stress recovery that is normalized with respect to base designs. The architectural improvisation of many other additional designs and practical implementation can be accomplished using the inverse design framework.

Chapter 1. Introduction

By using scientific concepts to build and improvise various architectures and equipment, the field of mechanical engineering improves. The architectural design to achieve primal performance and reduce the weights within the established boundary constraints is very vital for the best performance of any construction, in addition to choosing the appropriate material. Regarding comfort, affordability, and safety, architectural improvisation is very crucial. Several mathematical models are developed and are being continuously proposed for the understanding and improvisation of architectures from simple 1D and 2D geometrical shapes to complex 3D architectures. Computer-aided design, numerical simulation, and computer-based improvisation approaches have developed to advance and simplify these procedures in all engineering disciplines, even though traditional mathematical models are not always simple to understand. In numerous mathematical models, the advent of finite element methods made it easier to solve differential equations.

To address the progress in this area, several reviews on the historical and contemporary architectural improvisation strategies are routinely published [1-4]. Early in the 1960s, computer-aided designs attracted a lot of interest as researchers looked at the benefits of lightweight buildings [2]. It has been suggested to use homogenization strategies to analyze material models with microscale porosity and attain the best porosity while still having the necessary architectural qualities [3]. The architectural design of light weight buildings is accomplished by mimicking the naturally existing porous architectures like plant stalks, bones, and seashells [4]. In-depth research is being done on the use of new practices like machine learning, deep learning, and other statistical artificial intelligence approaches for the synthesis of novel chemicals, metals and polymeric materials, medicinal, and electrical devices in addition to architectural improvisation [5-8].

In this dissertation, as the title suggests, the focus is to develop and apply novel strategies like machine learning and biomimicry to improvise light weight architectures for better architectural characteristics such as buckling and compression strengths, shock mitigation and shape memory characteristics [9-12]. Lattice cored sandwich architectures, which are lightweight, are frequently utilized in load-bearing engineering designs like car hulls, airplane

wings and fuselages, wind turbine blades, bridge decks, offshore oil platforms, etc. Lattice truss unit cellular architectures are stacked one on top of the other in any arrangement to create a lattice structure. The design of the lattice unit cellular that makes up a lattice structure determines how well it performs as a whole [13]. Biomimicry cellular architectures developed from natural components, such as hexagonal honeycombs, plant stalks, muscles, beetle wings, etc., are intensively researched for their outstanding stiffness, strength, and energy mitigation capacities [12]. The development of additively manufacturing has made it possible to construct lattice core with extremely complicated geometrical configurations. The improvisation of these unit cells is therefore necessary to further raise the lightweight structure's ability to carry loads.

The topology improvisation approach was utilized to suggest new topologies and further improvise existing unit cells. This method iteratively improves a previously usable unit cellular for superior performance by maintaining a fixed relative density throughout [14]. To plan and naturally produce bracket architectures under unambiguous limit conditions, enhancement strategies were made [15]. Even though lattice truss unit cellular architectures have been improvised using normal topology improvisation, it can be challenging to create and improvise lattice truss architectures given the limitations of the structure. This is because it codes using a sophisticated genetic algorithm with two stages. Because it relies on mass reduction to create the best architectures, it may disregard those that demonstrate significant strength enhancements with relatively few mass raises. When evaluating compound iterations, optimizing a structure requires multiple iterations, each of which necessitates analyzing the new structure with auxiliary software, making the process time-consuming, laborious, and computationally intensive. Additionally, topology improvisation only permits the production of a small number of improvised architectures in comparison to a particular reference design. As potential solutions to this issue, data-based improvisation, and inverse design methods like machine learning prediction, GANs, and correlation analysis may be investigated. In order to enhance the mechanical and architectural characteristics of lightweight columns and cellular architectures, a number of these strategies are utilized here.

The following chapters will go into detail on biomimicry architectures, light weight cellular architectures, and data-driven artificial intelligence methods like machine learning prediction

and GANs. Later, it will be explored how to improvise a variety of lightweight architectures using inverse design for superior mechanical characteristics like buckling, compression strength, natural frequency, energy mitigation, and elastic stress recovery in SMP (shape memory polymers). Even though lattice truss unit cellular architectures have been improvised using normal topology improvisation, it can be challenging to create and improvise lattice truss architectures given the limitations of the structure. An overview of the observations, conclusions, and suggested courses of action based on the findings is then given.

Chapter 2. Light Weight Architectures

Lightweight architectures are porous, sufficiently rigid, and robust materials, such as closed and open cell foams [16]. The lattice truss architectures, which are made by interconnecting different truss elements in three dimensions, are one type of open cell foam. Stretching and flexural dominated architectures can be identified based on the quantity of truss components and points in these architectures. While predominantly flexural in nature's elements architectures fail by the flexural or buckling of the trusses, predominantly stretching in nature's elements architectures fail through the stretching of the truss parts [16]. The design criteria and choice of lattice truss architectures are influenced by the mode of failure; predominantly stretching in nature's elements architectures are better suited for load carrying practical implementation and predominantly flexural in nature's elements architectures are better suited for shock mitigation practical implementation. The closed-cell foams are irregular foam-like architectures or cellular architectures with thin walls, like hexagonal honeycombs. These architectures break down completely, either by buckling, flexural, or rupture. These architectures were the subject of numerous studies to investigate their behavior, fabrication methods, and uses. For examples of different light-weight construction designs, see fig. 1.

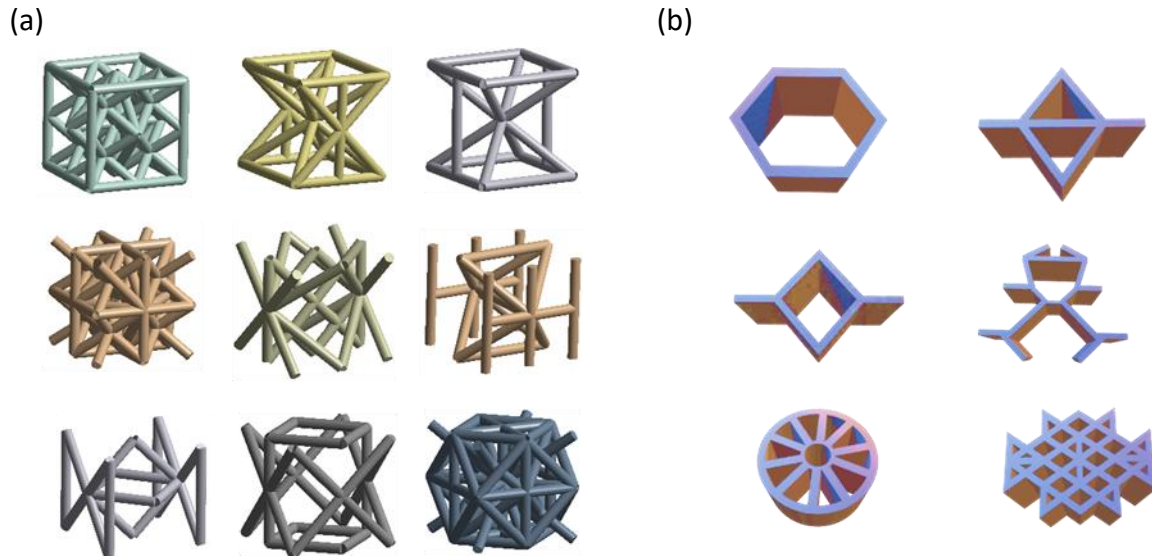


Figure 1. Lightweight (a) lattice, (b) thin-walled architectures.

Lattice truss unit cellular architectures with betterer performance and several benefits in the architectural, thermal, impact, vibrational, and acoustic domains were proposed [17–21]. Among predominantly stretching in nature's elements lattice truss unit cellular architectures, the octet truss lattice structure ranks among the best truss-based lattice architectures [18]. Gyroid and double gyroid architectures created using additive printing demonstrated reasonable impact mitigation capabilities and an added advantage with the same rigidity in both axial directions [19]. For improved energy mitigation, hollow micro truss lattice architectures have been investigated [20]. Betterer damping performance hybrid sandwich panels were created using pyramid truss architectures as the core [21]. Various computational and experimental studies were performed by multiple groups to support the recommended architectures. The linear and nonlinear characteristics of lattice truss architectures were investigated using continuum theory models [18, 22–25]. The octet truss lattice cell's practical FEA tires were initially studied by Deshpande and Fleck. Lattice cored sandwich structure manufacturing strategies and architectural performance were studied by several groups [26–29]. The production of titanium-cored, bio-inspired kagome sandwich panels using selective laser melting (SLM). These sandwich architectures outperform hexagonal honeycomb aerospace core constructions in terms of compressive and shear qualities, as has been demonstrated [26]. Photopolymerization or SLA is used to print and co-cure a number of lattice core sandwich structures manufactured from epoxy-based photopolymer resin and carbon fiber reinforced sandwich plates made as face sheets. Compressive and flexural characteristics of the sandwich constructions were evaluated [27]. Graded lattice core sandwich architectures that produce least weight sandwich architectures are assessed for their flexural response [28]. Sandwich cells made of CFRP with a tetrahedral core were created using silicon rubber molds, and their compressive and shear strengths were evaluated [29].

It is well known that the lightweight lattice truss core in sandwich architectures contributes significantly to the sandwich's overall load carrying capability. The development of additively manufacturing has made it possible to construct lattice core with extremely complicated geometrical configurations. The following is a list of factors that affect the acoustic performance of acoustic insulation A archetype for the modulus of cellular architectures was

created by Gibson and Ashby [30] based on the linear-elastic characteristics at varying relative specific densities:

$$\frac{E^*}{E_s} = c_1 \left(\frac{\rho^*}{\rho_s} \right)^2 \quad (1)$$

$\frac{E^*}{E_s}$ is the unit cellular's relative density, E^* is the porous structure's elastic modulus, E_s is

the base material's elastic modulus, and c_1 is the geometric constant of proportionality that may be calculated from the experimental results. The c_1 value for the octet unit cellular is determined to be 0.09 based on the results of the experiments at different densities, as shown in Fig. 2. (see Fig. 2)

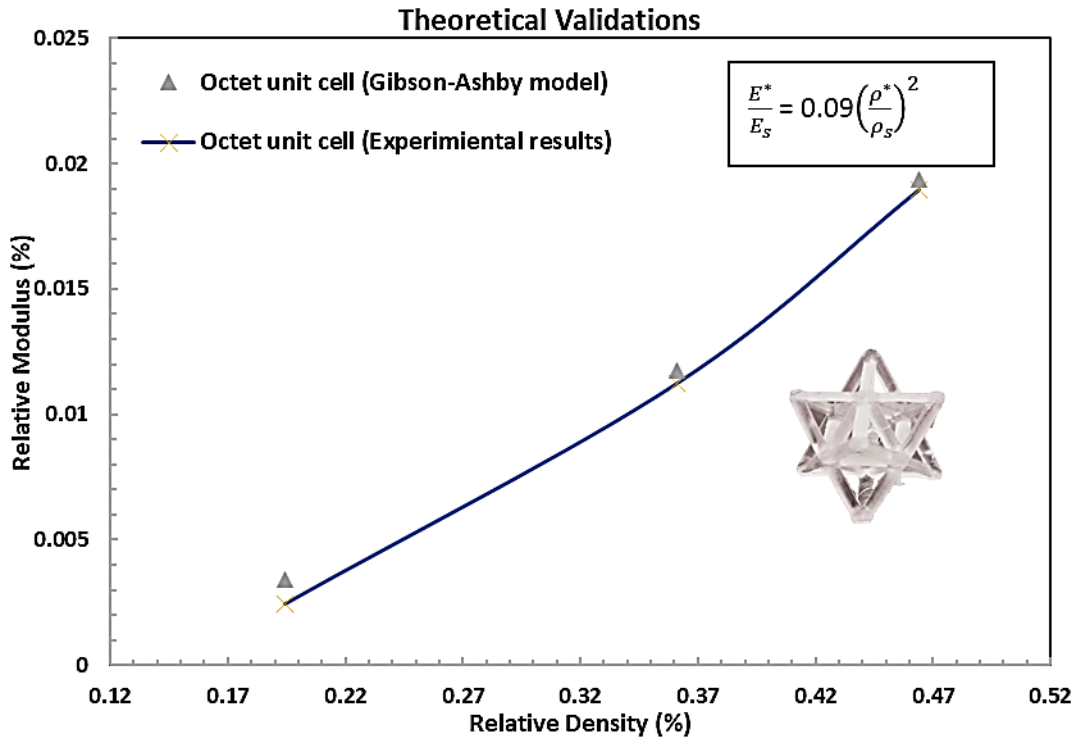


Figure 2. Gibson-Ashby archetype evaluations.

Biomimicry cellular architectures with thin walls, such as hexagonal honeycombs, plant stalks, bones, muscles, beetle wings, etc., are widely studied for their outstanding particular stiffness, strength, and energy mitigation FEA tires [30–36]. Hexagon-shaped cellular architectures that were based on hexagonal honeycombs have been the subject of several research and refinements [31]. The stalks of several plant species, such as bamboo, rice, and

square stalks, served as motivation for the construction of cylindrical columns which have buckling capacities seven times more than solid columns and hollow cylinders [32, 33]. The creation of rigid, thin-walled carbon fiber reinforced polymer (CFRP) tubes that are reinforced by foam cylinders resembles the luffa sponge's that consists of a hierarchical structure that is bio-cellular different densities of micro and macro holes [34]. The inner architectures of tabular bones and muscles served as motivation for the design of energy-absorbing and impact-resistant tubular sections, which demonstrated a 176% improvement in energy mitigation for the third level hierarchy compared to the first order [35, 36]. The invention of trabecular hexagonal honeycomb architectures, which surpass ordinary quadrilateral tubes used in the crash box beams of current gadgets and vehicles by a factor of five, was inspired by the Beetle Electra's more effective energy-absorbing qualities [37]. It is thought that the secret lies in the frequency improvisation of macroscale architectures factor in preventing harmful responses [38].

According to research, the Hooke's law-based computational homogeneous strategy (CHT) may be used to calibrate the useful characteristics of cellular architectures. The generalized Hooke's law based on the CMT may be used to determine the stiffness matrix of cellular unit architectures. In this work, a twofold rotational symmetry is included into each unit cell. As a result, Hook's law will look like this:

$$\begin{pmatrix} \bar{\sigma}_{11} \\ \bar{\sigma}_{22} \\ \sigma_{33} \\ \bar{\sigma}_{23} \\ \bar{\sigma}_{13} \\ \bar{\sigma}_{12} \end{pmatrix} = \begin{pmatrix} C_{11} & C_{12} & C_{13} & 0 & 0 & 0 \\ C_{21} & C_{22} & C_{23} & 0 & 0 & 0 \\ C_{31} & C_{32} & C_{33} & 0 & 0 & 0 \\ 0 & 0 & 0 & C_{44} & 0 & 0 \\ 0 & 0 & 0 & 0 & C_{55} & 0 \\ 0 & 0 & 0 & 0 & 0 & C_{66} \end{pmatrix} \begin{pmatrix} \bar{\varepsilon}_{11} \\ \bar{\varepsilon}_{22} \\ \bar{\varepsilon}_{33} \\ \bar{\gamma}_{23} \\ \bar{\gamma}_{13} \\ \bar{\gamma}_{12} \end{pmatrix}, C_{ij} = C_{ji} \text{ and } \bar{\gamma} = 2\bar{\varepsilon} \quad (2)$$

Here $\bar{\sigma}$ and $\bar{\varepsilon}$ are cellular unit's corresponding stress tensors, respectively. Using six boundary conditions—three uniaxial compressions and three shear deformations—and one non-zero component of the strain tensor, it is possible to determine the effective stiffness matrix of each unit cellular.

$$C_{11} = \frac{\bar{\sigma}_{11}}{\bar{\varepsilon}_{11}}, C_{21} = \frac{\bar{\sigma}_{22}}{\bar{\varepsilon}_{11}}, C_{31} = \frac{\bar{\sigma}_{33}}{\bar{\varepsilon}_{11}}, \text{ where } \bar{\varepsilon}_{11} \neq 0;$$

$$C_{22} = \frac{\bar{\sigma}_{22}}{\bar{\varepsilon}_{22}}, C_{23} = \frac{\bar{\sigma}_{33}}{\bar{\varepsilon}_{22}}, \text{ where } \bar{\varepsilon}_{22} \neq 0; C_{33} = \frac{\bar{\sigma}_{33}}{\bar{\varepsilon}_{33}}, \text{ where } \bar{\varepsilon}_{33} \neq 0; \quad (3)$$

$$C_{44} = \frac{\bar{\sigma}_{23}}{\bar{\gamma}_{23}}, \text{ where } \bar{\gamma}_{23} \neq 0; C_{55} = \frac{\bar{\sigma}_{13}}{\bar{\gamma}_{13}}, \text{ where } \bar{\gamma}_{13} \neq 0; C_{66} = \frac{\bar{\sigma}_{12}}{\bar{\gamma}_{12}}, \text{ where } \bar{\gamma}_{12} \neq 0;$$

The aforementioned archetype shows that the shape of each individual unit cellular determines the stiffness qualities of the cellular unit architectures as

$$\bar{\sigma}_{ij} = \frac{\sum F_{ij}}{A} \quad (4)$$

where F_{ij} = c force,

$A = c/s$ area.

Chapter 3. Biomimicry

Biomimicry is the study of imitating natural processes, components, and architectures to create or improve artificial counterparts with greater functionality. It took millions of years for our nature's elements to evolve, develop, and become what it is now. Nature's elements adjust its components through evolution so they can survive, grow, and prosper in their surroundings. Over the course of hundreds and millions of years, several species have steadily changed and evolved. By copying nature's elements, greater materials, models, and buildings can be created that would be impossible for humans to create on their own. The imitation of nature's elements has contributed significantly to many areas of engineering, including the manufacture of novel materials, architectural design, robotics, textiles, electronic gadgets, artificial muscles, etc. [41]. It is important to remember that artificial neural networks, a key component of many machine learning models, are modeled after how the human brain works. In architectural biomimicry, hexagonal honeycombs RVE as a motivation for the cellular cored sandwich architectures that have been intensively explored for their low weight, superior load carrying, and energy mitigation capabilities [42]. Armadillo and fish skin are utilized to create multi-layered body armors [43, 44]. The biology of plants has been the subject of numerous studies to comprehend and emulate specific FEA in producing innovative technologies that outperform traditional synthetic products. To further focus the literature, this section focuses on plant-based biomimicry practical implementation.

One of the oldest and most important natural groups on Earth, the plant kingdom governs and sustains a wide range of other organisms and ecological processes. Plant species educate humanity in a variety of scientific and research areas through slow yet careful evolution. Humans were able to better understand the Earth's environment, develop agriculture, establish civilizations, and build technology after the stone age by observing nature's elements and the evolution of plants. To create and develop their tools, humans have borrowed ideas from and replicated elements of nature's elements.

Water plants like the lotus have the ability to clean themselves, which is one application of plant-based biomimicry. In order to create façade paints, tiles, self-cleaning glasses, and places where hydro-degradation occurs, the extreme hydrophobicity of lotus blooms has been imitated

[45, 46]. The fluid motion of plants and the light energy they store via photosynthesis have served as motivation for the development of biohybrid models like microfluidic devices [47, 48]. Another source of motivation for the design of textiles is the flow of liquids and waters within plants, which serve as representational volume elements. To improve comfort in humid conditions, moisture-management materials can transfer sweat-generated water to the fabric's outside surface. Since plant architectures are mimicked, these textiles are more successfully created than conventional fabrics [49]. George de Mestral was inspired to develop Velcro by the hooks on plant burrs [50]. Pummelo is used as motivation to build buildings with decent damping characteristics [51]. A thick layer of skin made up of porous layers surrounds the flesh of this fruit. The fruit's skin shields it from impact injury as it falls to the ground. These characteristics of the fruit were observed and imitated to produce metallic foam cells that were light in weight and had excellent damping characteristics. It is also popular to use plant biomimicry in architectural design. The beautiful shapes of flowers like lilies and plant cells have been used as motivation for furniture design [52]. The use of bamboo, which is thought of as a strong composite material, is being investigated for constructions with larger architectural capacity. As a usage in creating engineered composite materials, the helical reinforcing of bamboo fibers is researched [53]. The tendril structure of plants has been replicated by creating polymeric artificial muscles by adding twists to precursor fibers [54, 55]. SEM was used to study the microscale surfaces of hydrophobic plants in order to better understand how they self-clean.

A major mode of failure for thin columns or columns under axial compressive buckling. It is important to avoid this kind of failure mode when designing architectural elements so that the materials' full load-bearing capability can be utilized. The geometrical shape of columns or columns is traditionally improvised; for example, drum-shaped columns have larger buckling loads than homogeneous cylinders [56]. The reason hollow or porous columns typically have betterer buckling load bearing capacity than solid columns with the same quantity of material is that the materials around the rod axis do not offer significant flexural load bearing capacity. Plant stalk and roots typically have porous architectures, as was previously mentioned. It may therefore be possible to create artificial columns or columns with greater buckling load bearing capacity by modeling their porous architectures. See a schematic of a porous structure in Fig. 3

on the left. In addition to animals' quills, seashells, and hexagonal honeycombs, plants frequently have porous architectures. These organic shapes can be idealized as the biomimetic architectures seen on Figure 3's right side. According to our understanding of the phenomena, these porous architectures are decent candidates for the creation of biomimicry columns with improved buckling load bearing capability. Based on biological architectures, improved buckling-resistant columns or columns are designed and tested.

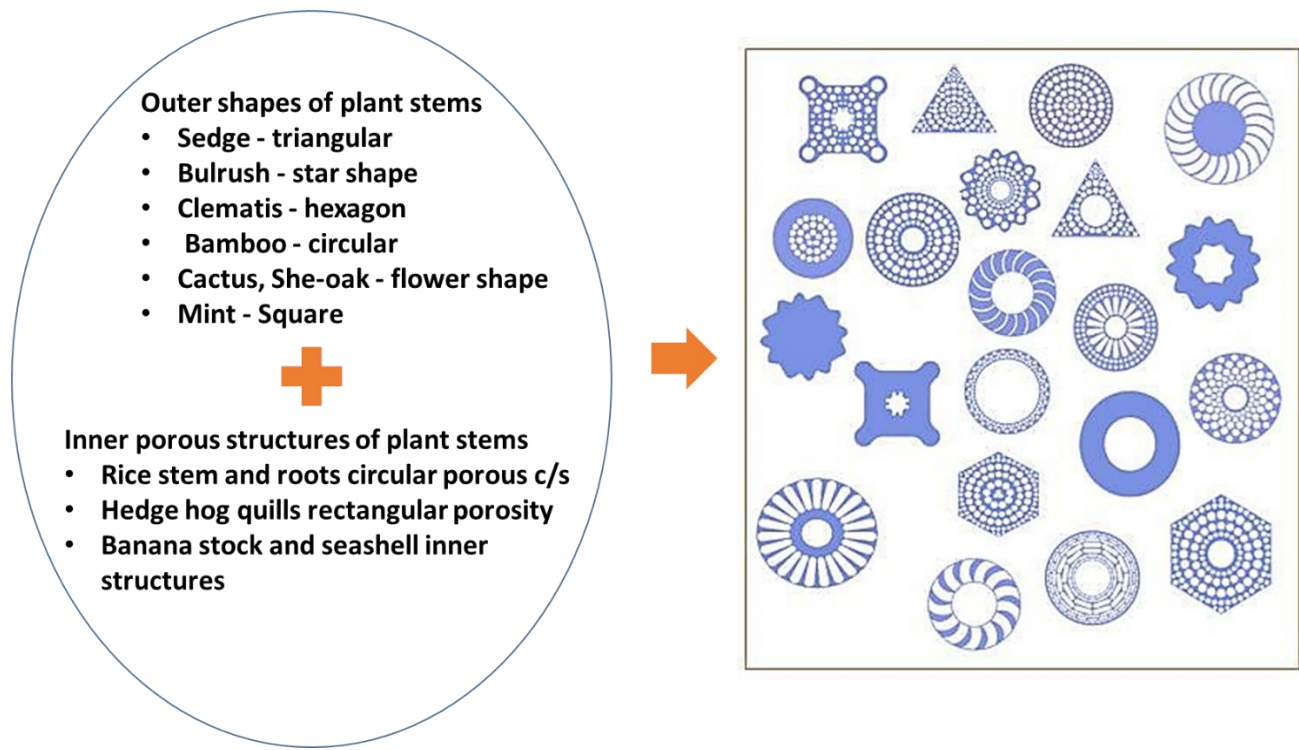


Figure 3. Schematic of biomimicry architectures learned from the nature's elements.

3.1. Buckling capacity analysis of the biomimicry columns

For several sample biomimicry columns, Figure 4 shows the mass vs. normalized buckling capacity, compressive stress, and axial deformation during stress and buckling analysis. For all designs, the overall volume remains constant. As can be shown in Fig. 4A, the biomimicry columns' normalized buckling capacities are more than twice as decent as those of solid and hollow columns of equal mass. As a consequence, the biomimicry columns show a notable improvement in buckling load bearing capability. According to Fig. 4B, when two biomimicry columns have the same mass, their peak compressive stress is comparable to that of a solid rod.

It is understood that biomimicry columns can be extremely light, and their maximal compressive stress is better. Even the stress in the lightest rod, however, is far lower than the compression strength of the polymer [9] as compared to strength. Compressive failure is thus prevented. Compressive stress is representative volume element to have a same tendency in terms of the axial deformation designed by stress analysis, indicating that biomimicry columns with the same mass display the same axial deformation to control solid and hollow columns. The interior porous structure and external form of the biomimicry columns have a substantial impact on the buckling load, as seen in Fig. 4. As shown in Fig. 2A, bamboo stalks with a circular outer form are significantly inferior to cactus and square-shaped stalks. It is crucial to remember that all of these columns mimic the basic xylem-based stalk cross-sections, with the exception of roots, which are entirely porous (hollow cylinders). The inner radii of these columns can be improvements to improvement the load-bearing capability of the constructions against buckling.

3.2. Experimental validation

Fig. 5 compares the normalized buckling loads of the 3D printed biomimicry columns and the columns from FEA simulations. It can be observed from the RVE that the modeling findings and the experimental results are consistent. The compromise in additively manufacturing catalyzed by low printing resolution is the main reason for the modest variation among the experimental results and the simulated results. It should be mentioned that the simulations' rod boundary conditions were modified to match the circumstances of the experiments. Consequently, the FEA is verified.

One drawback in this study is with the additive manufacturing of the optimized biomimetic rods. Since the rods have several porous elements within them and also the porosity due to the density is high, it is hard to include all the feature while 3D printing. This is due to the complexity in the designs, 3D printing system in use, material, and printing time. If a better additive manufacturing technique can be used, or a machine with higher resolution and less time requirement for the additive manufacturing process this could lead to much better replication of the optimized rods. Nevertheless, the results presented below can be taken as good representation of the study as the designs carry majority of the recommendations.

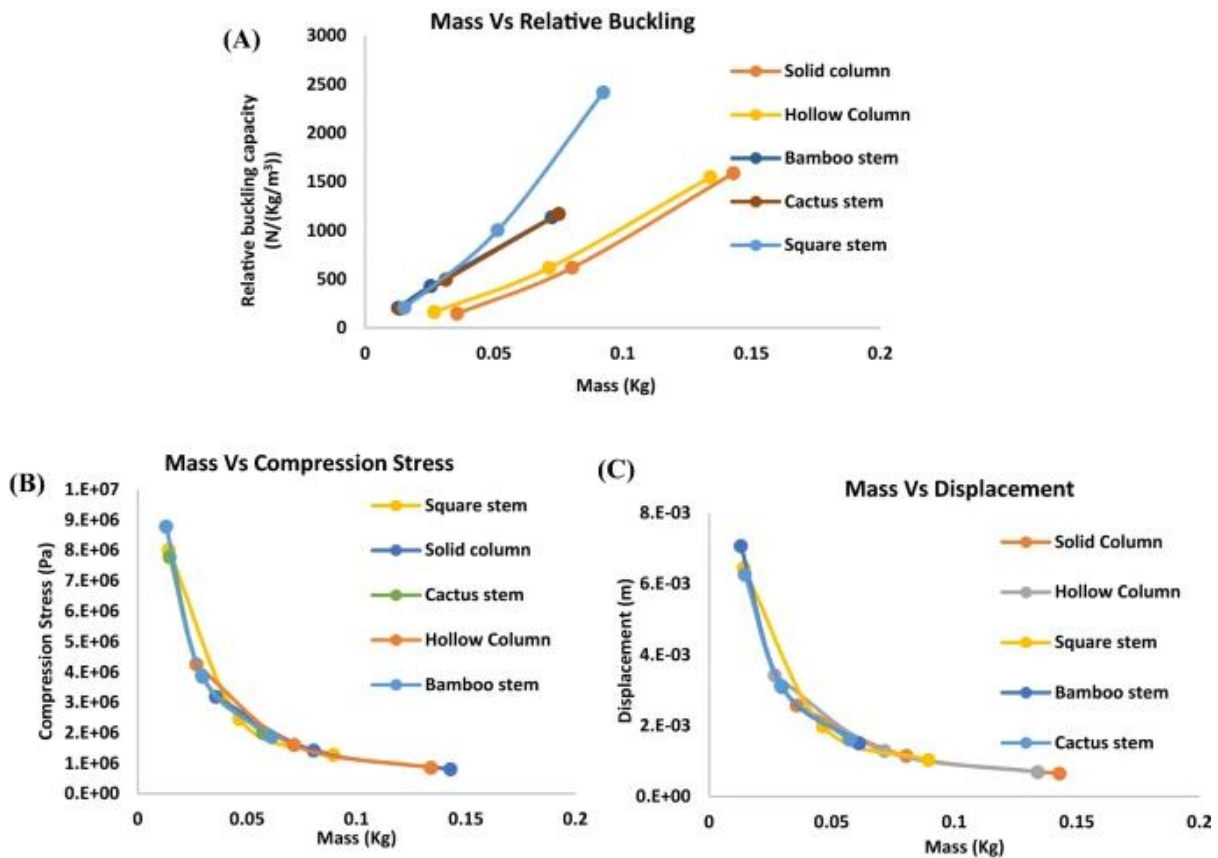


Figure 4. (A) normalized buckling capacity, (B) compressive stress, and (C) axial deformation, respectively with respect to mass.

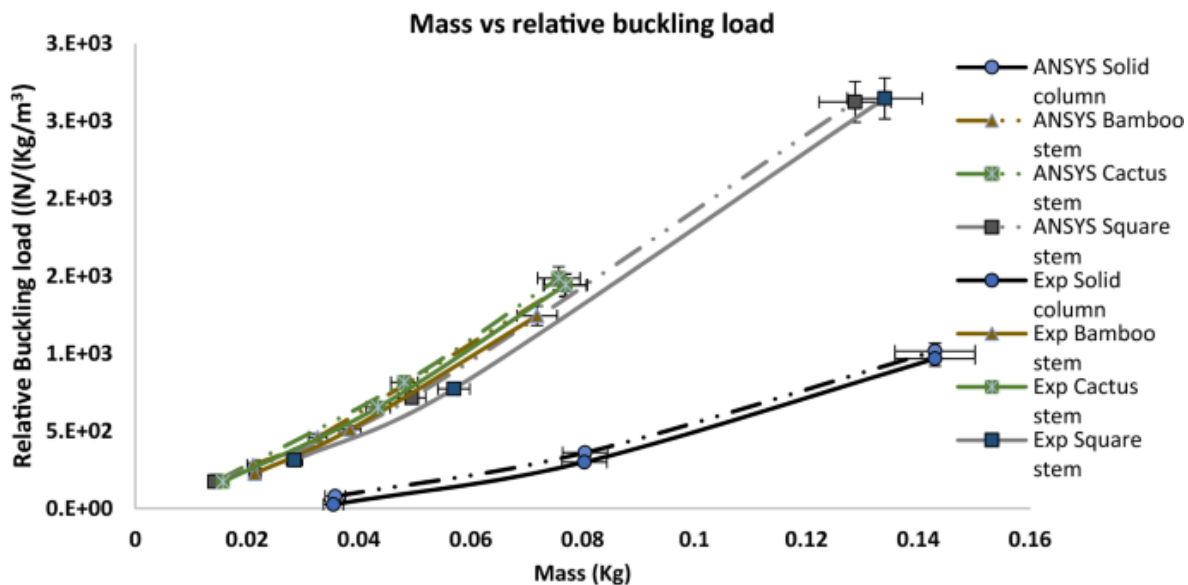


Figure 5. Experimental validation for 3D printed rods.

Chapter 4. Data Driven Artificial Intelligence

When building the biomimicry columns that are discussed in the third chapter, it was designed that there are some drawbacks to directly copying architectures to achieve the best designs. First, manually designing, analyzing, and comparing all potential designs is extremely taxing and not primal. Second, even if the designs allow for the deduction of an ideal set of architectures, it is thought that even better designs with betterer architectural capacities exist. Combining these biomimicry designs also makes it hard to investigate all conceivable architectures or the structure design space. To find the best columns, a design improvisation strategy should be utilized.

The development of additively manufacturing technology and sophisticated design tools has made it possible to manufacture lattice cores with extremely complex geometrical configurations, even though several lattice truss unit cells and cellular architectures with thin walls have been proposed with various practical implementation. Lattice core innovation is therefore necessary to further improvement the load bearing capability of lattice cored sandwiches. There is thought to be a sizable uncharted area of cellular architectures that can outperform their biomimicry equivalents.

Numerous groups have proposed new architectures while optimizing the lattice truss unit cellular architectures that already exist. By maintaining a fixed relative density throughout, this approach iteratively improved a previously usable unit cellular for betterer performance [57]. By employing this strategy, the researchers were able to produce novel optimal lattice truss unit cellular architectures (ORC, OQSO) that were 5% and 38% stiffer than octet truss lattice truss unit cellular architectures in the usual (001) direction [57]. To compensate for the constituents of the octet truss lattice unit cellular' s elastic anisotropic character, researchers produced elastically isotropic unit cells by combining a variety of fundamental unit cells, including the simple cubic unit cellular, the octet unit cellular, etc. [58]. By using an inverse improvisation strategy, Messner [59] improved an iso-truss lattice, which demonstrated a 50% raise in stiffness over the octet truss lattice. Yang and Li [60] created a cuttlebone-like lattice utilizing topology improvisation and showed that the new lattice had 141.96% raise in relative collapse strength as compared to octet truss lattice. A uniform octet-truss lattice structure's density distribution and macro

topology were both improvised by Yang et al (61). 's multiscale fuzzy improvisation (FO) approach. Nasrullah et al. [62] demonstrated that the octet truss lattice has the highest crashworthiness, and following topological improvisation showed that twisted lattice truss architectures with 20% relative density may generate the better specific energy mitigation. All the trusses under discussion behave similarly, according to Watts [63], with anisotropic trusses yielding stronger architectures for a given load. To discover the stiffest possible multiscale architectures constructed of micro-architected materials, he used topological improvisation. A multi-objective genetic algorithm with Kriging support was used by Song et al. [64] to build the biggest specific modulus octet-truss (OCT) cellular materials. They intended for a further improvement in weight bearing capacity to be possible by optimizing the sizes of OCT. In addition to biomimicry existing cellular architectures like the hexagonal honeycomb, topology improvisation has been extensively used to suggest and improvise specific cellular designs for greater performance in various practical implementation (65-67). Using a multiscale topology improvisation approach, greater natural frequency inhomogeneous cellular materials are created (68).

Although lattice truss unit cellular architectures have been improved using standard topology improvisation, developing, and optimizing cellular architectures under the given architectural boundary conditions or restrictions may be challenging. This is because it employs an advanced two-stage genetic algorithm. The best constructions are produced using this method, which may overlook those that exhibit a substantial improvement in strength with little mass boosts. Multiple iterations are required to improvise a structure, and each iteration requires analyzing the new structure using auxiliary software, which makes the procedure complicated, time-consuming, and computationally intensive, especially when evaluating compound iterations.

4.1. Machine learning

Machine learning is the branch of computer science and an artificial intelligence that utilizes data to automatically learn through experience. Models can be taught to learn from the data provided via machine learning, and these models can then be utilized to predict or categorize additional untrained data. Reduced human involvement, complex programming, and computation time are all huge benefits. Unsupervised learning and supervised learning are the

two formal contexts in which machine learning may be understood. Learning under supervision necessitates data with known input and output values. Unsupervised learning, on the other hand, uses inputs without labels. The data utilized in this dissertation include inputs such as architectural characteristics like mass, volume, and structure as well as outputs such as the intended mechanical qualities.

To predict the mass, load, and natural frequency of each cellular unit, for instance, a variety of machine learning strategies were used. Support vector regression models were used to estimate the mass values of the cellular architectures (SVM). The SVM archetype looks for the best hyperplane that fits under a particular threshold value rather than seeking to minimize the difference between actual and predicted values. The MATLAB toolbox implements the built-in linear epsilon insensitive SVM (SVM) regression. The objective of this archetype is to find a function $f(x)$ such that the observed response values (y_n) do not deviate by more than for each training point x . SVM forecasts new values using the following function (89):

$$f(x) = \sum_{n=1}^N (a_n - a_n^*) (x_n \cdot x) + b \quad (5)$$

where N = number of observations,

x_n = set of observation,

n = observations,

a_n, a_n^* = non-negative multiplier for observations x_n .

To predict the load and natural frequency, a kernel-based probabilistic archetype known as Gaussian Process Regression (GPR) is used. To get the response, the GPR models employ a set of random latent variables for which any finite number of them have a Gaussian distribution. The GPR archetype serves the following purposes (90):

$$P(y_n|f(x_n), x_n) \sim N(y|h(x_n)^T \beta + f(x_n), \sigma^2) \quad (6)$$

where y_n = response variables,

$f(x_n)$ = zero mean, $k(x, x')$,

$h(x_n)^T$ = transformation function from the original FEA true vectors into new FEA true vectors,

σ^2, β = error variance and coefficients, respectively.

Numerous technical practical implementations, such as the identification of novel polymers, compounds, and architectures, make extensive use of machine learning [69–72]. Machine learning strategies such as forward regression and classification have been applied in the fields of material, medical, chemical, and architectural engineering, replacing labor-intensive simulations and experimental comparisons that are expensive and time-consuming. The search for novel thermoset shape memory polymers with improved elastic stress recovery has been aided by the use of convolutional neural networks (CNN) and other machine learning strategies [72]. Kernel Ridge Regression (KRR) has been used in the property assessments of polymers to control non-linear correlations and give a material design process that hastens the discovery of novel polymers [73]. According to research, Gaussian Process Regression (GPR) is better suited to forecasting the uncertainty and confidence intervals of polymers and their characteristics [74]. Other machine learning methods, such as Gradient Boosting Algorithms, Decision Trees, and K-nearest Neighbors, have also been shown to be better accurate at predicting FEA tires [74]. With an average discrepancy of 0.492%, neural networks are used to simulate the stress distributions in the aorta wall based on the findings of FEA (FEA) [75].

Support vector regression models are used to imply a direct link between the input and output of the components. This eliminates the requirement for challenging numerical iterations and allows for the creation of the internal deformation field [76]. Gaussian Process Regression (GPR) has been used by the same group, and they have come to the conclusion that it is more suitable for predicting a better uncertain/confidence interval of polymers and their characteristics [77]. Support vector machines (SVM), which are regarded as being especially effective in real value function estimation, have been used to forecast the mechanical and architectural characteristics of cement [78, 79]. Regression trees have been used to predict the mechanical characteristics of carbon fibers, such as the longitudinal and transverse elastic modulus and shear modulus, using data from finite element modeling [80]. Support vector regression models have been applied in order to create FEA models that can clearly identify a relationship between the input and output of the components. This eliminates the requirement for challenging numerical iterations and allows for the construction of the internal deformation field [81]. Ensemble approaches have been used to characterize the bio-mechanical behavior of

breast tissues under compressive forces using the results of FEA models [82]. Machine learning is utilized in the design of auxetic complex structures to avoid heavy computational and analytical workload [83]. Neural networks and inverse design methods are utilized to create spinodal complex structures with raised anisotropic stiffness [84]. Neural networks were also used to build and modify 3D chiral metamaterial with high chiroptical response, avoiding time-consuming numerical calculations [85]. To implement machine learning, numerous factors including creating the data, data filtering, fingerprinting the data, archetype training and execution are necessary. The use of machine learning to forecast the buckling characteristics of biomimicry columns, the compression strength of lattice truss unit cells, and the natural frequencies of thin-walled cellular unit architectures will be discussed in the parts that follow.

4.2. Database formation

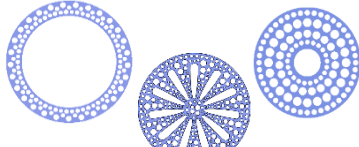
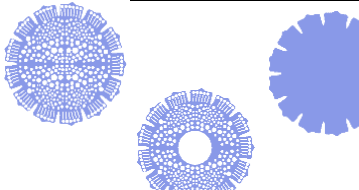
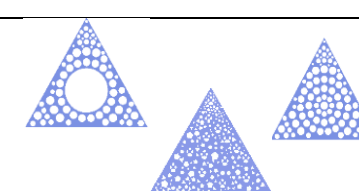
4.2.1. Biomimicry columns

The biomimicry columns developed in this study are depicted on the right side of Figure 3 and combine the exterior shape (upper left) and interior microstructure (bottom left) of their biological counterparts. There are 21 fundamental biomimicry columns that were made from the schematics in Fig. 3's right-hand corner. The external stalk forms of the rice plant, bamboo, cactus, square (mint, cup plant), bulrush, papyrus, and she-oak plants, as well as the interior porous architectures of the roots, hedgehog quills, seashells, and she-oak plants, were combined to produce the biomimicry columns. But for machine learning, 21 columns are not enough. A total of 1500 columns were produced for modeling in this experiment. Based on the 21 fundamental columns, these extra columns were made by altering the columns' pore positions, size distributions, and shapes, among other things. Table 1 lists the quantity of extra columns produced for each group.

The biomimicry columns were grouped into seven categories in Table 1 based on their external forms. Each rod or column was 10 cm tall and had an identical overall volume (volume of the solid substance + volume of the pores). A round rod with a diameter of 1 cm was used to determine the volume, which was 7.85 cm³. As control columns for comparison, solid and hollow cylinders with an inner diameter of 0.5 cm and an outside diameter of 1 cm were used. In addition

to the 1 cm outside diameter for both solid and hollow columns, two additional outside sizes of 1.5 cm and 2.0 cm were also tested, for a total of 6 control columns.

Table 1. Biomimicry columns database

External shape	Primary designs	Extended Database (a total of 1,500)
Bamboo, rice		91 dummy columns
Square plant		81 dummy columns
Bulrush		71 dummy columns
Cactus		81 dummy columns
She-oak		50 dummy columns
Sedge		50 dummy columns

4.2.2. Lattice unit cellular data formation

It is crucial to establish specific boundary conditions for the method's consistent execution in order to generate every FEAable combination of lattice truss unit cell architectures. Here, we take a cuboid with 27 points (Fig. 6(a)) into consideration. This cuboid may be broken

into eight symmetric little cubes, each of which has eight points on the edges. Single truss elements may be created by joining every point to its neighbor, and multiple truss elements can be combined to create a wide variety of 2D isotropic and anisotropic lattice truss unit cell architectures. This complete cube's one by eight can be viewed as an RVE (Fig. 6(b)) to produce every symmetric lattice unit cellular that is conceivable. This decreases the complexity of managing data and simplifies the data size while conserving computer capacity.

To construct the full lattice unit cellular, spin the one by eight cube into each of the final seven mirror images. Other anisotropic combinations, including stretching and predominantly flexural in nature's elements lattice cells, can be produced using the complete cube's (27 points) RVE to create architectures that might be the best under direction-dependent loading situations. When building the training database using ANSYS workbench, a constant truss diameter, material specifications, meshing size, and boundary conditions are established for all the fingerprints or all the lattice truss architectures for consistency's sake. The RVE is used to produce all possible combinations using the MATLAB function "combnk" for combination enumeration. There are 176 different components that may be constructed inside the RVE. Lattice truss unit cellular architectures and a number of specific patterns are formed to cover constructions with somewhere between 4 and all 176 parts. Thus, a large design space with around a million different lattice unit cellular patterns can be created.

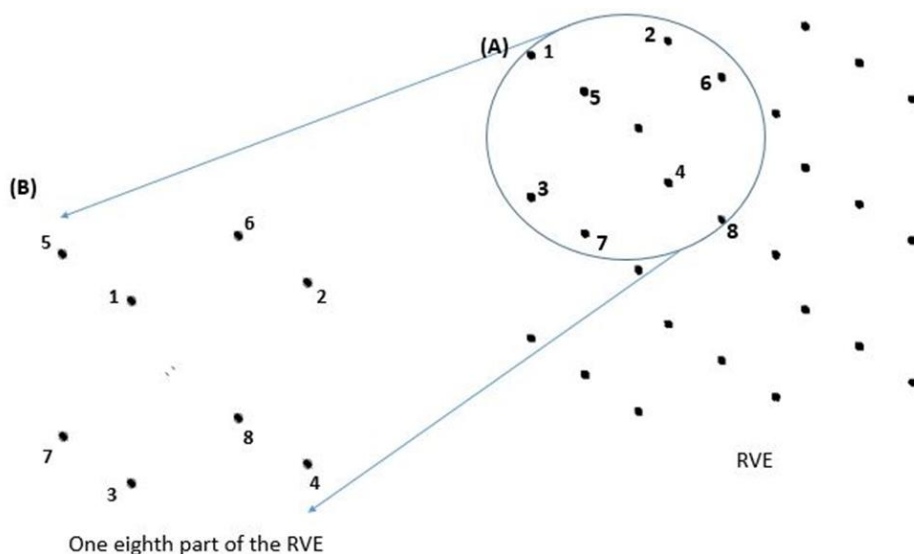


Figure 6. RVE for lattice truss unit cells with (a) 27 vertices, (b) one-eight part of RVE for orthotropic unit cells.

4.2.3. Cellular unit cellular data formation

Thin-wall cellular unit cellular architectures are the primary focus of this work since they have greater natural frequencies than hexagonal honeycomb and other biomimicry designs. For ease in creating modern designs, the height of every unit cellular and the thickness of its walls are fixed. In a 2D format, a RVE (RVE) with 9 vertices is created, as seen in Figure 7. Several lines can be created connecting any two surrounding vertices using the vertices of the RVE. A quarter of the unit cellular can be created by joining a few lines that connect several nearby vertices. Now, a 2D image may be created by mirroring this arrangement of lines along the horizontal and vertical axes. A complete 3D unit cellular is created by giving the lines thickness and extruding them in the third dimension.

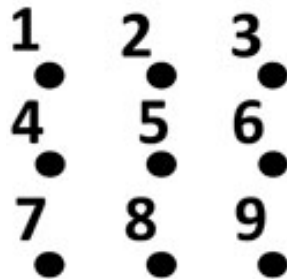


Figure 7. RVE for thin-walled unit cells with nine vertices.

4.3. Fingerprinting

Any machine learning model that wants to intercept the architectural designs has to be able to identify the designs. The process of fingerprinting involves transforming each specific design into a machine-readable code or sequence. For this reason, each design and each new FEA true inside a design is given a specific identification. The parts that follow give a full rundown of fingering various designs.

4.3.1. Biomimicry columns fingerprinting

The biomimicry columns are made up of multiple smaller hollow cylinders with many sizes and an exterior circular shape with an inside circular surface. Each design uses a separate set of these shapes. Each smaller circle, the inner circle, and its location in reference to the origin of the coordinate model are assigned a specific number. Each design was checked to make sure the

origin was at the middle of the outer circle. For the purpose of simplicity, the small circles that make up porosity are all given the same diameter. Each new-shape design is given a specific number in this manner. The biomimicry patterns consist of seven larger outer circles with numbers 1 through 7, six smaller inner circles with numbers 8 through 13, and three smaller inner circles with numbers 14 through 16. The fingerprints are made up of these numbered shapes. The 1500 biomimicry columns in Table 1 are all treated in a manner that is comparable. The final fingerprint for the rod consisted of a single vector with different values that represented each component of the rod. There are around 400 small spherical holes in some designs, such as the root cross-section, which implies that there are 400 more variables in the fingerprint vector in addition to the outer circle. Every one of the 400 variables has a distinct place, and hence, a distinct number. For example, the fingerprint of a rod with an outer, inner, and ten small cylinders is "1, 9, 141, 142, 143, 144, 145, 146, 147, 148, 149, 1410". It specifically describes a rod made up of an inner circle number 9, an outer circle number 1, and smaller circles numbers 141, 142, 143, 144, 145, 146, 147, 148, 149, and 1410. The following will explain what the numbers signify. For instance, the number 141 denotes a tiny circle or cylinder, and the number 1 designates the specific little circle (14) at a defined location within the cylinder.

4.3.2. Lattice truss unit cellular architectures fingerprinting

There is no established strategy for identifying the lattice truss unit cellular architectures in machine learning. Depending on the nature of the incoming data, fingerprints should be thought of as a logical numerical sequence that maintains consistency across the Database. The numbers of the two lattice points that the element links, which are assigned to each lattice point in the RVE, are used to specifically identify each lattice unit cellular. For symmetric lattice truss unit cellular architectures, the eighth of the 27-point cuboid is taken into account for computing RVE. For instance, the lattice unit cellular (12 24 46) represents three elements by linking the points 1, 2, and 4, respectively, of elements 12, 24, and 46 in the eighth section.

It being a symmetric unit cellular, these three components must be rotated into each of the remaining seven mirror planes of the 27-point cuboid to produce the whole lattice unit cellular. In the case of asymmetric lattice truss unit cellular architectures, the 27-point cuboid is regarded as the RVE, and all the components present in the lattice unit cellular combine to create

the fingerprint (Fig. 6). With the fingerprints serving as predictors (input) and desirable attributes like mass, uniaxial compressive along primary direction, and uniaxial compressive with rotational load direction serving as response variables, several databases are independently generated (outputs). For use with machine learning algorithms, these fingerprints are further converted into a vector of 1s and 0s. The fingerprint vector is created by having 1s where there is an element in the design and 0s for the other locations. This is done by associating one constant location with each element. Even while the vector representation of the lattice truss unit cellular architectures by the names of the elements will be easy for human comprehension, a further modification of these vectors in 1s and 0s is more suited for AI models.

To further explain, all combinations of symmetric and asymmetric lattice truss unit cellular architectures can be created by connecting different combinations of points using the one eighth component of the RVE (Fig. 6(B)). Here, the numbers 1 to 27 are assigned to each point of the complete RVE. Eight points in the RVE, numbered from 1 to 8, make up an eighth part. The element bridging each pair of numbers' respective positions is shown. The formation of elements is limited to connecting only points that are immediately adjacent to each other to maintain consistency and meaningful connectivity. For example, point 1 can only form an element by connecting to points 2, 3, 4, 5, 6, 7, and/or 8, which are immediately adjacent to point 1, but not with any other points from points 9 to 27 because there will be another point among point 1 and points 9 to 27. An element generated by joining points 1 and 2 is seen in example (12).

The fundamental and complementary components listed in Table 1 are all that are required to create symmetric lattice truss architectures. The symmetric lattice unit cellular fingerprints are the elements utilized to name each of the primary elements in this context. For instance, a symmetric lattice unit cellular would be (12 24 46). The components from one eighth of the 27-point cuboid, 12, 24, and 46, are utilized to represent the (12, 24, 46) lattice unit cellular as a fingerprint. The complimentary elements that are attached to each primary element in Table 1—(13, 15) for 12, (26, 34, 37, 56, 57) for 24, and (47, 67) for 46—are crucial for maintaining symmetry. Now, other primary element combinations can be created with the "combnk" function. Symmetric lattice truss unit cells may be created by using mirror rotations and

complimentary elements. The cuboid with 27 points is regarded as RVE for forming direction dependent primal asymmetric lattice truss unit cellular architectures. Table 1 cannot be utilized in this situation because asymmetric lattice truss unit cellular architectures are created by randomly combining elements inside the RVE. As a result, the number of components that make up a specific lattice unit cellular are known in advance, and other combinations are created using the same "combnk" function. Asymmetric lattice truss unit cellular architectures made up of the 43 elements in the fingerprint include, for instance, (12 13 15 213 1314 1415 1015 910 39 519 1316 1625 1518 1827 911 1121 1922 2225 2526 2627 2021 2124 2427 18 89 813 815 819 821 825 82725 23 35 28 58 46 47 67 46 68 78 45 27). When an element (12, 13, 15, etc.) includes two digits, it means that it was made by connecting two points, with the first number representing one point and the second digit representing the other. In the elements with three digits (213, 519, 911, etc.), the first digit represents one point, while the next two represent the number of additional points. For elements with four digits (1314, 1415, 1015, etc.), the first two digits stand in for one point, while the following two digits stand in for the other point.

The vertices are named from 1 to 27 and the dotted lines connecting two adjacent vertices are the truss elements. Fingerprinting for lattice unit cellular in figure 8 will be of the form, (12
 13 15 24 26 213 37 39 34 410 414 48 56 57 519 68 616 622 711 78 812 817 823 910 911 1012

1015 1112 1121 1218 1224 1314 1316 1415 1417 1518 1625 1617 1718 1726 1827 1922 1920
2021 2023 2124 2223 2225 2324 2326 2427 2526 2627).

In this case, 12 refers to the truss element joining vertices 1 and 2, 13 to the truss element joining vertices 1 and 3, and so on. The element linking vertices 1 and can be designated as either 12 or 21 because the element's name is independent of the sequence. The machine learning algorithms will treat 12 as a category variable because it has no value.

Example:

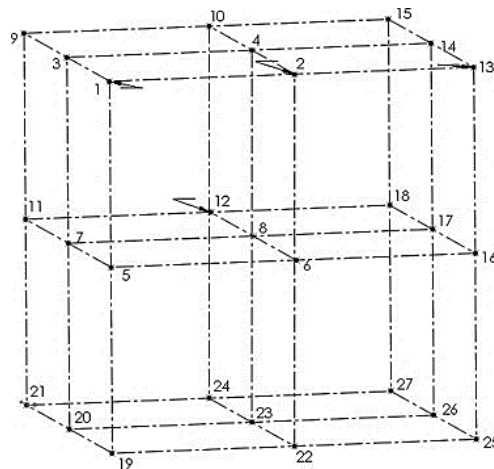


Figure 8. Sample cubic lattice unit.

Table 2. Primary and their complementary elements to form symmetric lattice truss unit cellular architectures

Primary Elements	Complementary Elements					
12	13	15				
16	14	17				
24	34	37	56	57	26	
25	23	35				
28	38	58				
46	47	67				
48	68	78				
45	27	36				
18						

4.3.3. Cellular unit cellular fingerprinting

Because all designs for cellular unit architectures are produced by duplicating the RVE along the horizontal and vertical axes and have the same wall thickness and height, these characteristics are not useful for machine learning and may be eliminated from the fingerprints. As a result, the fingerprinting procedure is reduced to the initial RVE, which simply consists of thin lines joining the 3 by 3 matrix's 9 vertices. All the vertices are named from 1 to 9 for the fingerprinting process, and each line created by joining adjacent vertices is given the names of the two vertices it joins. The fingerprint of a unit cellular is now created by combining the names of all the lines that make up that unit cellular. In Figure 9B, for instance, the lines 14, 15, and 24, respectively, connect the vertices 1 and 4, 1 and 5, and 2 and 4. The names of the remaining lines are similarly called, and the sum of all of them (14 15 23 24 47 59 78 89) will RVE as the specific fingerprint of a single unit cellular. For the purpose of producing the unit cellular for numerical simulations, as previously mentioned, the fingerprint design from the RVE is mirrored into the horizontal and vertical axes to produce a whole unit cellular. It is easy to infer a design from a fingerprint or convert a design into a fingerprint using this fingerprinting strategy. In order to do inverse design and forward regression for more accurate machine learning assessments, these fingerprints are further turned into a vector of 1s and 0s. This is done by giving each of the probable lines in the RVE a 20-vector space (12, 14, 15, 23, 24, 25, 36, 45, 47, 48, 56, 57, 58, 59, 68, 79, 89), putting a "1" in the vector if a certain fingerprint has that line of the form (0 1 1 1 1 0 0 0 0 1 0 0 0 1 0 0 1 1). The same approach should be used to fingerprint all designs for logical forward regression, and consistent boundary conditions should be provided for the generation of all data points. The same approach should be used to fingerprint all designs for logical forward regression, and consistent boundary conditions should be provided for the generation of all data points in the inverse design.

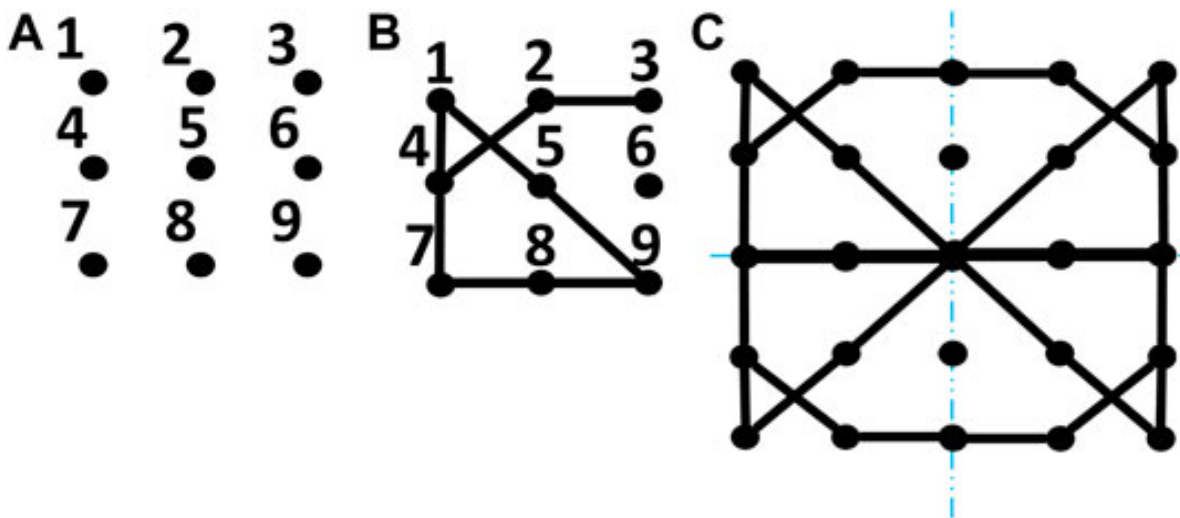


Figure 9. Entire RVE for thin-walled cells with rotations.

4.4. Machine learning prediction

This information can be utilized as input with the architectures created and fingerprinted. The output is the necessary mechanical characteristics for each application, such as the uniaxial compressive loads for the lattice truss unit cellular architectures, the natural frequency, and compression strengths for the cellular unit architectures, and the buckling loads for the biomimicry columns. The training Database formation processes and machine learning prediction models for the prediction of the above-mentioned mechanical and architectural characteristics are described in the following sections.

4.4.1. Buckling capacities analysis of the biomimicry columns

The information used in this study (biomimicry columns with uniaxial buckling loads) comprises inputs for architectural characteristics such as mass, volume, and microstructure as well as an output of the buckling strength of certain designs (columns). As a result, the Database was trained using supervised learning. All the designs' mass, volume, and buckling strength were directly utilized as FEA. Each distinct rod's mass, volume, buckling strength, and geometrical fingerprints were all documented in an excel file. Most information on the biomimicry columns created in Table 1's buckling capacity is unknown. Therefore, using FEA, the buckling capabilities for each biomimicry rod were determined (FEA). ANSYS Workbench was used to analyze buckling and stress. All of the designs were made using Polylactic Acid (PLA), which was produced

additively by Hatch Box. With the use of a Q-TEST 150 device, the mechanical characteristics of PLA during uniaxial compressive were assessed. The compressive of additively made components was compressed in accordance with ASTM standard D695-1523 for this purpose. Five of the ten printed samples were used for the modulus test and the other five were used for the strength test. The measuring strategies and testing speed, which was 2 mm/min., complied with the requirements in [86]. Table 3 provides a summary of the material's characteristics.

Table 3. Mechanical and architectural characteristics of 3D printable PLA

Material	PLA
Density	1,138 kg/m ³
Poisson's ratio	0.4
Young's modulus	1.2424 GPa
Compression strength	55.3 MPa
Tensile strength	11 MPa

An example outcome is shown in Fig. 10; it was achieved by immediately importing the stress vs. strain data from the uniaxial compressive test at room temperature into ANSYS as the constitutive law. All of the columns in Table 1 were modeled and examined in ANSYS Design Modeler under uniaxial compression. All the columns had the identical boundary conditions, stress, meshing strategy, and height (10 cm) to ensure consistency. Euler's buckling analysis was used in conjunction with static analysis to evaluate the rod response under a constant load. For the buckling investigation, all the columns were modeled with the same uniaxial compressive load (1000 N), one end fixed, and the other end supported by a pin. The actual buckling load for each rod was determined by multiplying the ANSYS-provided buckling factor by the applied force (1000 N). The kind of hexahedral element and ultimate element size of 0.1 mm were decided after a convergence analysis was finished. from the example. The buckling load, load, dislocation, weight, and volume of each rod were recorded from the archetype interface.

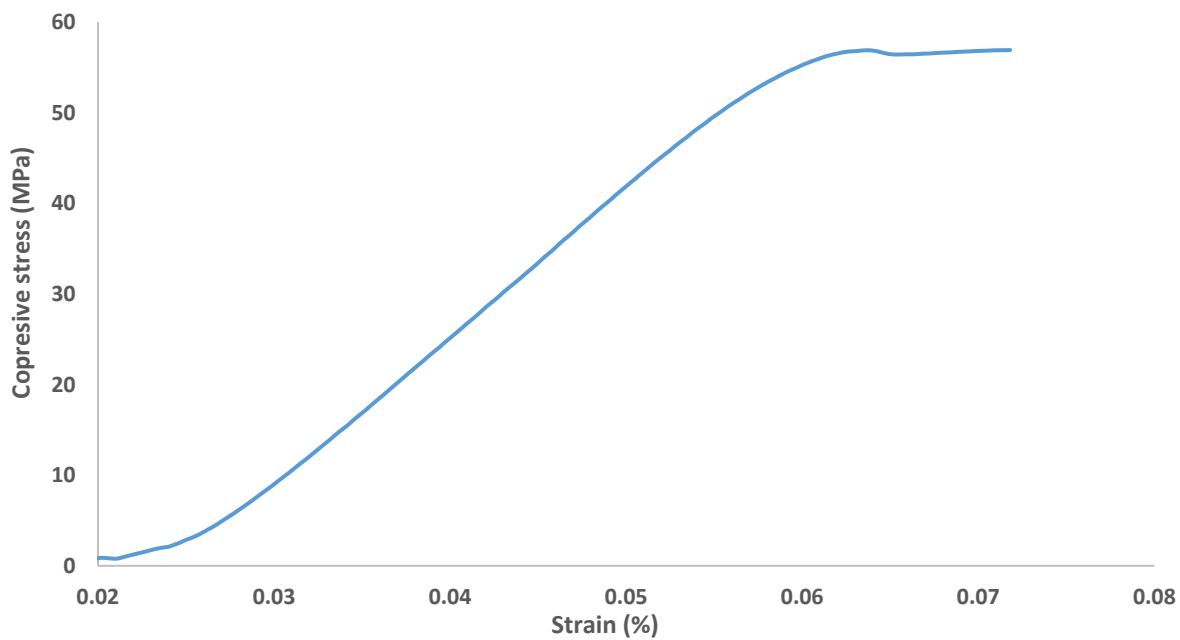


Figure 10. Stress vs strain representation for a typical 3D printed compressive test sample.

In MATLAB, the Database was assessed using a variety of machine learning strategies. The remaining ten percent of the data were used to test the various strategies after ninety percent of the data had been used to train the regression models. The mass, volume, and fingerprints served as the inputs while the buckling strength served as the output for all regression models. Because the output is a single variable that depends on several connected input factors, the machine learning algorithm can easily establish a link between them. The effectiveness of the machine learning algorithms in forecasting fresh data was assessed using fivefold cross-validation. We may assess the performance of several pre-programmed machine learning strategies using our data, and MATLAB offers the root mean square error (RMSE) of each archetype prediction. It is the difference between the actual values seen and the predicted values determined by the assessments. In comparison to other models like SVM, GPR, and neural networks, the Ensemble Bagged Tree approach with a leaf size of eight was found to be the best acceptable machine learning algorithm based on the RMSE for the data type under consideration. The Database is divided into several subgroups in this archetype using an ensemble tree, and each subset is trained individually. The average of the subgroup archetype assessments was used

to construct the final forecast [87]. In comparison to individual subsets, the ensemble of all the subsets produced an archetype that was far more robust. correlation of fingerprints through forward design and buckling load. Figure 11 compares machine learning evaluations to actual results or observations made by FEA. The archetype is more accurate the closer the observations are to the prediction line, where the line represents evaluations, and the dots represent observations. It is evident from Fig. 11 that the ensemble tree archetype provides the most accurate prediction.

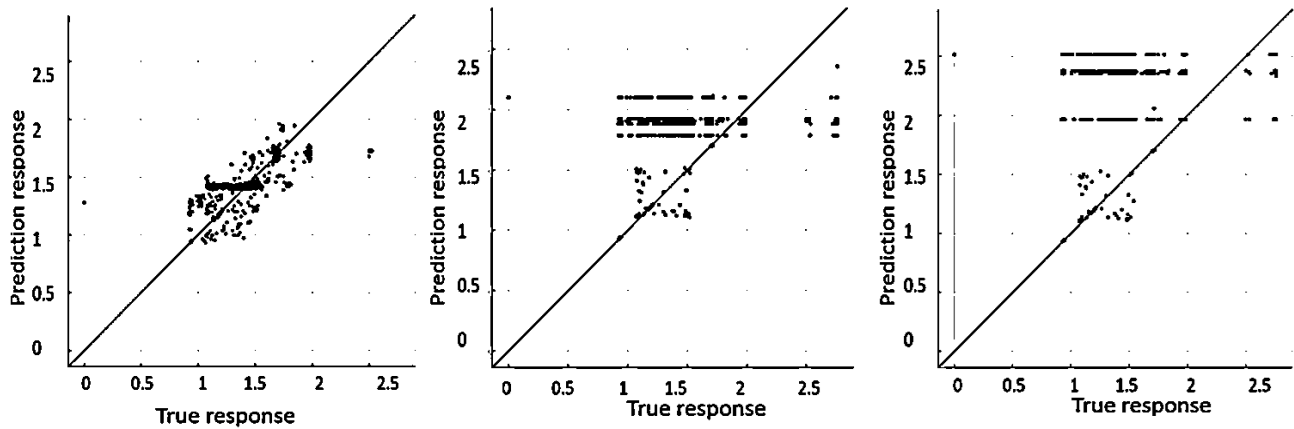


Figure 11. Comparison of evaluations vs. true responses using different machine learning models.

In the ensemble tree approach, the algorithms split the data set into various subsets at random to make evaluations. Even while ensemble trees are based on the mean of forecasts from subsets, precise values for evaluations may not be possible, this approach is extremely helpful in handling complex data. Given that the present data type has huge vectors in its fingerprints, ensemble tree appears to be a suitable archetype for regression using this data type. When the archetype was ready for testing, it was exported to the MATLAB workspace. The workspace was imported along with a table containing the same labels as the training data and a transformation of the test data. The 'yfit' functions were used to forecast the buckling strengths of the test data. The computed error percentage for the remaining test data was less than 10%, with the exception of a few dummy points where the error rate was greater than 10%. Others have also used this margin of error in the past [77-79]. The margin of error was used, but it is now evident that a more precise comparison of the root mean squared error (RMSE) between the training and testing data would be useful for analyzing any overfitting, which may be an issue with ensemble

trees. We'll take this into account when we conduct more study. This archetype may therefore be used to quickly calculate the buckling strength of any column that has data from training models.

For the testing Database, the RMSE and MAE are calculated using the following formula:

$$RMSE = \sqrt{\left(\frac{\sum_{i=1}^N (x_i - y_i)^2}{N} \right)} \quad (7)$$

$$MAE = \frac{\sum_{i=1}^N |y_i - x_i|}{N} \quad (8)$$

Were, RMSE = Root Mean Square Error.

MAE = Mean Absolute Error.

x_i = true values.

y_i = predicted values.

N = Total number of observations.

i = variable i.

4.4.2. Forward regression analysis for compressive stress of lattice truss unit cellular architectures

The data are correlated using the MATLAB Regression Learner package, which contains a variety of regression models. The performance of many machines learning strategies, including Random Forest, Support Vector Models, and Gaussian Process Regression models, is evaluated using the original Database. The rational quadratic GPR model, which had an RMSE of 0.20912, performed the best. The expected vs. true response plots for mass and compression strength (Fig. 12) show how well the evaluations made by machine learning match the actual values.

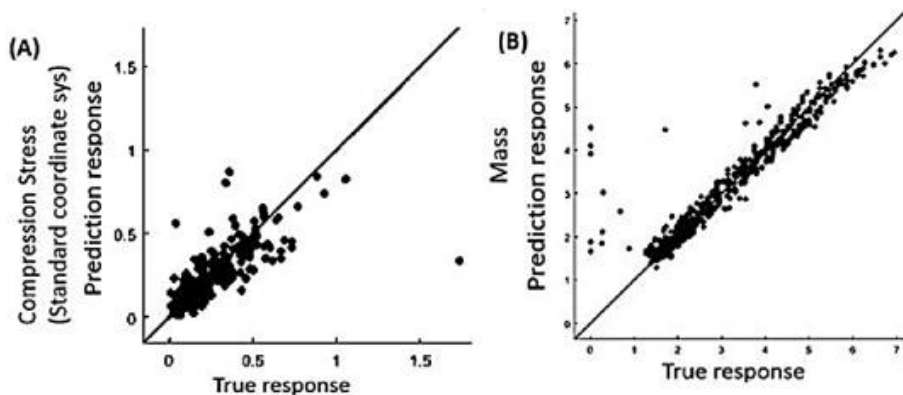


Figure 12. Prediction by GPR machine learning algorithm for lattice truss unit cells.

Table 4. Comparison of various machine learning prediction archetype performances to predict compressive and mass characteristics of lattice truss unit cellular architectures

Uniaxial compressive (Standard coordinate model)						
Machine learning strategy	Training Database			Testing Database		
	RMSE (Root Mean Square Error)	R ²	MAE (Mean Absolute Error)	RMSE (Root Mean Square Error)	R ²	MAE (Mean Absolute Error)
Rational quadratic (Gaussian Process Regression)	0.20469	0.92	0.10348	0.522207	NA	0.436
Machine learning strategy	Training Database			Testing Database		
	RMSE (Root Mean Square Error)	R ²	MAE (Mean Absolute Error)	RMSE (Root Mean Square Error)	R ²	MAE (Mean Absolute Error)
Ensemble (Bagged Tree)	0.24138	0.88	0.11337	0.278609	NA	0.251
Cubic SVM (Support Vector Machine) (table cont'd.)	0.23717	0.89	0.13625	0.433322	NA	0.339

Uniaxial compressive (Standard coordinate model)						
Machine learning strategy	Training Database			Testing Database		
	RMSE (Root Mean Square Error)	R ²	MAE (Mean Absolute Error)	RMSE (Root Mean Square Error)	R ²	MAE (Mean Absolute Error)
Fine Tree	0.33009	0.78	0.13227	0.522207	NA	0.436
Uniaxial compressive (45° coordinate model)						
Machine learning strategy	Training Database			Testing Database		
	RMSE (Root Mean Square Error)	R ²	MAE (Mean Absolute Error)	RMSE (Root Mean Square Error)	R ²	MAE (Mean Absolute Error)
Rational Quadratic GPR (Gaussian Process Regression)	0.26186	0.94	0.12043	0.2847	NA	0.221
Ensemble (Bagged Tree)	0.28321	0.93	0.13955	0.3347	NA	0.251
Cubic SVM (Support Vector Machine) (table cont'd.)	0.28385	0.93	0.15415	0.45781	NA	0.348

Mass						
Machine learning strategy	Training Database			Testing Database		
	RMSE (Root Mean Square Error)	R ²	MAE (Mean Absolute Error)	RMSE (Root Mean Square Error)	R ²	MAE (Mean Absolute Error)
Rational Quadratic GPR (Gaussian Process Regression)	0.26699	0.97	0.08	0.118	NA	0.01
Ensemble (Bagged Tree)	0.38828	0.93	0.21917	0.00632	NA	0.004
Cubic SVM (Support Vector Machine)	0.70689	0.76	0.50732	0.459	NA	0.04
Fine Tree	0.45214	0.90	0.27526	0.305	NA	0.3

The tables above compare various machine learning prediction models for predicting compressive stress and mass. The regression is conducted in MATLAB. The training Database and testing Database can be directly imported to the various machine learning methods using the built-in machine learning prediction modules in MATLAB. All the regression models underwent a five-fold cross-validation. The training period for the SVM and Gaussian process regression models was 300 seconds, with 10 grid divisions. The minimum leaf size of 8 and 30 learners with

a learning rate of 0.1 were utilized for the ensemble (bagged tree) and fine tree models, respectively. The RSME, R-squared and MAE values in the above tables is available with each training algorithm in the MATLAB regression learner application.

4.4.3. Forward regression for natural frequency and compressive load of cellular unit architectures

A training set of 2,000 fingerprints is used to train machine learning models for forward regression. To predict the mass, stress, and first natural frequency of each fingerprint under uniaxial compression, ANSYS workbench tools are used to extract data from the training database. When a structure is disrupted, it vibrates at its natural frequency. One issue with lightweight architectures is still their susceptibility to impact stress and resonance to dynamic load. By raising the natural frequency to avoid resonance and raise energy mitigation, these light architectures can function better. In dynamic architectural loads, natural frequency is crucial [88].

Theoretical background

The equation of motion for a multi-degree-of-freedom model in matrix form may be obtained from the Lagrange equations as:

$$[m]\ddot{\vec{x}} + [k]\vec{x} = \vec{F} \quad (9)$$

where $[m]$ and $[k]$ are the mass and stiffness matrices, \vec{F} is the column vector of non-conservative generalized force and \vec{x} is the column vector of generalized velocity.

Now the solution of the equation of motion for a conservative model corresponds to the undamped free vibration of a model [31]. By assuming a solution of the form $x_i(t) = X_i T(t)$, $i = 1, 2, \dots, n$, where X_i is a constant and T is a function of time t , and substituting it in Eq. 1 gives:

$$[m]\vec{X}\ddot{T}(t) + [k]\vec{X}T(t) = 0 \quad (10)$$

Eq. 2 can be written in scalar form with n separate equations as following:

$$\left(\sum_{j=1}^n m_{ij} X_j \right) \ddot{T}(t) + \left(\sum_{j=1}^n k_{ij} X_j \right) T(t) = 0, i = 1, 2, \dots, n \quad (11)$$

Eq. 3 will give the following relations:

$$-\frac{\ddot{T}(t)}{T(t)} = \frac{\left(\sum_{j=1}^n k_{ij} X_j \right)}{\left(\sum_{j=1}^n m_{ij} X_j \right)}, i = 1, 2, \dots, n \quad (12)$$

Since the Eq. 4 is independent of the index i and t , both sides must be equal to a constant ω^2 , which leads to the following:

$$\ddot{T}(t) + \omega^2 T(t) = 0 \quad (12)$$

$$\sum_{j=1}^n (k_{ij} - \omega^2 m_{ij}) X_j = 0, i = 1, 2, \dots, n \quad (13)$$

$$[[k] - \omega^2 [m]] \vec{X} = \vec{0} \quad (14)$$

To obtain a non-trivial solution, the determinant of the coefficient matrix of Eq. 7 must be zero. This leads to the following:

$$\Delta = |k_{ij} - \omega^2 m_{ij}| = |[k] - \omega^2 [m]| = 0 \quad (15)$$

For Eq. 8, ω^2 is the eigenvalue or the characteristic value and ω is the natural frequency of the model.

Because the regression strategy is made easier by the fact that the other natural frequencies show a similar tendency to the first one, just the initial natural frequencies of the cellular unit architectures are taken into consideration in this case. Using ensemble trees, Gaussian Process Regression (GPR), and Support Vector Machines (SVM), all of which are verified using the MATLAB regression analysis tool, the mass, maximum load, and natural frequency of new cellular architectures are predicted. With an RMSE of 0.16628 N and 0.8031 Hz, respectively, the GPR models had the greatest accuracy in predicting the maximum load and natural frequency of cellular unit cellular architectures. The root mean squared error (RMSE) for the quadratic SVM model's estimate of mass was 0.0048 kg. Figure 13 shows the prediction vs. response graphs for the top regression models. The symmetric distribution of the points along the diagonal line implies decent models. It should be noted that while GPR model worked best for this particular dataset, several other models perform differently with different datasets. No one particular machine learning regression model can be considered best. Depending on the data, dataset size and type of machine learning model, the best suitable model for each type of data shall be selected by comparing different models and their prediction accuracy.

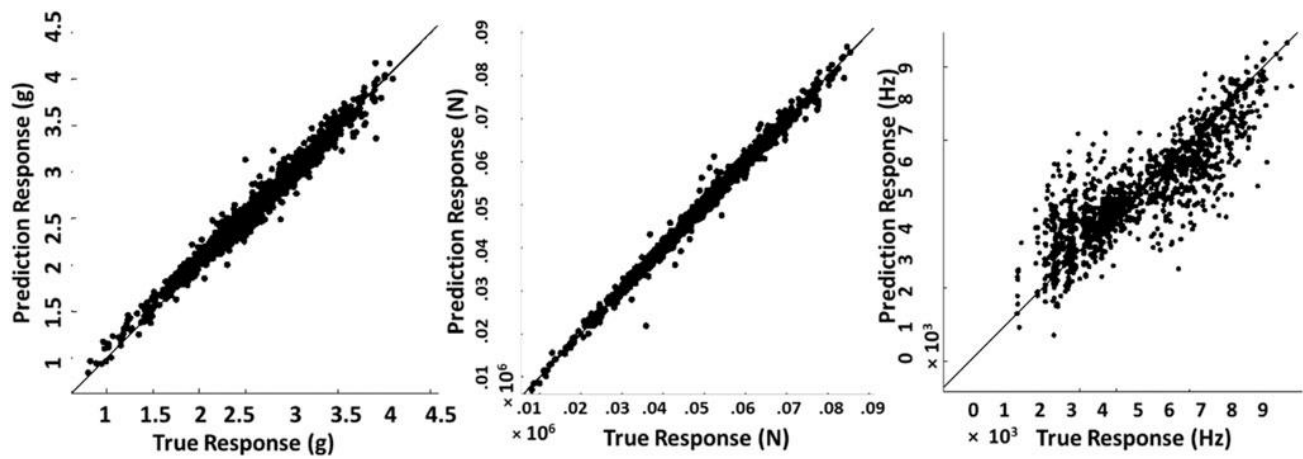


Figure 13. True Vs. Prediction responses for thin-walled unit cellular structures

A suitable filtering strategy or inverse design strategy must be developed to select or suggest the best architectures from the enormous Databases of new evaluations, even though forward regression models show promising results and can be utilized to estimate the architectural characteristics of lightweight architectures quickly and with little computational effort. On this basis, the subsequent chapter will present various improvisation strategies.

Chapter 5. Optimization

5.1. Improvisation of biomimicry columns

After creating a strong machine learning prediction model, the next step in creating biomimicry columns is to improve these designs to create even better columns with higher buckling strengths. The quick validation of new concepts as well as the ease of design are advantages of using machine learning software for improvisation. To anticipate the buckling loads of the new designs, the algorithm needs to be provided with nothing more than their fingerprints. For the forward prediction of several untrained fingerprints in the improvisation, the developed machine learning strategy is used. Compared to physically building each structure one at a time, creating a code that creates different fingerprint patterns is far simpler. A MATLAB algorithm is first created to produce all possible combinations inspired by the biomimicry columns. More than a million possible combinations are created as a result.

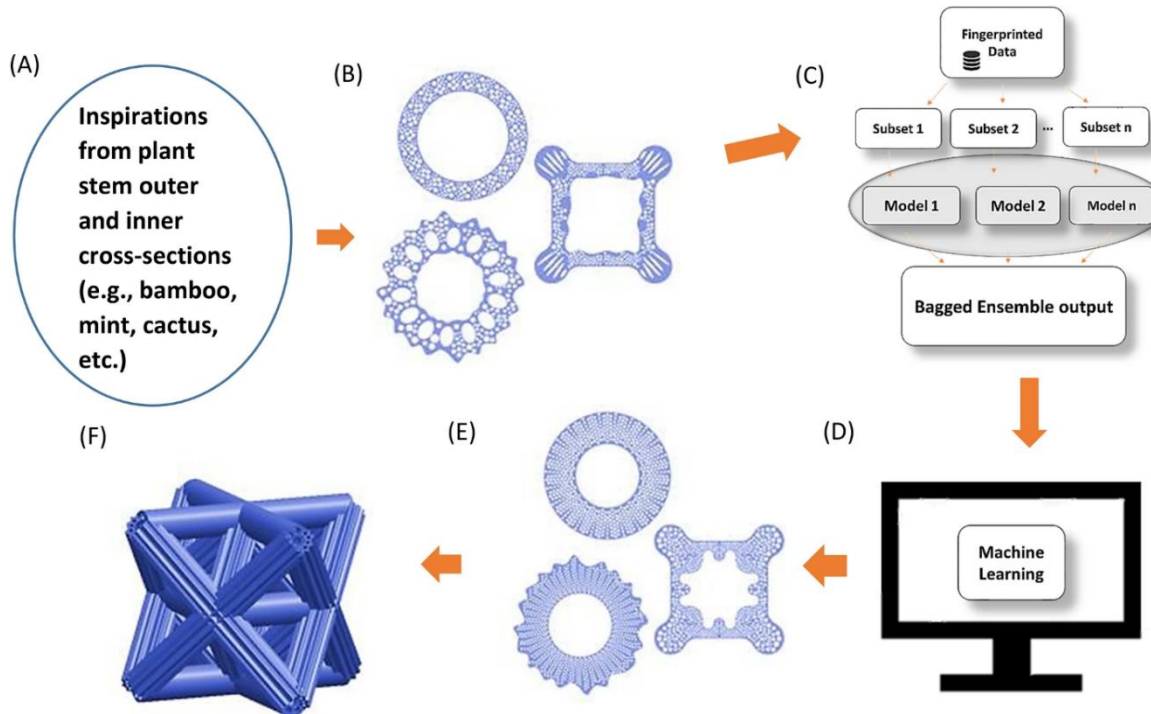


Figure 14. Machine learning assisted framework for biomimicry columns.

Not all combinations, nevertheless, have more refined architectural characteristics. Manually identifying a distinct pattern (number of internal microarchitectures) in the first few

Databases helped determine the minimum and maximum porosity necessary for the columns to outperform the semi-primal (1,500 biomimicry) columns. This originally aided in manually trimming the data sets. EXCEL and MATLAB functions can be utilized to further filter non-primal designs.

The "IF" function, ">" or "," and the "Index" function in Excel may be used to display the filtered fingerprints and show values that are greater or smaller than a specific number (in this case, the buckling load). In MATLAB, there is no indexing function. However, the desired fingerprints from the projected Database can be found using the ">" or "" symbols, and the found variables (fingerprints) can be called and defined in a new Database. Finally, a Database was created that included 160 fresh designs (fingerprints) that outperformed the biomimicry columns in the training Database in terms of buckling qualities.

To assess their performance, the best designs—those with greatest buckling strengths—were chosen. Utilizing ANSYS, these new fingerprints were transformed into 3D CAD designs, and their architectural characteristics were examined under uniaxial compression. The machine learning framework, as well as potential practical implementation in biomimicry lattice architectures, are shown in Figure 14. Table 5 lists all 160 of the modern designs.

These modern designs were subjected to the same uniaxial compressive simulation with the same boundary conditions as the biomimicry columns. Figure 15 presents the findings. The improvised columns that were inspired by the biomimicry columns through improvisation display a buckling strength that is twice as better as the biomimicry columns in the first training Database, as seen in Fig. 15. The stress distribution for different improvised columns is shown in Figure 16. Great betterment can be observed in the buckling capacities of the new designs compared to their biomimetic counterparts while withholding their strength.

Table 5. The created primal designs from inverse design and improvisation

External shapes of improvised biomimicry designs	Primary designs with improvised internal shapes	Number of primal designs in each type
Bamboo		50 columns
Square plant		40 columns
Cactus		50 columns
Bulrush		20 columns

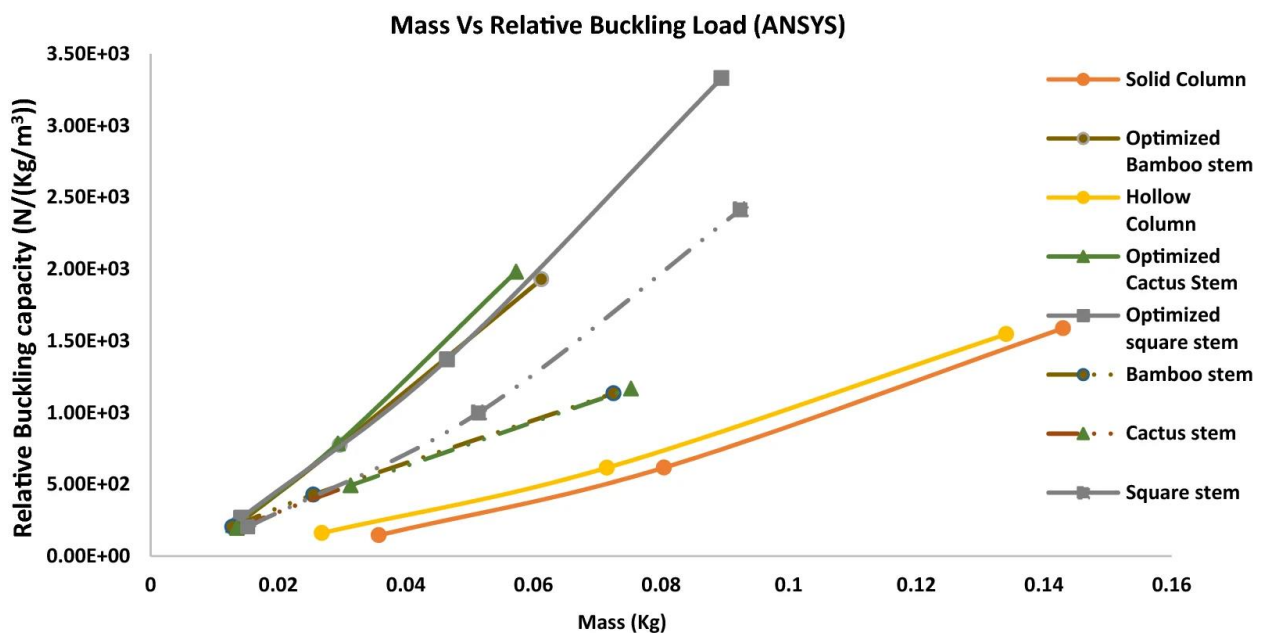
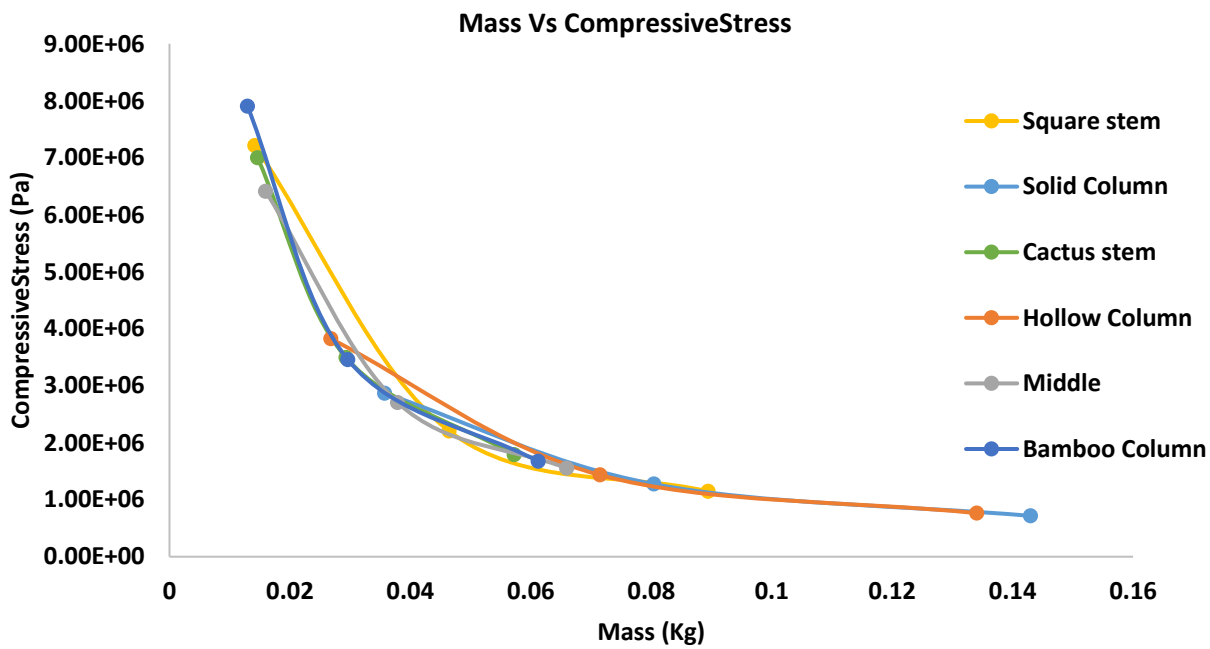


Figure 15. Simulation results from ANSYS conducted on various improvised columns.

(A)



(B)

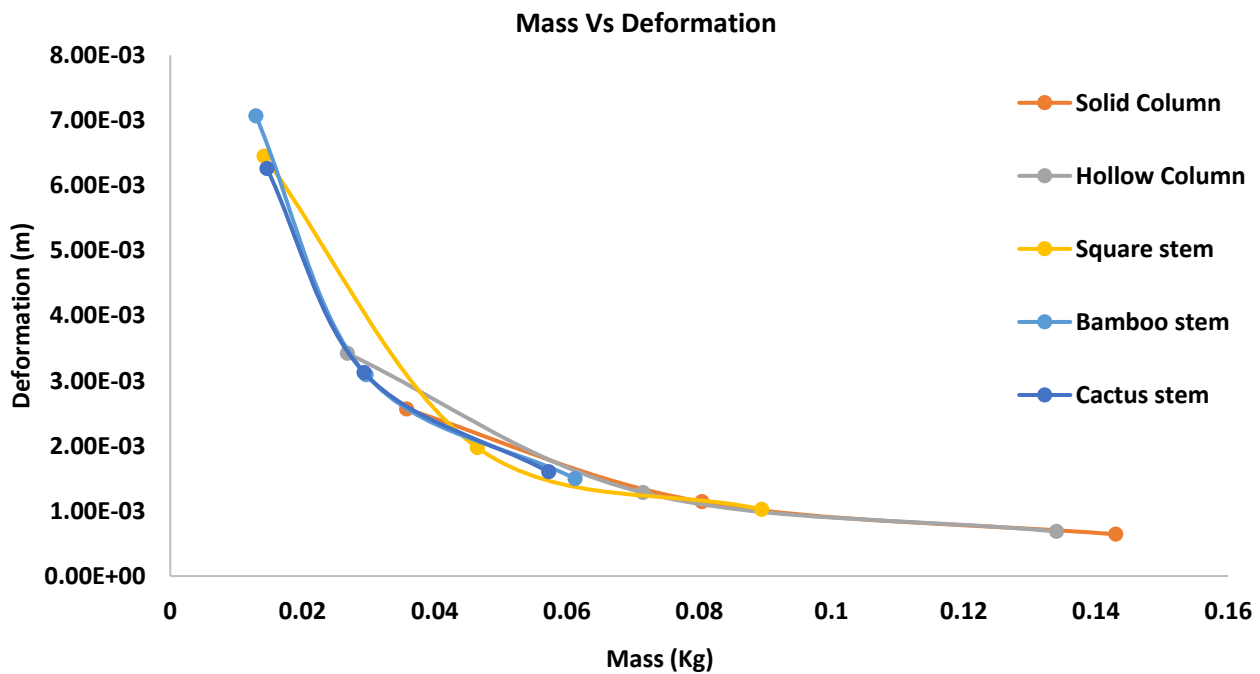


Figure 16. (A) Compressive stress and (B) axial deformation of improvised columns.

5.2. Improvisation of lattice truss unit cells

To identify the lattice truss unit cellular architectures with the highest performance, the machine learning models developed in the preceding section will be used to estimate the mass and compressive stress of different untrained lattice unit cellular signatures. More than 500,000 specific combinations of untrained lattice truss unit cellular architectures are produced using the MATLAB "nchoosek" function inside the boundary constraints of the RVE. Not all architectures perform better even though a substantial Database of lattice truss unit cellular architectures can be constructed. The octet unit cellular, which is frequently thought of as having betterer architectural performance, is taken into consideration as the datum point for comparisons to discover lattice truss unit cellular architectures with the best performance. Once a database with many of these untrained combinations has been established, the GPR archetype is used to anticipate their mass and compressive characteristics by employing the "yfit" function in a matter of 15 minutes or less.

The benefit of adopting a machine learning approach here is that several lattice truss unit cellular architectures can be evaluated for their effectiveness in a matter of minutes with little manual labor and with conventional computational power. After anticipating the required FEA, the vast Databases are compacted to only contain lattice truss unit cellular constructions that surpass the octet truss lattice unit cellular. It requires time and physical labor to create the training database, but if a strong regression archetype is used, data reduction and selection of the best lattice truss unit cellular architectures may be performed rapidly. Additionally, with the least amount of manual effort and time, all permutations within a specified set of boundary constraints or limits may be evaluated. By altering the boundary conditions throughout the data filtering process, it is possible to find lattice truss unit cellular architectures with any required FEA (See Fig. 17 for pictorial representation). To determine the optimal lattice truss unit cellular architectures for topology improvisation, any necessary boundary criteria may be established using Excel data filtering or MATLAB coding. For instance, the filtering process may be used to impose certain boundary restrictions, such as low mass, high compression strength, and symmetric or orthotropic truss distribution along the unit grid, to carry out topology improvisation. A filter is used to recover various fingerprints that have greater relative

compressive (in proportion to overall density) than the Octet unit cellular since it is used as the datum point in this inquiry. Once a Database composed of numerous ideal unit cells has been built, more filters may be configured to retrieve fingerprints from the recently acquired Database. These filters may be used to find fingerprints that have architectural symmetry in the unit cells, as well as those that have a considerably lower mass or superior compression strength under different loading orientations.

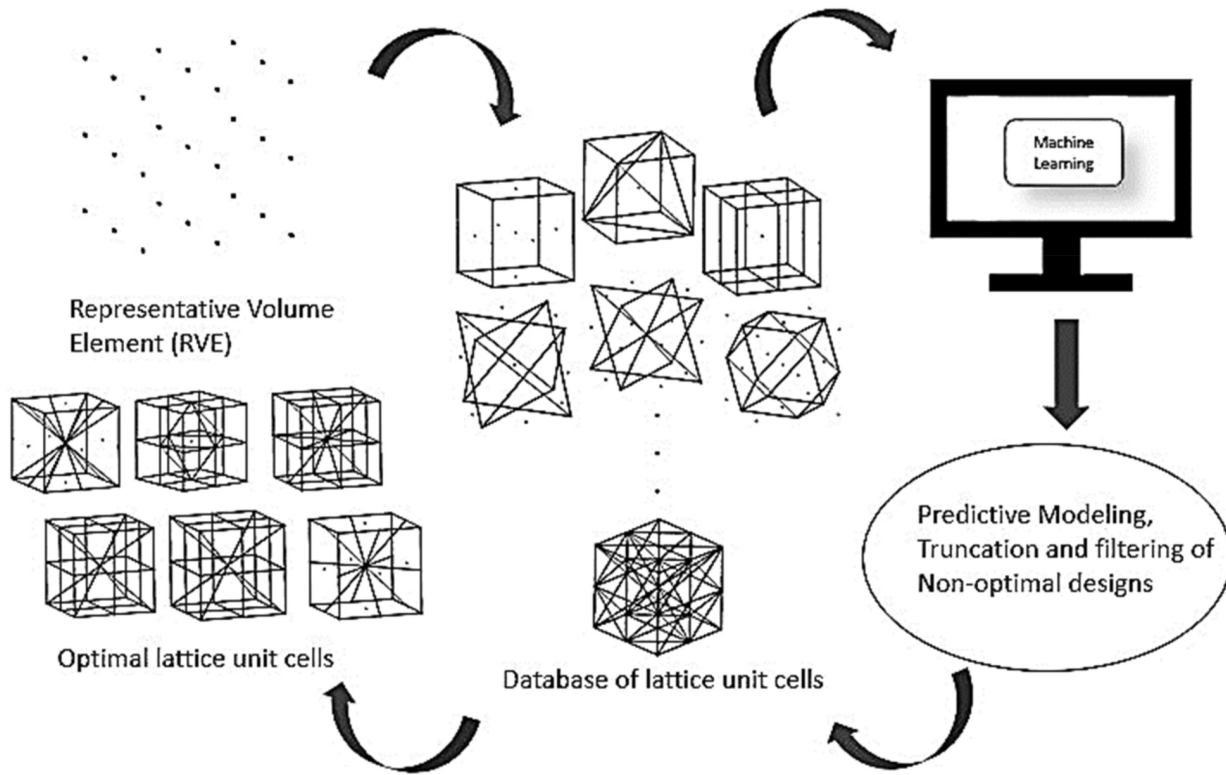
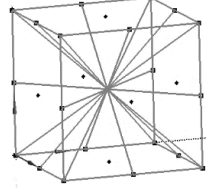
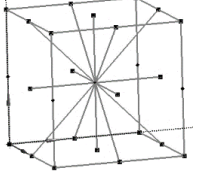
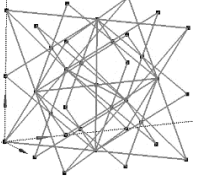
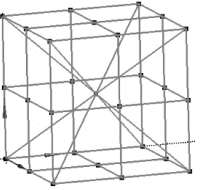
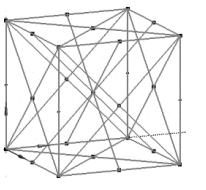
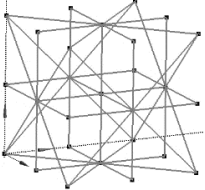
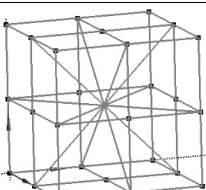
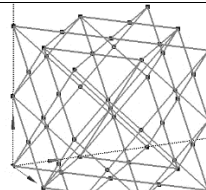
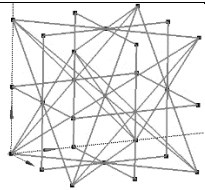
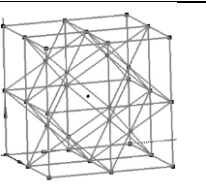
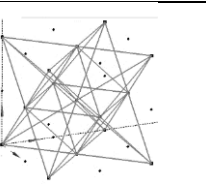
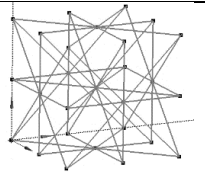
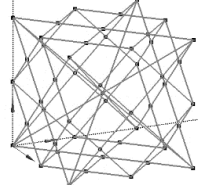
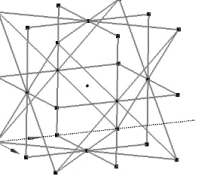
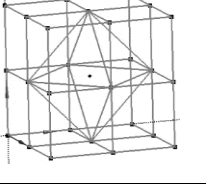
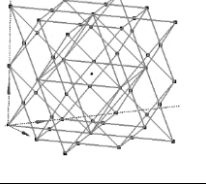
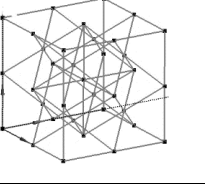
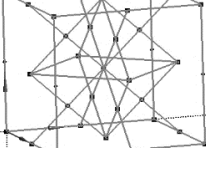
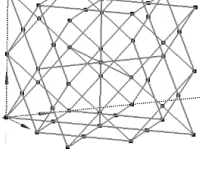


Figure 17. Schematic flowchart of improvisation process for lattice truss unit cells.

This plan is followed by the proposal of 20 primordial designs for symmetric lattice truss unit cellular architectures that outperform octet truss lattice unit cellular in terms of mechanical and architectural qualities (Table 6). It can be seen that each unit cell formed by connecting various number of trusses or rod elements in different orientations within the RVE. This causes changes in the mass and mechanical properties of individual unit cell make it mostly dependent on the structural orientation of the rod elements.

Table 6. Selected primal lattice truss unit cellular architectures

Unit cells	Fingerprint s	Unit cells	Fingerptin s	Unit cells	Fingerprint s
	12 18 28		12 28 48		16 45 48
	12 18 24		12 16 28		16 24 48
	12 24 28		16 25 28		16 24 18
	12 24 45		16 18 46		16 24 28
	12 24 48		16 18 25		16 24
	12 24 46		16 25 46		12 48 45
	12 846		16 25 48		

5.2.1. Validation of the ML predicted unit cells

Using additively manufacturing, several of the ideal lattice truss unit cellular architectures suggested in Table 6 were created and evaluated under uniaxial compression. The optimal lattice truss unit cellular architectures are chosen, and the stereolithographic (STL) files of the 2D architectures are modelled and produced using the Solidworks design application. These STL files may be read by any 3D printer. A professional 3D printer (Pico 2) is used in the production process to cure materials using a vat photopolymerization strategy. The photopolymer is utilized to produce all unit cells. As shown in Fig. 18, three samples of each unit cellular are created with various relative densities.

All of the samples were subjected to a uniaxial compressive test using an MTS machine (ADMET eXpert 2610 Tabletop 5kN Universal Test Model) following postprocessing. To get the stress-strain representations, the compression tests were carried out at a speed of 1 mm/min, and the load and deformation for each sample were recorded. All of the samples evaluated were subjected to ANSYS simulations under the identical boundary and material conditions. Boundary conditions were added to the top and bottom surfaces of the unit cells to represent the compressive behavior. While the bottom surfaces were fixed in the Z-direction, which was the direction of the imposed load, the top surfaces on which the load was applied were granted free movement in that direction. One of the other two directions on the top and bottom surfaces was allowed to slide in order to take the effects of small sliding into account.

The mesh convergence for homogeneity of the identical architectures used in additive manufacturing that were immediately imported into the ANSYS platform was confirmed. The brittle fracture caused every lattice unit cell to break under little force. Fig. 19 shows non-linearity brought on by flaws in the 3D produced lattice truss unit cellular architectures. In terms of compression strength, sample with fingerprint (12 24 46) outperformed the other 3D printed lattice truss unit cellular architectures. The modest difference among the experimental and simulation representations for (12, 18, and 28) unit cells could be the result of support protrusions that were not completely removed or additional cured polymer resin that was not cleaned. Tables 7 and 8 show a list of additional ideal lattice truss unit cellular architectures that have both symmetrical and asymmetrical configurations.



Figure 18. Images of various 3D printed lattice truss unit cellular architectures.

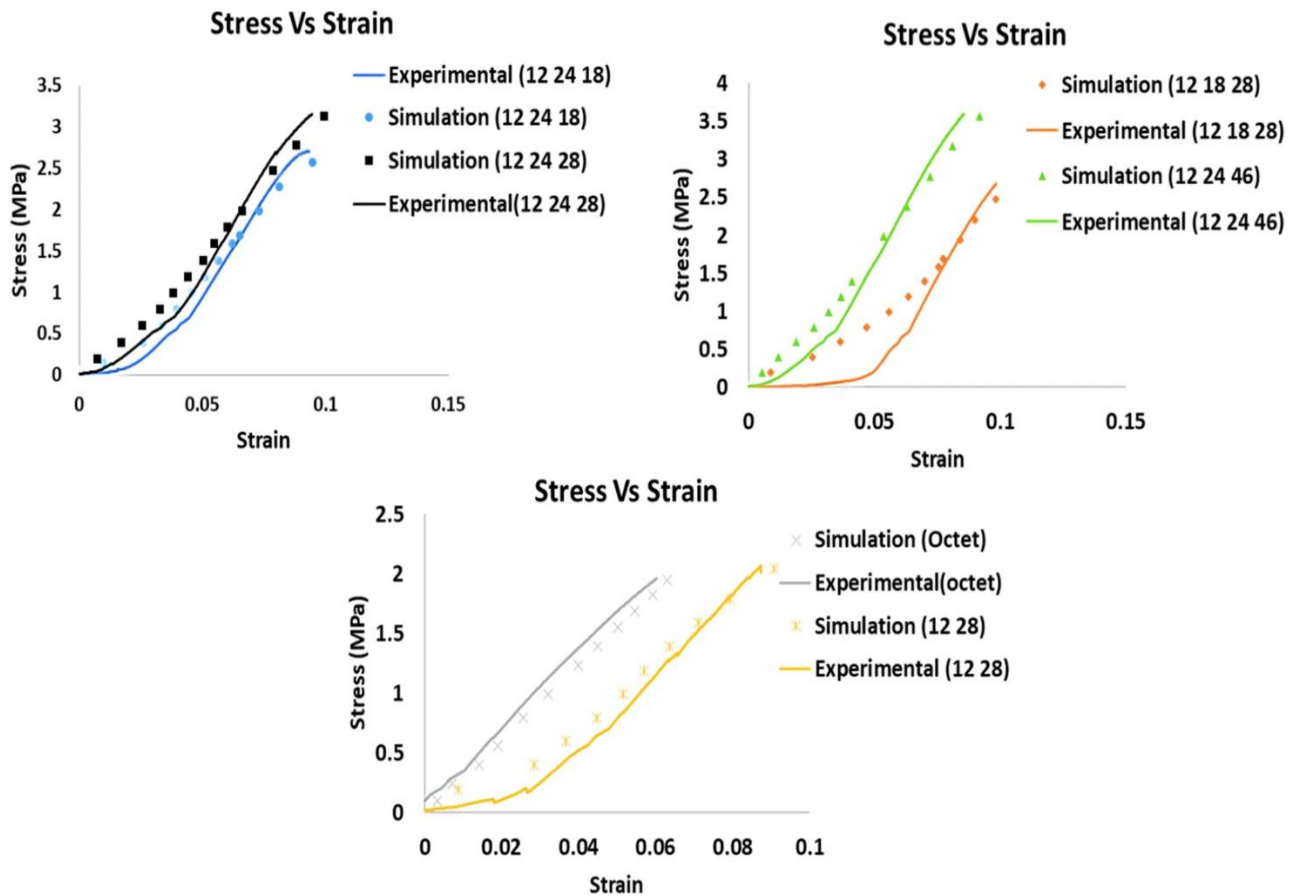


Figure 19. Validations for stress–strain representations of various primal lattice truss unit cellular architectures.

After the numerical results are validated by experimental results on a portion of the unit cells predicted by machine learning, further simulation analysis is carried out on more primal lattice truss unit cellular architectures with varying mass to obese RVE the compressive and tension stresses induced in the lattice elements under uniaxial compressive in different directions. In both normal and angular directions, the suggested optimal lattice truss unit cellular architectures, as shown in Fig. 20, exhibit lower elemental compressive and tensile stresses with the same mass as the octet truss lattice structure.

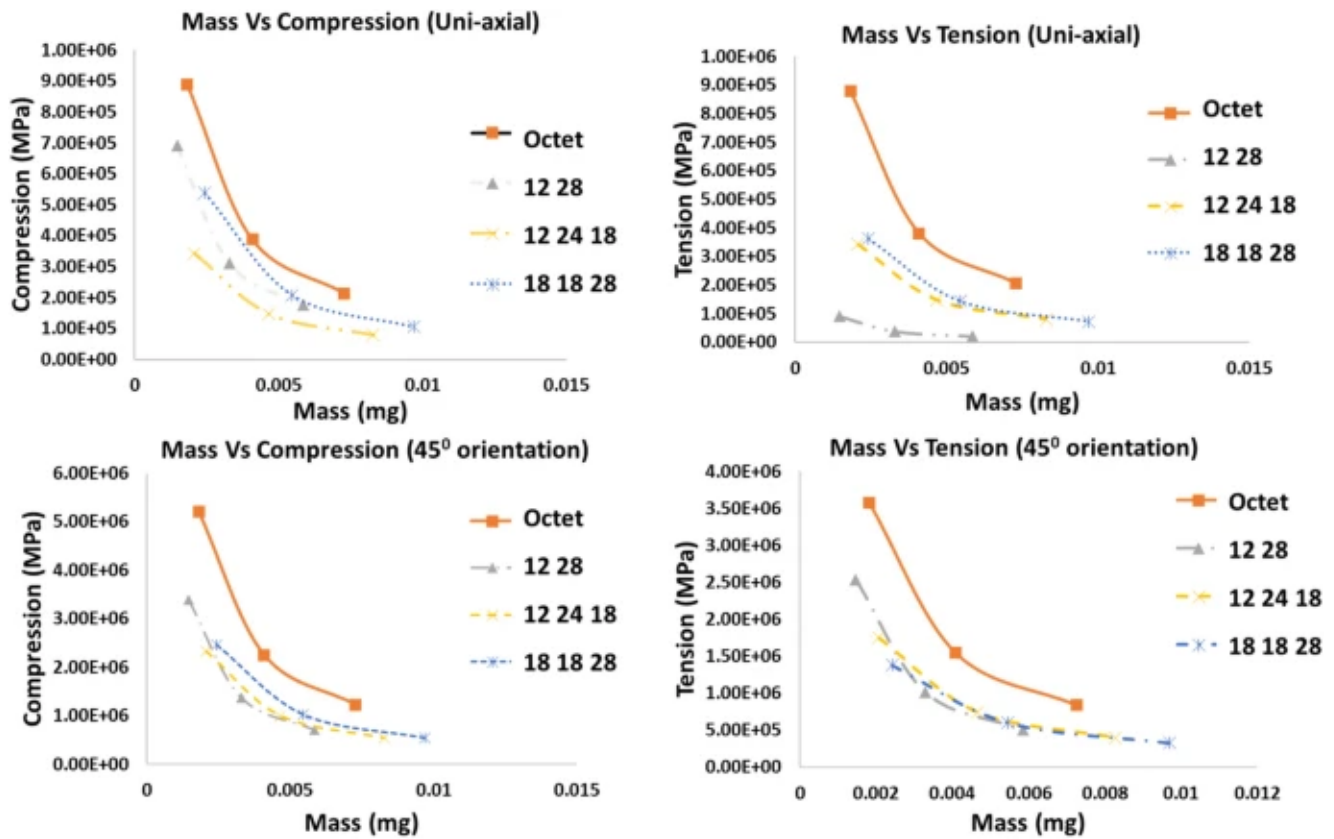


Figure 20. ANSYS simulation results for lattice truss unit cellular architectures compared with octet truss lattice unit cell in different orientations.

Table 7. List of symmetric lattice truss unit cellular architectures

12 28	16 18 45
16 24	16 24 25
16 25	16 24 28
16 45	16 24 46
12 16 25	16 24 48
12 16 28	16 24 45
12 16 45	16 25 28
12 18 24	16 25 46
12 18 28	16 25 48
12 18 45	
(table cont'd.)	16 25 45

12 24 25	16 28 46
12 24 28	16 28 45
12 24 46	16 46 45
12 24 48	16 48 45
12 25 28	
12 28 48	
12 46 45	
12 48 45	
16 18 24	
16 18 25	
16 18 46	

Table 8. List of asymmetric lattice truss unit cellular architectures

Asymmetric primal lattice unit cellular in normal direction (uni-directional)
12 13 15 213 1314 1415 1015 910 39 519 1316 1625 1518 1827 911 1121 1922 2225 2526 2627 1920 2021 2124 2427 18 89 813 815 819 821 825 82725 23 35 28 58 46 47 67 46 68 78 45 27
12 13 15 213 1314 1415 1015 910 39 519 1316 1625 1518 1827 911 1121 1922 2225 2526 2627 1920 2021 2124 2427 24 34 37 56 57 26 25 23 35 28 38 58 46 68
12 13 15 213 1314 1415 1015 910 39 519 1316 1625 1518 1827 911 1121 1922 2225 2526 2627 1920 2021 2124 242718 89 813 815 819 821 825 82724 34 37 26 25 23 35 28 38 58 46 47 67 46 68 78 45
12 13 15 213 1314 1415 1015 910 39 519 1316 1625 1518 1827 911 1121 1922 2225 2526 2627 1920 2021 2124 2427 18 89 813 815 819 821 825 82724 34 37 56 57 26 25 23 35 28 38 58 46 47
12 13 15 213 1314 1415 1015 910 39 519 1316 1625 1518 1827 911 1121 1922 2225 2526 2627 1920 2021 2124 2427 24 34 37 56 57 26 25 23 35 28 38 58 46 68 78 45 27 (table cont'd.)

Asymmetric primal lattice unit cellular in normal direction (uni-directional)
12 13 15 213 1314 1415 1015 910 39 519 1316 1625 1518 1827 911 1121 1922 2225 2526 2627 1920 2021 2124 2427 18 89 813 815 819 821 825 82725 23 35 46 47 67 46 68 78 45 27 36
12 13 15 213 1314 1415 1015 910 39 519 1316 1625 1518 1827 911 1121 1922 2225 2526 2627 1920 2021 2124 2427 25 23 35 28 46 47 67 46 68 78 45 27 36
12 13 15 213 1314 1415 1015 910 39 519 1316 1625 1518 1827 911 1121 1922 2225 2526 2627 1920 2021 2124 2427 24 34 37 56 57 26 28 67 46 68 78 45 27 36
12 13 15 213 1314 1415 1015 910 39 519 1316 1625 1518 1827 911 1121 1922 2225 2526 2627 1920 2021 2124 2427 24 34 37 56 57 26 25 68 78 45 27 36
12 13 15 213 1314 1415 1015 910 39 519 1316 1625 1518 1827 911 1121 1922 2225 2526 2627 1920 2021 2124 2427 24 34 37 56 57 26 25 23 35 28 38 58 78 45 27 36
16 14 17 625 613 619 912 1227 1215 1221 79 719 721 49 413 415 1317 1517 1725 1727 1923 2123 2325 2327 18 89 813 815 819 821 825 82724 34 37 56 57 35 28 38 58 46 68 78 45 27 36
Asymmetric primal lattice unit cellular in 45° directions (uni-directional)
16 14 17 625 613 619 912 1227 1215 1221 79 719 721 49 413 415 1317 1517 1725 1727 1923 2123 2325 2327 18 89 813 815 819 821 825 82724 34 37 56 57 26 25 23 35 28 45 27 36
16 14 17 625 613 619 912 1227 1215 1221 79 719 721 49 413 415 1317 1517 1725 1727 1923 2123 2325 2327 18 89 813 815 819 821 825 82724 34 37 56 57 26 38 58 46 47 67 46 68 78
16 14 17 625 613 619 912 1227 1215 1221 79 719 721 49 413 415 1317 1517 1725 1727 1923 2123 2325 2327 18 89 813 815 819 821 825 82724 34 37 56 57 26 25 23 35 48 68 36
16 14 17 625 613 619 912 1227 1215 1221 79 719 721 49 413 415 1317 1517 1725 1727 1923 2123 2325 2327 625 613 619 912 1227 1215 1221 79 719 721 49 413 415 1317 1517 1725 1727 1923 2123 2325 2327 56 57 26 25 23 35 46 47 67 45 27 36
16 14 17 625 613 619 912 1227 1215 1221 79 719 721 49 413 415 1317 1517 1725 1727 1923 2123 2325 2327 18 89 813 815 819 821 825 82724 34 26 25 23 35 46 47 67 46 68 78
16 14 17 625 613 619 912 1227 1215 1221 79 719 721 49 413 415 1317 1517 1725 1727 1923 2123 2325 2327 18 89 813 815 819 821 825 82724 34 37 56 57 26 28 38 58 45 27 36

Although the data filtering method mentioned above improvises the biomimicry columns and lattice truss unit cellular architectures, it may be difficult to choose the required ideal architectures from databases that comprise hundreds of thousands of designs. Not all design requirements require manual filtering and large database administration. As a result, it's essential to develop inverse design methods for architectural improvisation that go beyond database administration. GANs are used to build primordial architectures with the right characteristics. The next chapter offers a design framework for generating ideal lattice truss unit cellular architectures based on their compression strengths and cellular unit architectures based on their natural frequencies using inverse strategies constructed using GANs, forward regression, and training databases.

Chapter 6. Inverse Design

It takes a lot of human work and is equivalent to hard coding to retrieve the optimum designs throughout the data filtering phase. This takes time, and it has been noted that, particularly with large data sets including millions of data points, some of the ideal designs can be overlooked. The goal of "architectures by design," which is to identify the best architectures given desired architectural attributes, cannot be accomplished using this forward method. This means that while better primal designs than those in the training Database can be proposed, some ideal designs that are within a set of architectural boundary requirements, such as mass, volume, strength, etc., cannot be proposed. This necessitates the development of a superior machine learning strategy that can manage large Databases with less time and manual labor while also predicting targeted ideal designs based on desired design restrictions.

For this, a Generative Adversarial Networks (GANs)-based inverse design ML framework is used. In contrast to forward machine learning, which forecasts certain desirable FEA of a chemical or physical structure, inverse machine learning aims to anticipate an ideal structure given the required attributes. Forward machine learning prediction is a straightforward approach where we forecast numerical data (output) based on categorical data, in contrast to inverse machine learning, which is the reverse of the preceding process and might be difficult (input). Inverse design networks, which combine two deep neural networks, have led to faster and more precise outcomes when compared to other numerical approaches [91]. Using two neural networks and a set of training data, GANs are a type of machine learning that generates new data. While one of the neural networks, the generator neural network, creates new data, the discriminator neural network separates the newly formed data from the training data. The GAN keeps running until the discriminator neural network is unable to tell the difference between the new input and the old training data. This recently created data will be the intended result.

GANs are used to build photonic crystals based on data from a supervised machine learning archetype [91]. When using GANs to create fake inorganic substances, 92.53% of them are specific, and 84.5% of them are chemically sound [92]. A brand-new regression and conditional generative adversarial network (RCGAN) are introduced for the inverse design of two-directional graphene and boron-nitride hybrids [92]. The use of supervised regressive networks

in RCGANs compensates for the incapacity of GANs to generate data samples when fed continuous and quantitative labels. By replacing intricate traditional prediction models with GANs, meta-surfaces that match the necessary optical spectra may also be designed [93].

6.1. Improvisation for superior load carrying capacity

The use of inverse design in improvised architectural design based on mechanical and FEA has not been investigated, despite the recent success of machine learning strategies like GANs and regression in uncovering novel patterns in a variety of domains. This section covers the first inverse design ML framework for identifying, predicting, and enhancing particular lattice unit cellular designs that may be used to create sandwich architectures with higher performance. The remaining components of the inverse design framework, which is built using GANs to produce several possible lattice truss unit cellular architectures, are the forward regression archetype and boundary conditions. All these elements work together to create a single inverse design framework, which results in the creation of lattice truss unit cellular architectures with the appropriate attributes. To create fingerprints for this investigation, a database of many lattices truss unit cellular architectures was initially created (numerical representation). These fingerprints are used as training data for forward regression models to predict the architectural characteristics of certain lattice truss unit cellular architectures and as input to the GANs to generate new lattice truss unit cellular architectures. Sandwich architectures are designed using the expected primal lattice truss unit cellular architectures from the inverse design framework, and they are assessed using computational and experimental strategies.

The inverse design framework for lattice truss unit cellular architectures employed in this study is depicted in Fig. 21. A training Database is provided to the discriminator in the framework, which trains to distinguish among authentic data and fraudulent data produced by the generator. A new set of lattice truss unit cellular architectures with enhanced characteristics are created by applying the set of starting conditions, boundary conditions, and forward regression to the real data.

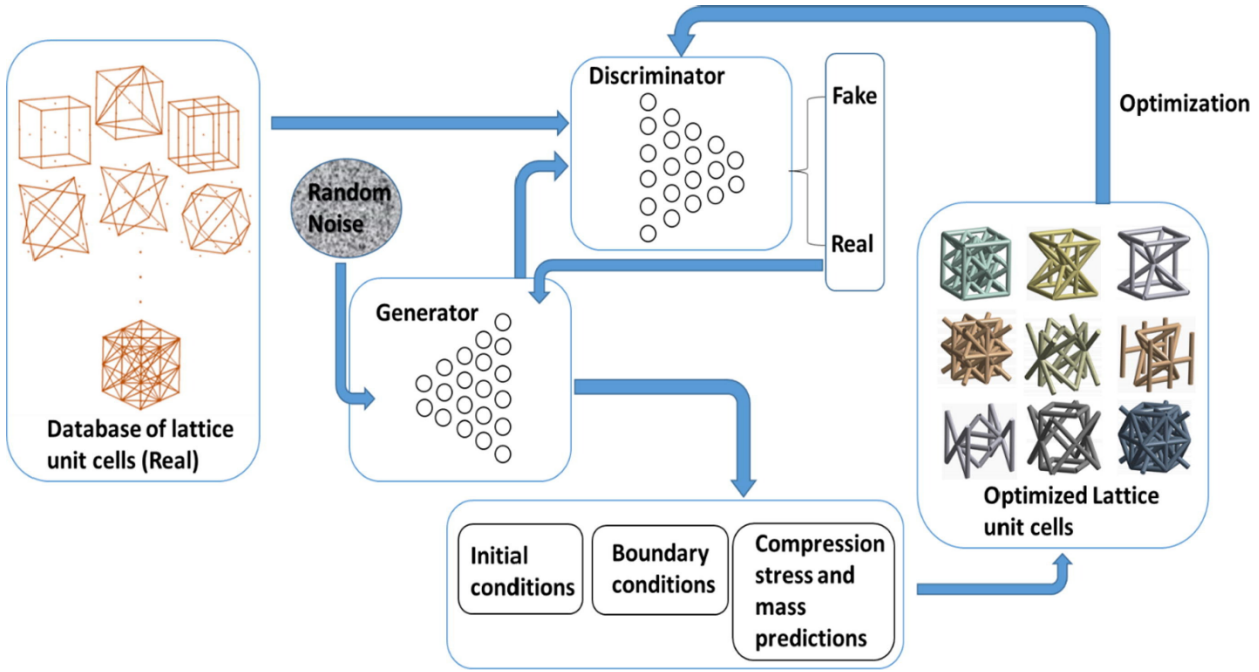


Figure 21. The framework of the inverse design using GAN's for lattice unit cells.

Additional primordial lattice truss unit cellular architectures are produced by further repeatedly training the GAN network using this new database (manually updating the discriminator with latest Databases). Once the inverse design framework is ready with trained GAN network and regression models, the input will be the required characteristics in a lattice unit cell (for example, low mass, better compression strength, or symmetric truss distribution). The outcome is a set of optimal lattice truss unit cellular architectures with fingerprint shapes that satisfy the given input requirements. As a result, the planned inverse design—which predicts primordial lattice truss designs as an output from supplied attributes—is achieved.

The data from this study, which is present in the training database of 1500 lattice truss unit cellular architectures, is input to the discriminator of the GANs model. Based on this, the generator tries to learn from the discriminator and keeps creating new fingerprints until the discriminator is unable to tell fake data from actual data. A collection of distinctive fingerprints that closely resemble those from the original 1500 training Database will be the end result. Currently, the initial training databases contain a variety of lattice truss unit cellular structure fingerprints, some of which outperform octet truss lattice or other superior architectures when

subjected to uniaxial compressive loading. The GANs can only use the training data to generate a finite set of new architectures with similar but different FEA. Therefore, as soon as the GANs generate new data, the new fingerprints should be examined to determine if they fulfill the essential conditions. This includes the ideal compression strength, mass, whether the created fingerprints can really form a structure or not, and if flexural or stretching predominates in the structure. To do this, a number of boundary conditions are applied to the newly formed Database to make sure it complies with the criteria. The mass and compression strength of the produced fingerprints may be rapidly determined using forward regression using the archetype built in the previous section. Maxwell's criteria [16] can be used to assess whether flexural or stretching is more prevalent in a construction. In this analysis, all points are taken into account as stiff. An extra criterion may be added to decide if a recommended lattice unit cellular makes a structure or not. This additional criterion only takes into account fingerprints for which at least one end of each individual element is connected to any other element. This will eliminate fingerprints using truss components without points.

The fingerprints generated by the GANs can be filtered by applying the aforementioned restrictions to all the architectures that outperform a given datum point, in this example the octet truss lattice unit cellular. Every fingerprint that meets the criteria outperforms the octet unit cellular in terms of performance. The inverse design is used on the original database of 1500 fingerprints to produce architectures that outperform octet unit cellular training. In Fig. 22, ANSYS simulations are used to evaluate a few sample fingerprints that passed the predefined specifications during the uniaxial compressive test. At different compressive stresses (40–120%), the expected lattice truss unit cellular architectures are shown to vary while still adhering to the basic goal, i.e., outperforming the octet unit cellular. Several characteristics, including low mass in some lattices like lattices A and B, parallel truss member direction in lattices B, C, and D, and stronger joint connectivity in lattices C and D, could be to blame. However, there isn't a single trait shared by all primal architectures that explains why they perform better than the octet truss lattice.

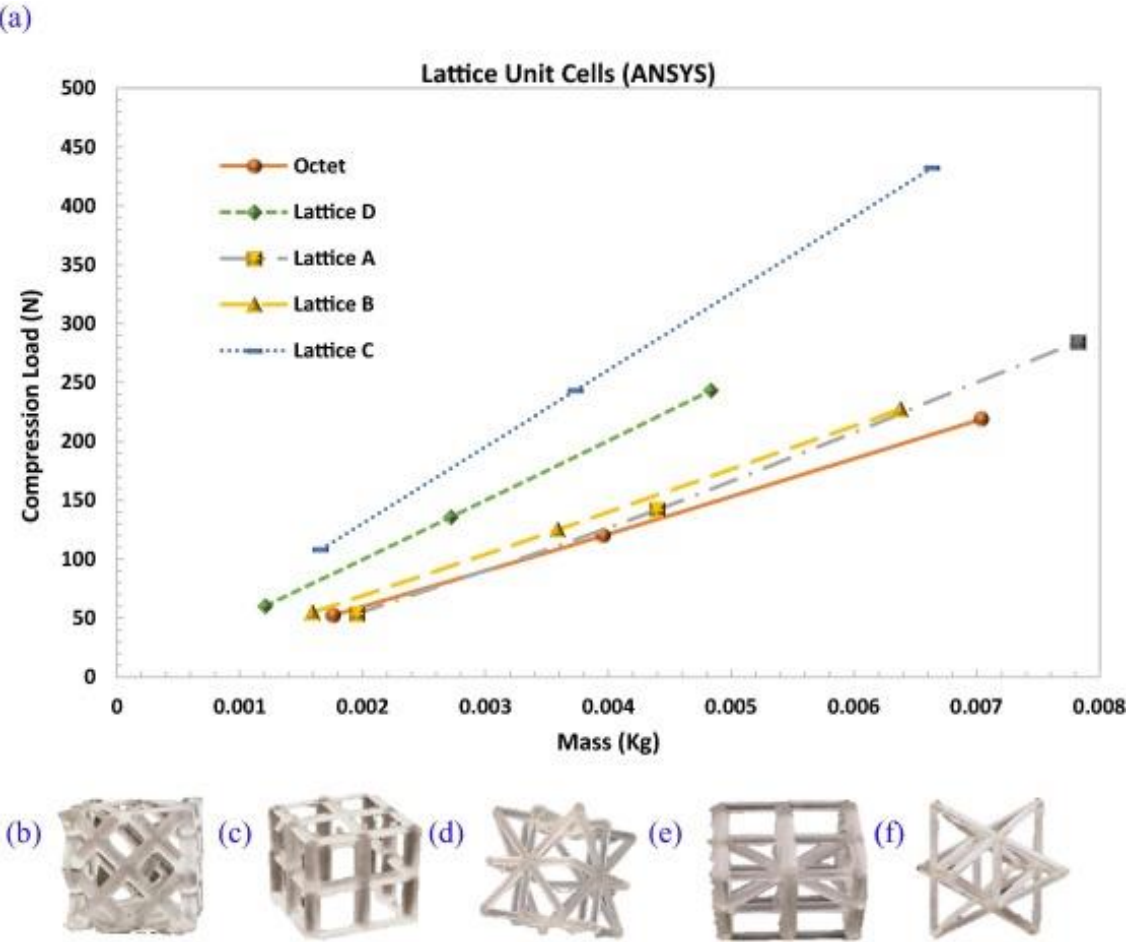
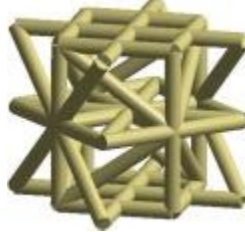
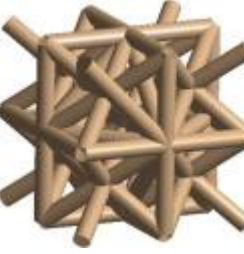
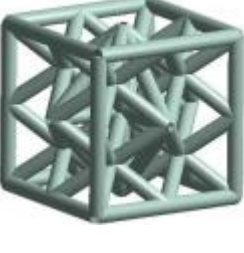
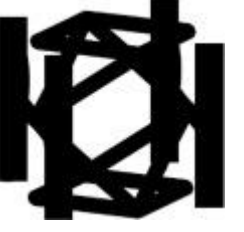
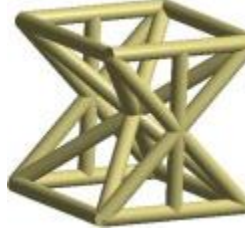
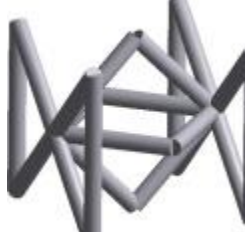
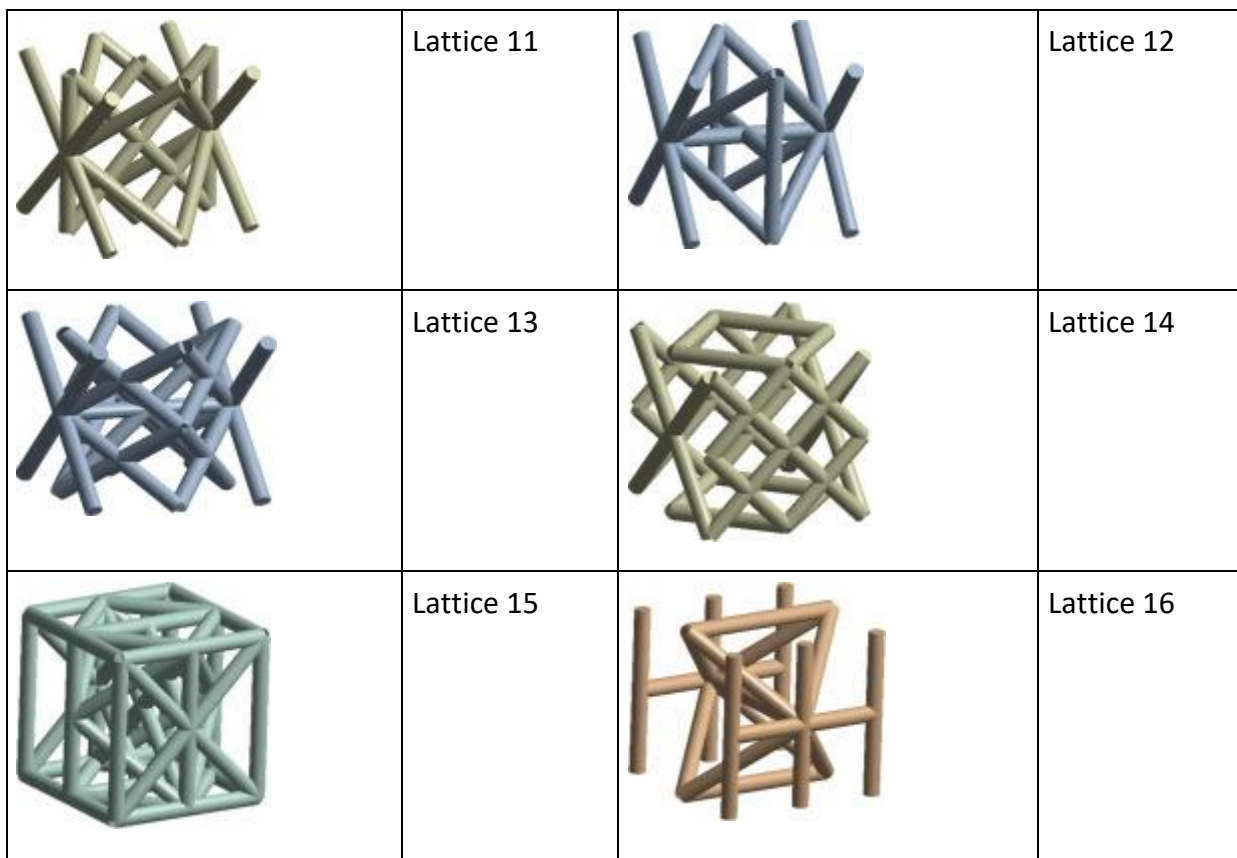


Figure 22. ANSYS comparisons of various primal unit cells predicted through inverse design.

Now, more improvised architectures will be formed using the newly developed fingerprints that outperform the octet unit cellular. A fresh set of data made up of 500 lattice truss unit cellular architectures that outperform octet unit cells is created using the inverse design method mentioned above. Now that the most current Database has been supplied to the discriminator, the generator has been taught to produce new fingerprints using the new Database. The GAN will create new fingerprints close to the new sample space, and this data can bypass the set of boundary restrictions. By setting the goal for mass and compression strength to be significantly greater than those from the prior learning cycles, i.e., even lower mass and better compression strength, further improvised lattice truss unit cellular architectures that outperform the octet unit cellular at a better order can be anticipated. Table 9 lists the photos of 16 improvised lattice truss unit cellular constructions.

Table 9. Images of several primal lattice truss unit cellular architectures

	Lattice 1		Lattice 2
	Lattice 3		Lattice 4
	Lattice 5		Lattice 6
	Lattice 7		Lattice 8
 (table cont'd.)	Lattice 9		Lattice 10



6.1.1. Iterative improvisation of the lattice truss unit cellular architectures by inverse design

The inverse design methodology used in this study allows for ongoing modification of the lattice truss unit cellular architectures by repeatedly leveraging the framework in Fig. 21. To test the effectiveness of the inverse design ML framework, many cycles of improvised lattice truss unit cellular architectures are constructed by optimizing the architectures for each cycle. The results of four groups or forms of these unit cells under uniaxial compressive stress are displayed in Fig. 23. The boundary conditions of the inverse design framework are initially set up to forecast lattice truss unit cellular architectures that are superior to the octet unit cellular by limiting the mass and compression strength of the projected unit cells. As previously noted in the section on inverse machine learning, each new set of ideal lattice truss unit cellular architectures is built by training the GANs using a new primal Database formed from the prior set. According to the ANSYS simulation findings shown in Fig., the improvement in architectural performance from the first formation (set 1) to the fourth formation (set 4) can be clearly shown to have improvements by 50%. 23.

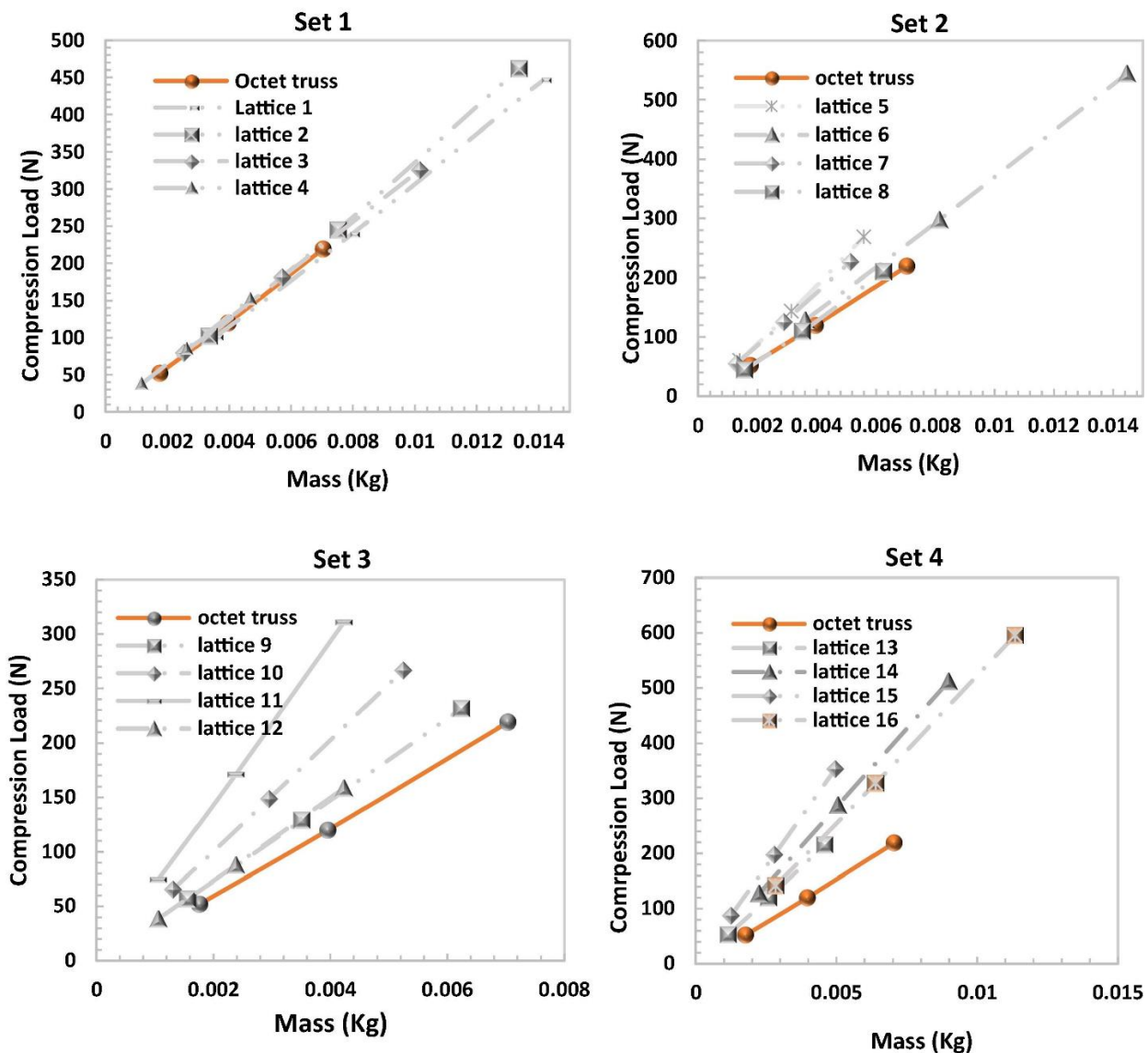


Figure 23. ANSYS comparisons for compressive load vs. mass of several improvised lattice truss unit cellular architectures improvised for each formation.

6.1.2. Experimental comparisons

Using SolidWorks, a 3D CAD design application, models of all the lattice truss unit cellular architectures predicted and evaluated in this study were produced. ANSYS Workbench is used to archetype the compressive behavior of these CAD designs for linear and non-linear analysis. After being converted into the vendor-neutral file format, SolidWorks CAD drawings are fed into the ANSYS platform for simulations (IGES). VeriGuide, a photo-polymerizable resin that can be used for 3D printing and is commercially available, is used for all of the computational and

experimental comparisons (tensile strength 28.5 MPa, elastic modulus 1.14 GPa). Massive deflections are explored for non-linear analysis, and tetrahedron elements are used to mesh the architectures for simulation. The mesh convergence of various mesh sizes is investigated, and an adaptive sizing with resolution order 4 (about 900,000 elements) is taken into account to balance simulation speed and convergence.

For the purpose of experimental validation, stereolithographic (STL) files of the 2D lattice cells are produced using SolidWorks. These STL files may be read by any 3D printer. A professional 3D printer (Pico 2) that uses a vat photopolymerization technology to cure materials creates the lattice truss constructions. All the unit cells are made from VeriGuide, a commercial polymer with a 20 x 20 x 20 mm overall volume. After postprocessing, a dual range XS105 balance is used to calculate the mass of each unit cells, and all the samples are then put through a uniaxial compressive test on an MTS machine (ADMET eXpert 2610 Tabletop 5kN Universal Test Model). The compressive tests are conducted at a pace of 1 mm/min, and the load and deformation for each sample are recorded throughout to provide the load vs. deformation representations. All of the architectures failed due to brittle fracture at low strain. Fig. 24 demonstrates that the simulated findings and the experimental data correlate rather well. The modest discrepancy between experimental and simulation findings might be the consequence of flaws in 3D printed components or inappropriate removal of uncured resin and support materials.

6.1.3. Compressive analysis of lattice cored sandwich architectures

Building sandwich panels with a lattice core is one use for lattice truss unit cellular architectures. Here, numerous sandwich architectures with various densities were built using the best lattice truss unit cellular architectures predicted by the inverse design ML framework. The lattice core is sandwiched among two thin plates on top and bottom to create lattice core sandwich cells. Lattice truss unit cellular architectures are stacked on top of one another to create the core. The 4 by 4-unit cells are laminated using thin sheets that are 10% the thickness of the core, resulting in a variety of sandwich architectures with assorted sizes, as shown in Fig. 25.

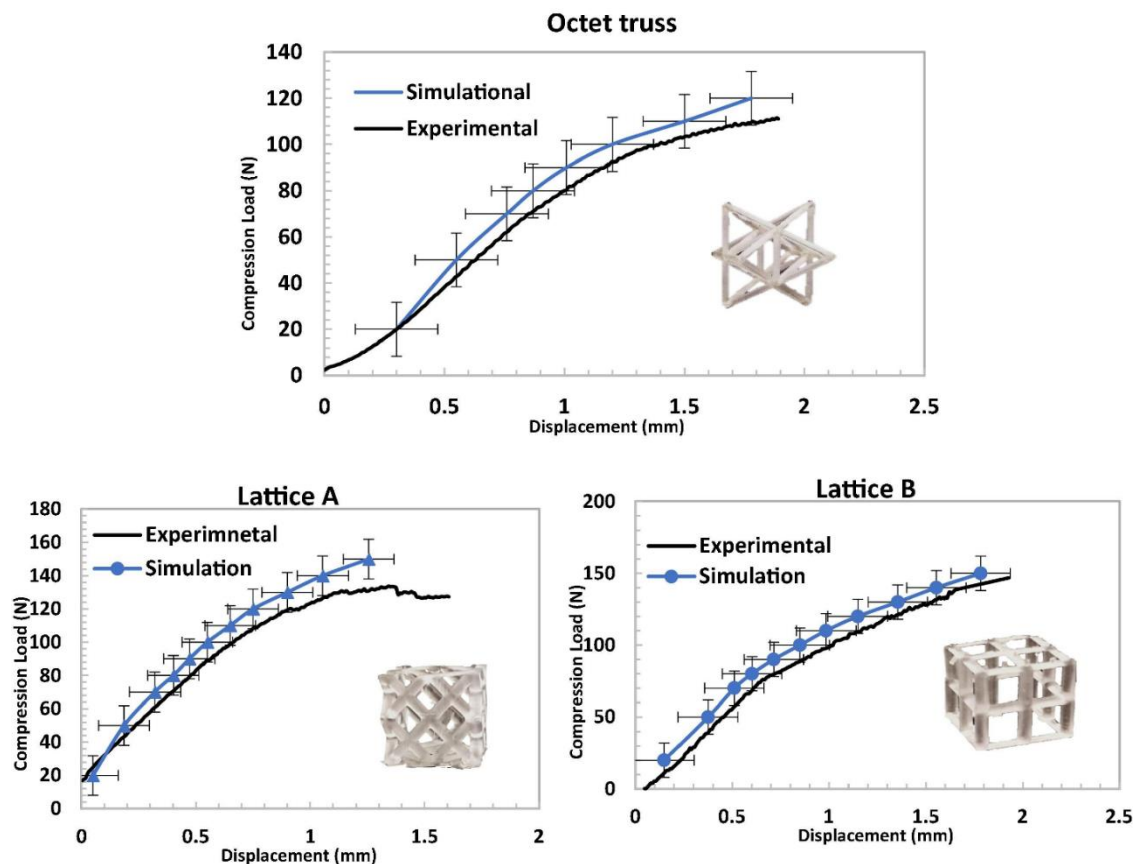


Figure 24. Experimental and simulation comparison for lattice truss unit cellular architectures under uniaxial compression.

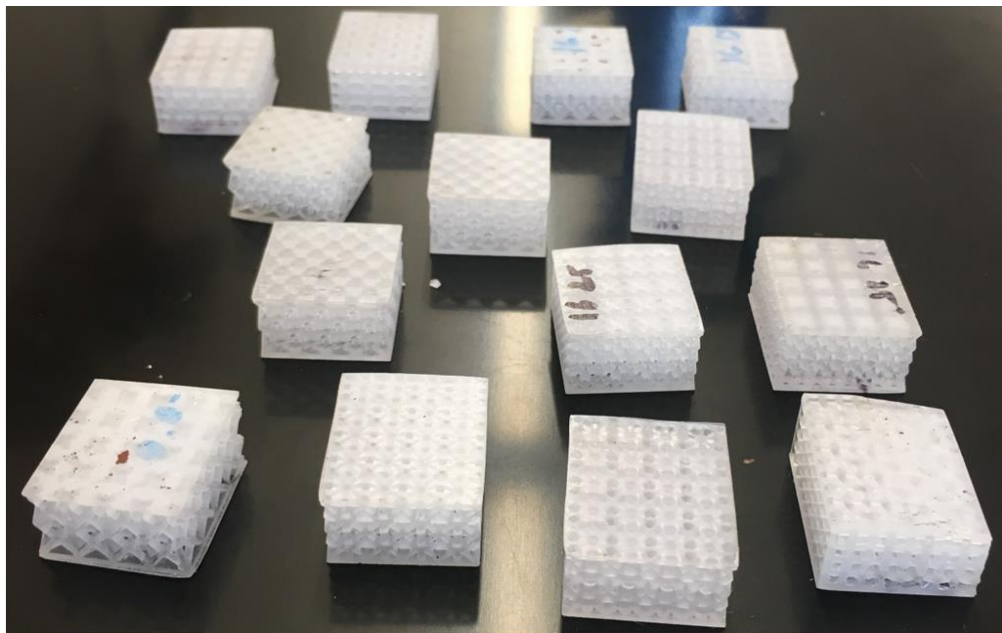


Figure 25. Several lattice core sandwich architectures.

The findings of testing procedures similar to those used on lattice truss unit cellular architectures on the sandwich constructions are depicted in Fig. 26's comparison of compression strength and density. The compression strengths of the sandwich cells are calculated by dividing the maximum compressive loads of the unit cells by their cross-sectional area. The performance of the sandwich cells showed a pattern like that of single unit cell analysis. Sandwich constructions made with optimum lattice truss unit cellular architectures perform 60% better than sandwich architectures made with octet truss lattice cores when subjected to uniaxial stress.

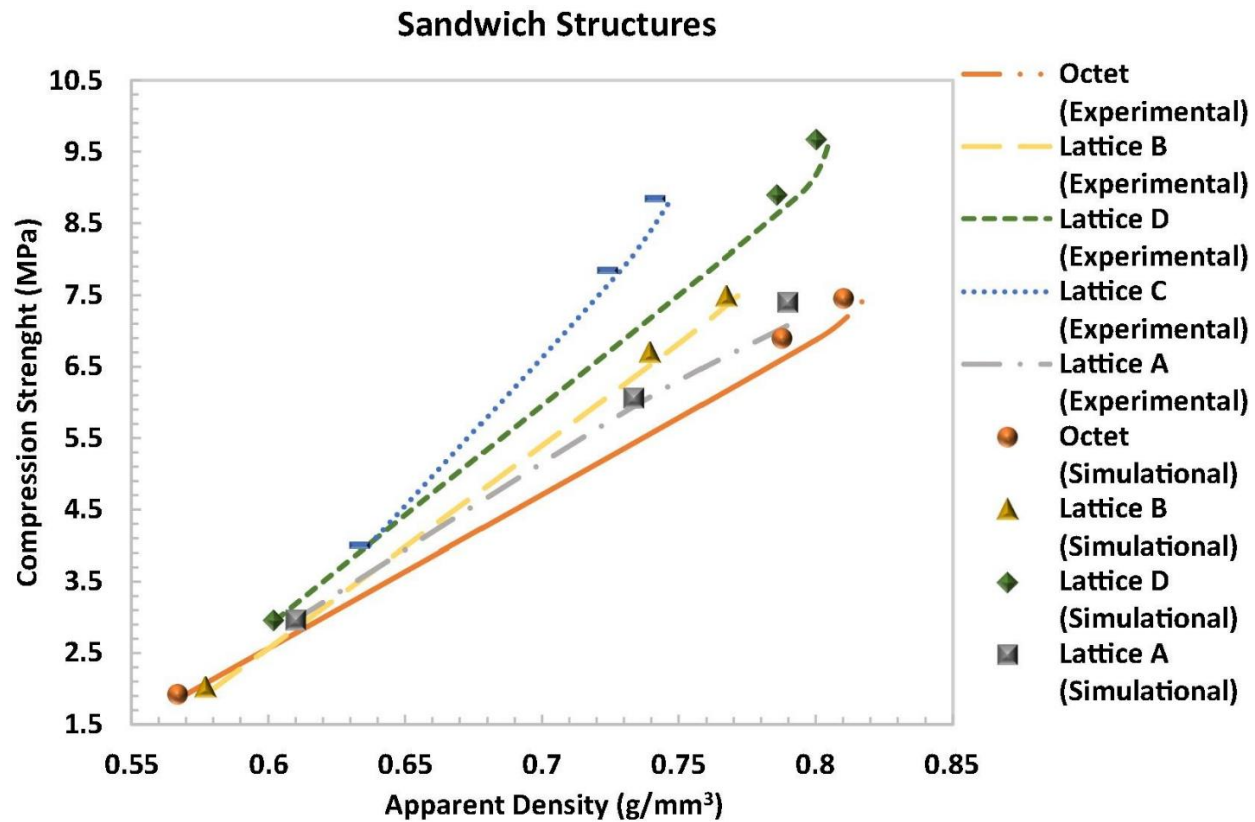


Figure 26. Compression strength and apparent density comparisons among ANSYS simulation and experimental testing of several lattice cored sandwich.

6.2. Improvisation of cellular unit architectures for superior energy mitigation

The best regression models are found by comparing them to hexagonal honeycomb unit cells using a design framework that uses inverse approaches, which may predict unit cells with desirable architectural attributes and optimal cellular unit architectures. Forward regression, additional necessary boundary conditions, and the inverse design framework are integrated with

GANs. In this work, a subset of 300 cellular unit architectures were taken from the original training database and sent to the discriminator of the GAN model to train the GAN model. These cellular unit architectures had superior natural frequencies than hexagonal honeycomb unit cells. The discriminator iteratively trains with the generator until it generates new fingerprints that are strikingly similar to yet distinct from the subset of cellular unit architectures presented to the discriminator in order to predict cellular characteristics like mass and natural frequency, forward regression models are used to build new untrained fingerprints using GANs. The inverse design framework is composed of GANs, forward regression models, starting conditions, and boundary conditions. Boundary requirements, such as the required mass, the maximum load, or the natural frequency, can be specified to produce new cellular unit architectures with the proper FEA. This framework will be given the required characteristics of a cellular unit as input in the form of boundary conditions, and the outcome will be a collection of innovative cellular unit architectures, as illustrated in Fig. 27. Here, the architectural characteristics of the hexagonal honeycomb unit cells are set as boundary conditions along with the regression models to forecast the best cellular unit architectures that outperform biomimicry cellular architectures.

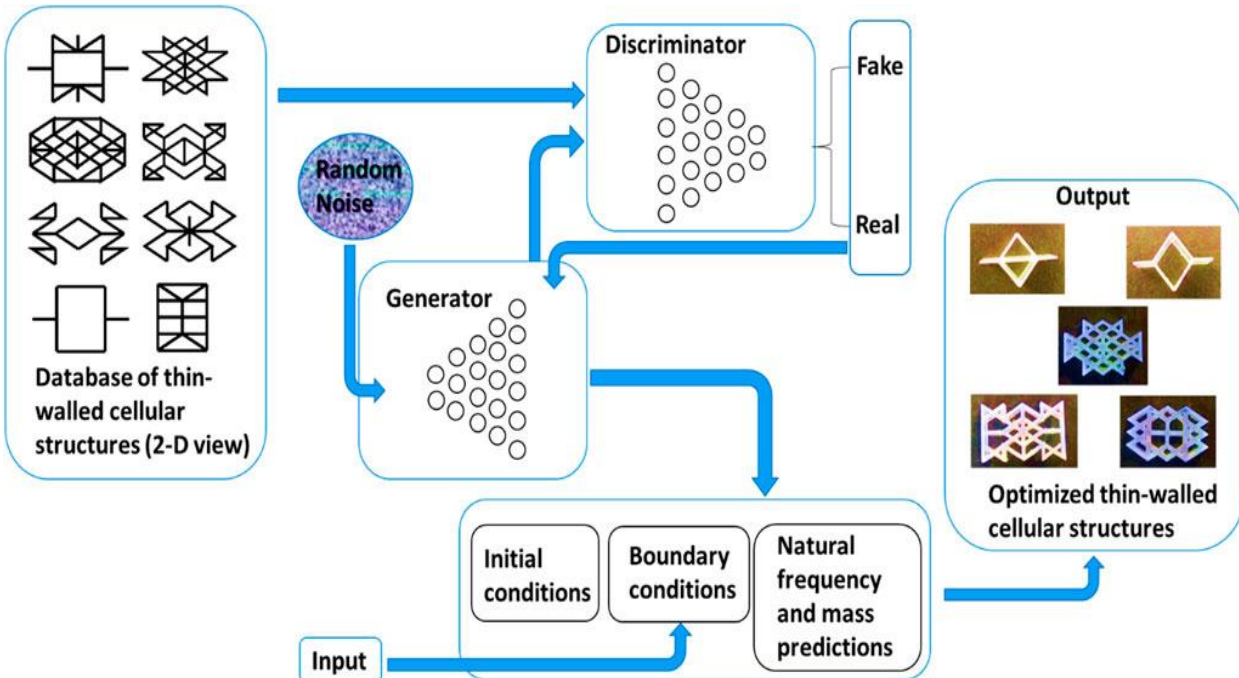


Figure 27. Framework for inverse design of primal cellular unit architectures.

The GAN model must first be trained to generate distinctive cellular unit cellular fingerprints. Step 2: The boundary conditions are given inputs that represent the desired characteristics (better natural frequency, low mass). Step 3: The freshly produced fingerprints from the GAN model are subjected to boundary constraints and a forward regression archetype in order to anticipate mass and natural frequency. 4. The perfect cellular unit architectures that satisfy the boundary criteria have their fingerprints made.

With the same mass and strength as hexagonal honeycomb unit cells but with better natural frequencies, new, perfect cellular unit cellular fingerprints are produced using the inverse design framework. The natural frequencies of the recommended models are compared using simulations in the following sections. The archetype analysis tool with a mechanical APDL solver is used to simulate the natural frequency of each cellular unit cellular with a fixed support on one end and a uniform deformation of 20% on the other end for all designs. The cellular architectures are designed using the ANSYS workbench—design modeler. The upgraded unit cells' native frequencies are contrasted. To make comparisons, many unit cells with various wall thicknesses and calibrated, normalized first natural frequencies are used. Here, the datum structure is a hexagonal honeycomb, and the normalized natural frequencies are calculated using the equation below:

$$f_{1,normalized} = \frac{f_{1,j}}{f_{1,H}} \quad (15)$$

where $f_{1,j}$ = first natural frequency of j^{th} unit cellular,

$f_{1,H}$ = first natural frequency of hexagonal honeycomb unit cellular.

In contrast to biomimicry unit cells like hexagonal honeycomb, bamboo, and trabecular bone architectures, which have been extensively studied for their better natural frequency and energy mitigation qualities, the improvised cellular unit architectures, as shown in Fig. 28, have a normalized natural frequency that is 10–50% better. It has been shown that the hexagonal honeycomb structure outperforms other biomimetic architectures like the bamboo stalk and trabecular bone in the same total volume. Within the same mass range, it is demonstrated that models 1 through 4 all have higher natural frequencies than their biomimicry equivalents. As soon as the mass is more than about 2g, Archetype5 has a higher natural frequency. Due of their higher natural frequencies, Models 1 to 5 make better candidates as cellular unit architectures.

These constructions are considered for further experimental and computational validations to study their behavior during uniaxial compression, DMA, and impact testing.

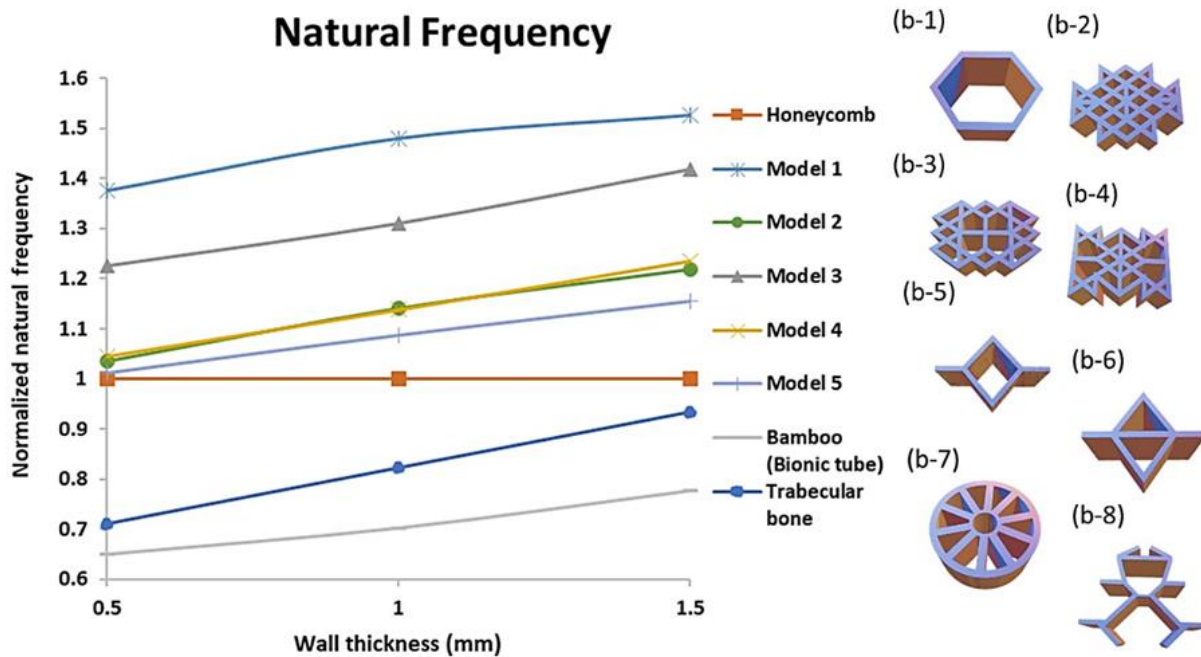


Figure 28. Numerical simulations for Wall thickness.

6.2.1. Uniaxial compression

A few fingerprints of the best cellular unit cellular architectures are chosen to study the uniaxial compressive behavior because they perform better in natural frequency than hexagonal honeycomb structured unit cells. Through the use of CAD design tools, these cells are created as 3D models (Solidworks). All of the 3D models were converted into STL files for additive manufacture using a stereolithographic 3D printer and photopolymer purchased from Formlabs, as illustrated in Figure 29. (a). Each sample is tested for uniaxial compression using a Q-TEST 150 device following postprocessing. For comparisons and validations, the maximum load before failure for each sample is kept track of.

The numerical study was carried out using a program named ANSYS design modeler and simulation. The imported Solidworks 3D models in XML format were pre-processed using the ANSYS design modeler. The bulk material characteristics, such as density, Poisson's ratio, and stress-strain representations from uniaxial compression, were instantly added to the program.

The uniaxial compressive test of 3D printed cylinders (12.7 12.7 25.4) gave these bulk material parameters in accordance with the ASTM D695-15 standard for 3D printable polymers. A consistent printing direction is used to calibrate the material parameters and produce the cellular architectures. A mesh convergence test is carried out for the design, as shown in fig. 30, in order to obtain consistent results without considerably impacting the computation time. Figures 31(a) and 31 demonstrate comparisons between mass and load and mass and natural frequency (b).

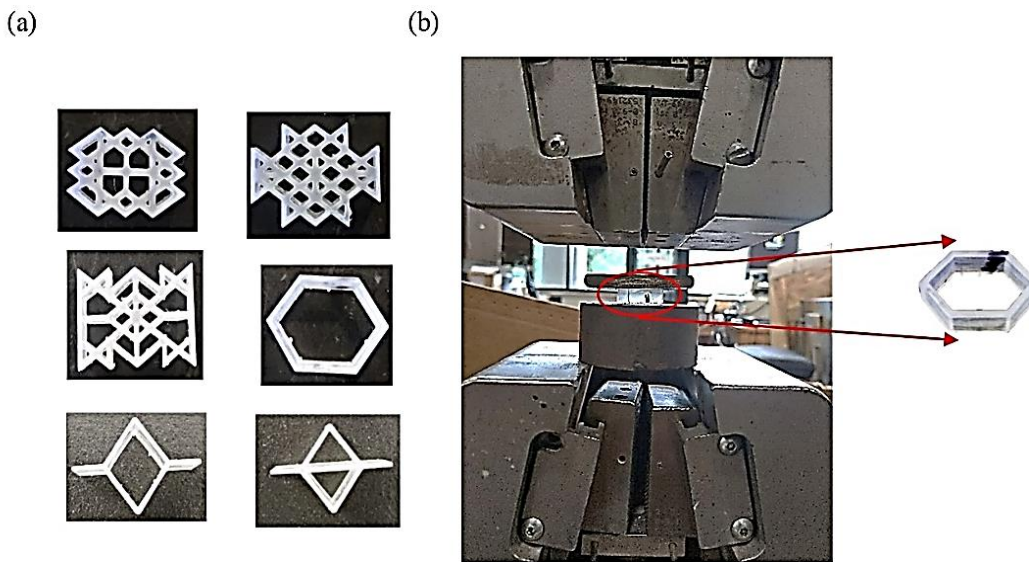


Figure 29. Additively developed (a) cellular unit architectures and (b) Uniaxial compression.

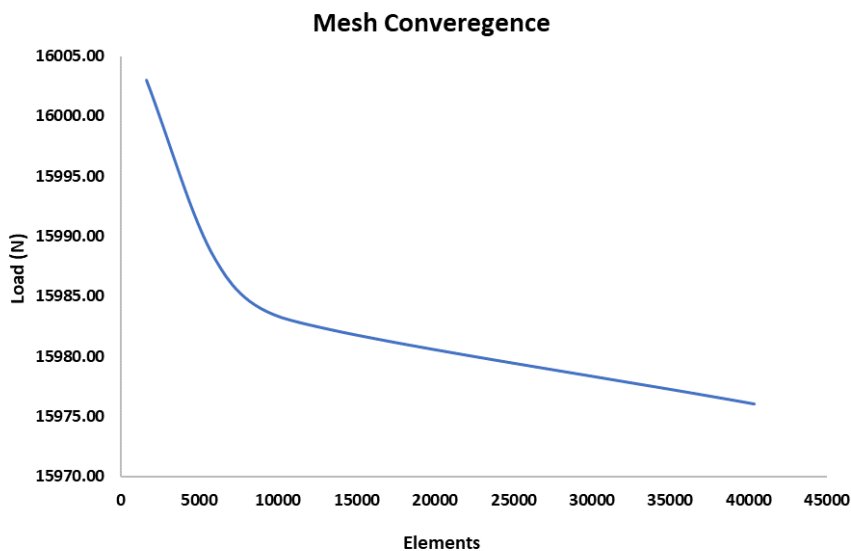
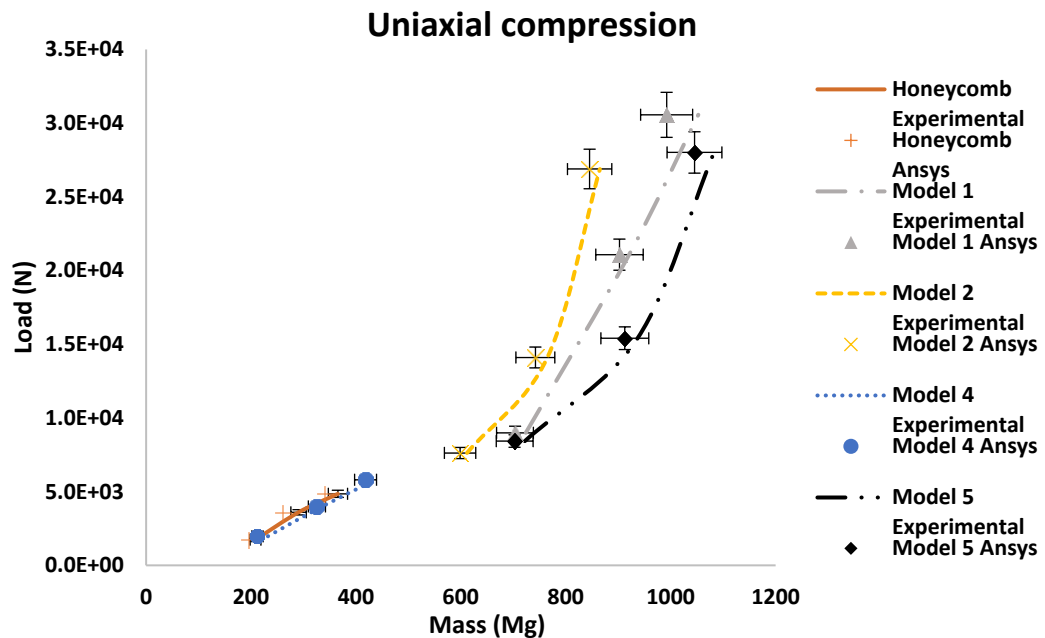


Figure 30. Mesh Convergence for Ansys simulation of cellular unit architectures.

(a)



(b)

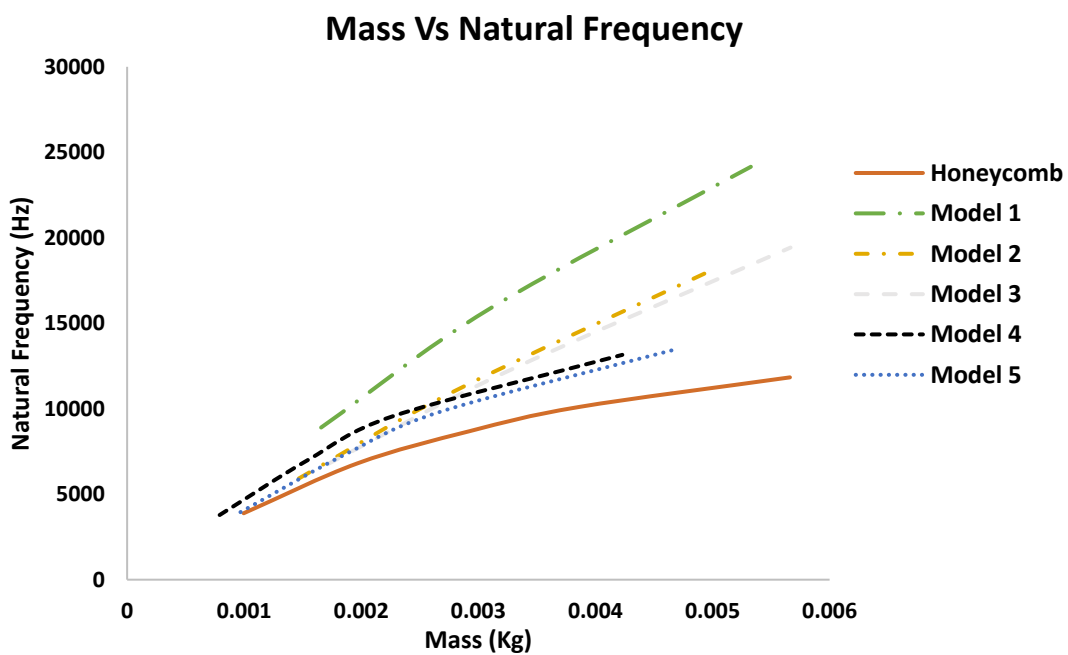


Figure. 31 (A) Mass vs. Load, (B) Mass vs. Natural Frequency.

6.2.2. Dynamic compressive analysis

To examine different samples' responses to the oscillating force at room temperature, the Dynamic Mechanical Analyzer is employed. The elastic response of the structure is measured by the storage modulus (E'), which can be calculated as follows [40]:

$$(E') = \left(\frac{\sigma^0}{\varepsilon^0} \right) \cos \delta \quad (16)$$

The loss modulus (E'') is the energy dissipated due to friction or internal motion and can be calculated as following:

$$(E'') = \left(\frac{\sigma^0}{\varepsilon^0} \right) \sin \delta \quad (17)$$

where σ^0 = stress at the peak of the sin wave, ε^0 = strain at the peak of the sin wave, and δ = phase angle.

The efficiency of the structure's loss energy, also called as damping ($\tan(\delta)$) can be measured by the ratio of the loss modulus to the storage modulus:

$$\tan(\delta) = \frac{E''}{E'} \quad (18)$$

To examine the behavior of the proposed unit cells under cyclic loading, many designs were 3D printed using the same SLA printer and transparent photopolymer detailed in the uniaxial compressive section. As shown in Figure 32, all the specimens are put through a dynamic evaluation utilizing an RSA-G2 Dynamic Mechanical Analyzer with variable frequency. See S10 for a theoretical foundation (c). The storage modulus, loss modulus, and damping ($\tan(\delta)$) characteristics of the specimen are determined for an angular frequency range of 1 - 62 rad/sec (0.16 - 10Hz) and 0.125% strain under compression. The overall volume of each specimen is intended to be the same (2 mm, 1.2 mm, and 1.15 mm).

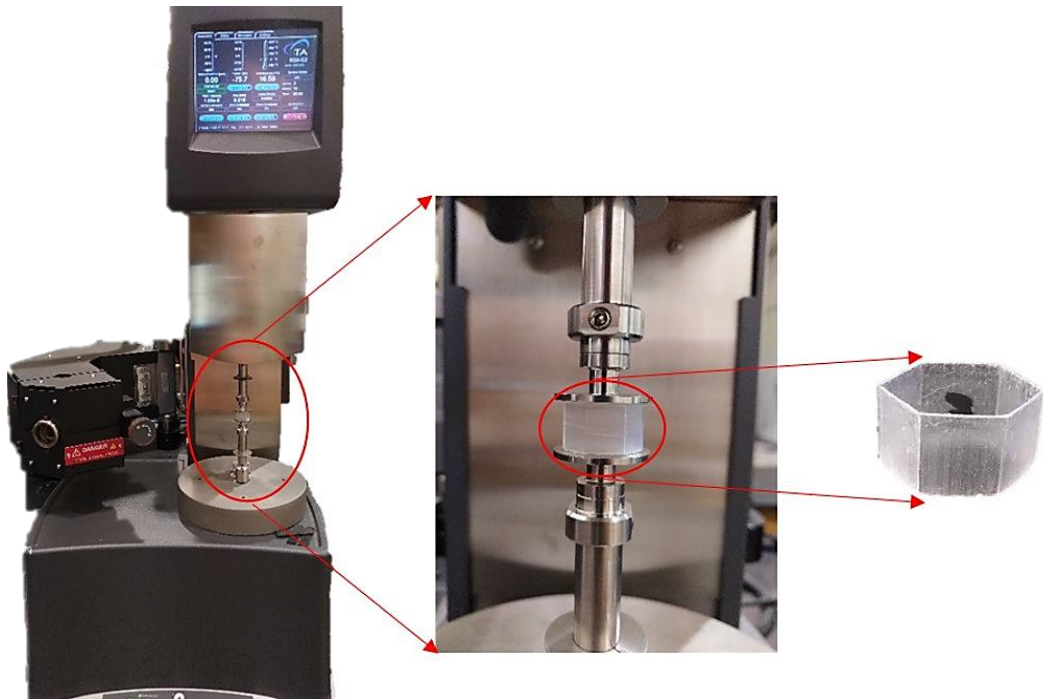


Figure 32. RSA-G2 Dynamic Mechanical Analyzer.

Figure 33(a) at room temperature compares the storage modulus of several makeshift cellular architectures to hexagonal honeycomb architectures with frequency sweep. Storage moduli of cellular architectures have been found to progressively improvement with improvements frequency. Figure 33 illustrates how several perfect cellular unit cellular designs differ from hexagonal honeycomb unit cellular in terms of normalized tan (delta) with wall thicknesses (b). The normalized tan (delta) in Figure 33 (b) was created, much like the normalized specific load in the comparisons of uniaxial compression.

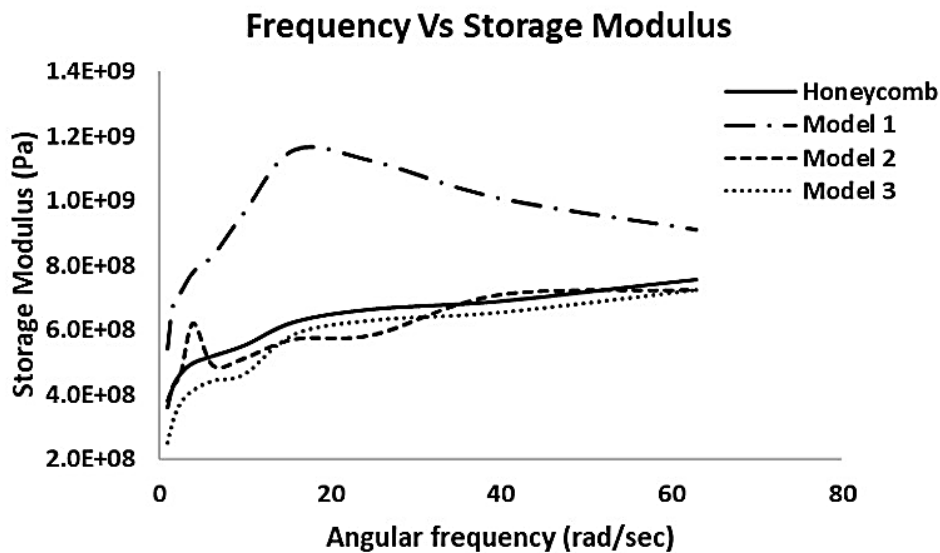
$$\tan(\text{delta})_{\text{normalized}} = \frac{(\tan(\text{delta})/\text{specific density})_j}{(\tan(\text{delta})/\text{specific density})_H} \quad (19)$$

where j = each individual unit cellular,

H = hexagonal honeycomb unit cellular.

When compared to hexagonal honeycomb unit cells, the ideal cellular unit architectures, such as Models 1, 2, and 3, exhibit reasonable performance (delta). Except for Models 1 and 3, all the architectures exhibit similar tendencies, with the storage modulus and tan (delta) rising with mass and frequency (delta). Due to their betterer natural frequencies and mass, architectures like Models 1 and 2 with the same overall volume display a larger range of damping characteristics, as shown in Figures 34(a) and (b).

(a)



(b)

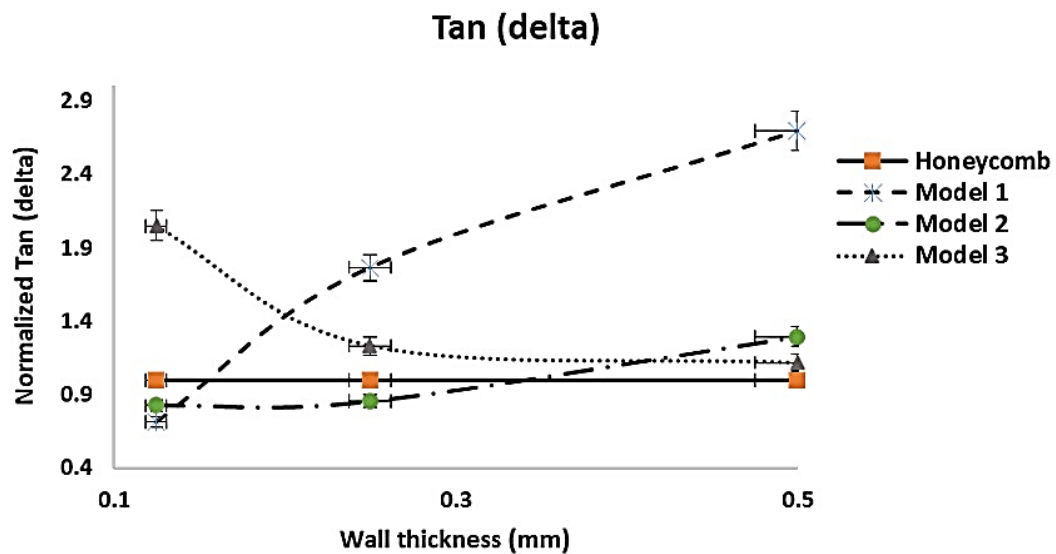
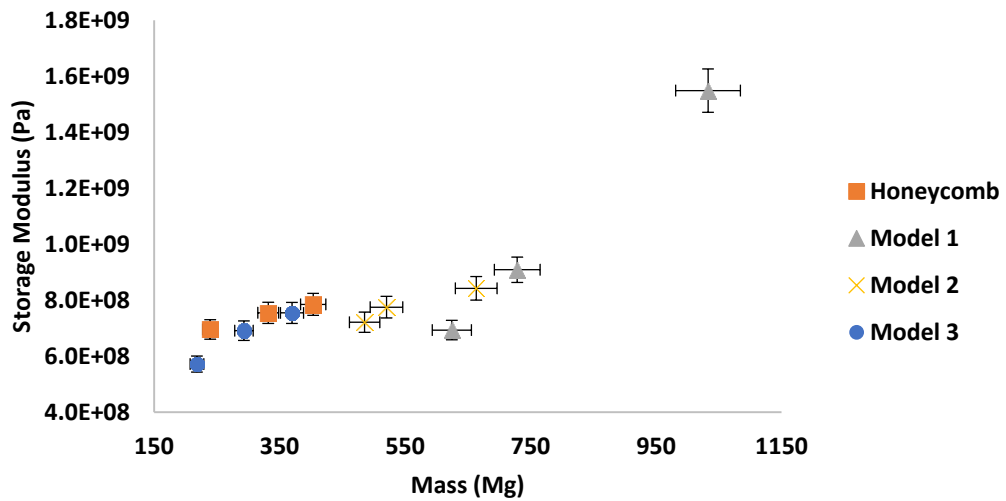


Figure 33. Storage modulus and Normalized Tan (delta) for different cellular architectures.

(a)

Mass Vs Storage Modulus



(b)

Mass Vs Tan (delta)

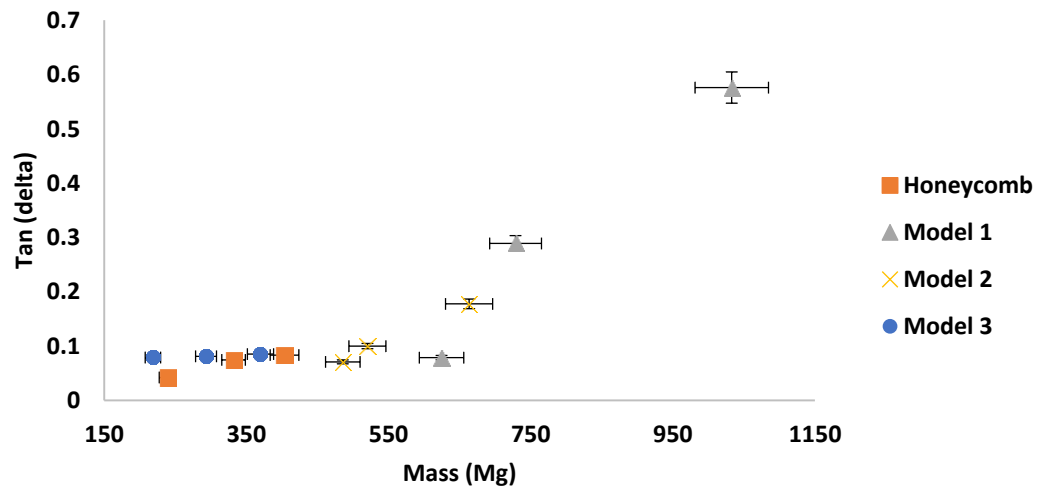


Figure 34. Storage modulus and Tan (delta) plotted with mass.

6.2.3. Impact test

To create cellular core sandwich architectures, the best cellular unit architectures were designed using an inverse design approach. As seen in Figure 35, all of the samples were created using extrusion-based additive manufacturing with PLA as the starting material. (b). The Instron Dynatup 8250 H V impact tester with a hammer weight of 11.2 kg and an impact velocity of 2 m/s [25] was used for the low velocity impact testing, as shown in Figure 35. (a). All sandwich architectures were created using Solidworks, and ANSYS LS-DYNA was used to do explicit non-linear finite element simulations of the low velocity impact tests. The total volume of the sandwich constructions is intended to be the same (120 mm 25.4 mm 4 mm).

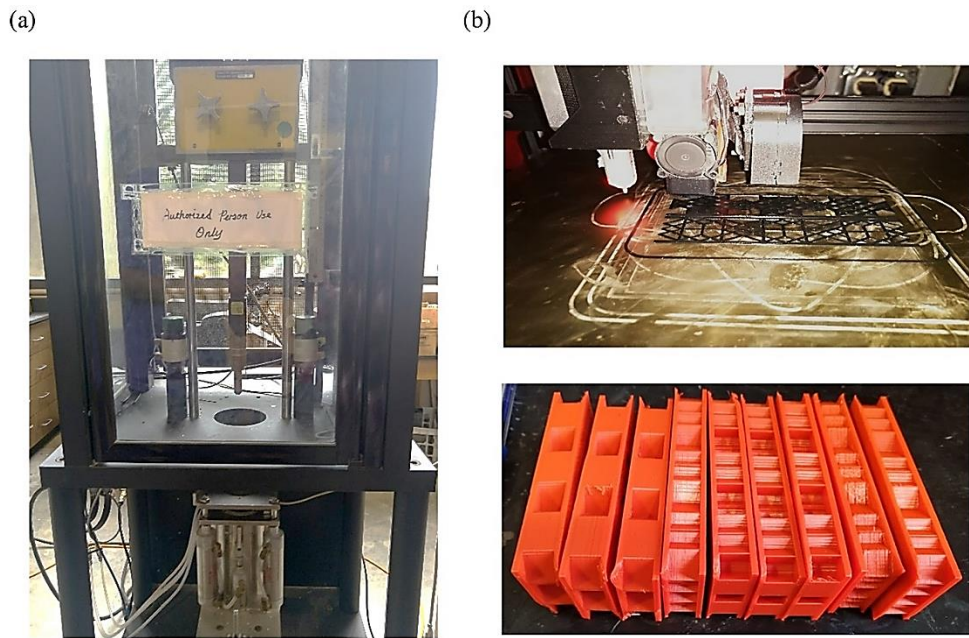


Figure 35. (a) Instron impact tester, (b) 3D printer.

6.2.4. Simulation and experimental results of low velocity impact tests

To determine the natural frequencies of the cellular unit architectures, the architectures are assumed to have constant stiffness and mass with no damping, time-varying force, deformation, or pressures applied. The natural circular frequency I derived from the equation of motion's solution may be calculated using the following equation [30] (see S10, (a) for the governing equations):

$$\omega_i = \sqrt{\frac{[K]}{[M]}} \quad (20)$$

$$f_i = \frac{\omega_i}{2\pi} \quad (21)$$

where $f_i = i^{th}$ natural frequency,

$[K]$ = stiffness matrix,

$[M]$ = mass matrix.

The capacity to mitigate energy is examined for the primary unit cells suggested by the inverse design. For impact energy comparisons, the normalized energy is determined by,

$$\text{Energy}_{\text{normalized}} = \frac{(\text{energy}/\text{specific density})_j}{(\text{energy}/\text{specific density})_H} \quad (22)$$

where j = each individual unit cellular,

H = hexagonal honeycomb unit cellular.

Figure 36 (a) demonstrates how, when flat, the best cellular architectures outperform hexagonal honeycomb designs by 300–800% in terms of normalized energy (i.e., with their walls perpendicular to the surface). This is because hexagonal honeycomb architectures typically have large gaps (porosity), but the best cellular unit architectures typically have web-like patterns that can fill the sandwich structure's impact zone. The best architectures perform between 50 and 350% better than the vertical hexagonal honeycomb structure (Figure 36(b)). Figure 36(c), which illustrates the superior performance of the primitive cellular architectures, displays the outcomes of experimental testing on sandwich constructions with the perfect cellular lattice core.

Figure 36 shows how, as the unit cellular wall thickness improvement, the normalized energy of the ideal sandwich panels steadily reduced (c). This is due to the fact that the mass of the architecture's improvements along with the wall thickness of the unit cells. Because the influence is limited to the central unit cellular of the sandwich structure, the mass improvement in the other unit cells within the sandwich structure has no impact on the overall performance (normalized energy) of the sandwich structure. As a result, when compared to wall thickness, this raise in sandwich structure mass has an impact on the normalized energy. The experimental findings for the impact test in the vertical direction are not presented in this work since machine learning is only used to improvise flat-oriented unit cells. In both strategies' computational and experimental studies in the flat direction (Figure 36(a), 36(c)), the number of unit cells used in the sandwich constructions causes a difference in the normalized energy in that direction. A single cellular unit is used in the analytical study to take into account the computational time and

power of the dynamic analysis, whereas multiple unit cells are used in the experimental study to meet the minimum dimensional requirements for specimens (120 mm 25.4 mm 4 mm) when using the impact testing machine.

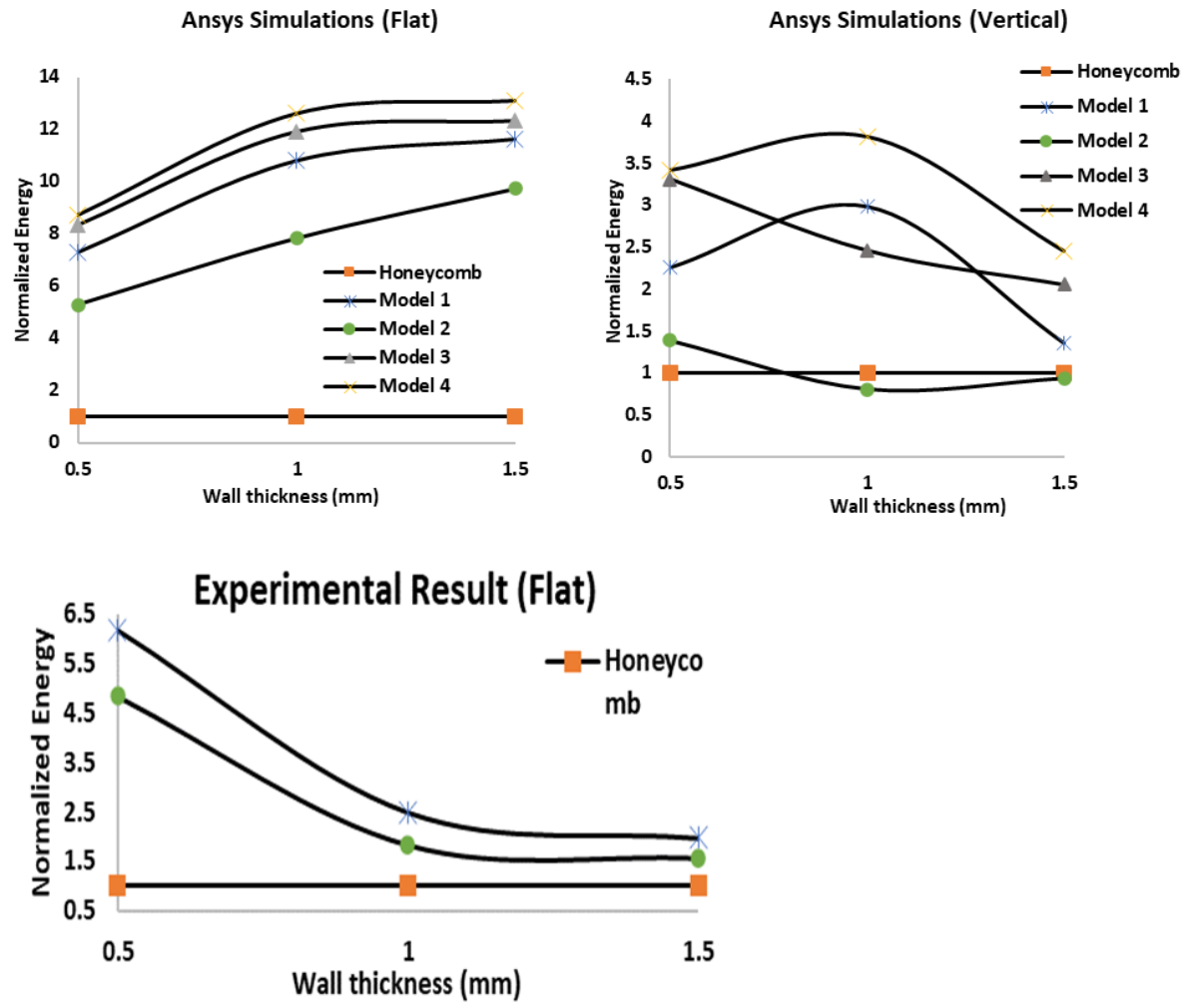


Figure 36. Numerical simulations for low velocity impact test.

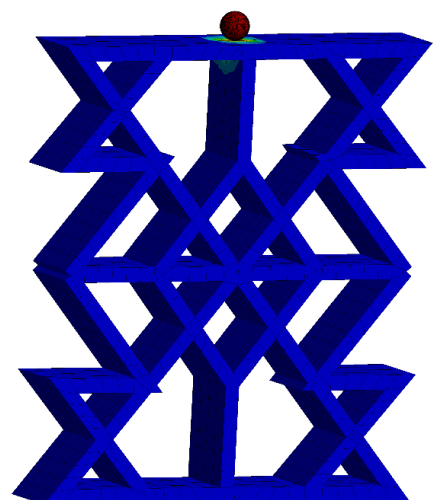
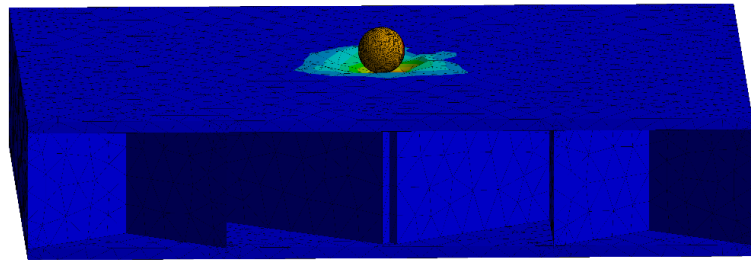


Figure 37. Ansys Impact test simulation flat (top), vertical (bottom).

Chapter 7. Shape Memory Architectures with Record High Recovery Stress

Shape memory polymers (SMPs) have expanded in usefulness in a range of technological domains since the phrase "4D printing" was first used in 2013 [94, 95]. Volumetric printing may be used to further improvement the printing pace of SMPs [96, 97]. The decent form recovery of 4D-printed SMP architectures is one of its advantages. For certain practical applications, such as serving as actuators in deployable architectures [98, 99] and as a crack-closing tool in damage self-healing in line with the close-then-heal (CTH) method [100, 101], stress recovery is better sought. Increasing SMPs' shape memory capabilities has been the subject of numerous studies. At various temperatures, a mixture of TPU (thermoplastic polyurethane) and PLA (polylactic acid) was investigated to improve PLA's shape memory characteristics. The PLA and TPU blend's elastic stress recovery has been found to be reduced by preformation temperatures [102]. In addition, the response of a brand-new PETG (poly-ethylene terephthalate glycol) polymer to both cold and hot temperatures was investigated. The findings indicate that hot programming has a betterer elastic stress recovery [103]. Nanocomposite or enthalpy as a method of energy storage has also been utilized in additional studies to raise elastic stress recovery [104, 105] [106, 107]. Because a better elastic stress recovery necessitates a better rubbery stiffness, form or strain recovery is reduced, leaving less room for expansion. Consequently, it remains challenging to develop new SMPs with better elastic stress recovery, better strain recovery efficiency, and better load carrying capacity.

With a few exceptions that concentrate on lattice truss constructions, the bulk of elastic stress recovery estimates in the open literature are based on test findings for solid materials like cubes or cylinders [108, 109]. In general load bearing capacity of a material can be improved in sandwich beams, T-beams, box beams, and I- beam architectures, rather than solid cuboid beams. As a result, if complex structures of SMP'S are 3D printed then the specific elastic stress recovery would improve as opposed to solid architectures.

Shape memory polymer (SMP) has previously been used to 3D print mechanically adjustable complex structures using Octet and Kelvin lattice truss unit cellular architectures [110]. SMPs were used to create auxiliary architectures that may be used in medical equipment and have changeable mechanical and architectural qualities [111]. A solid-solid phase shift that

includes hierarchically structured metamaterial was created [112] for application in programmable devices such as micro-actuators and grippers. By contrasting their mass, clasping load, regular recurrence, Poisson's proportion, and pressure load with other computational and exploratory outcomes, elective two-and three-layered auxetic designs have additionally been created [113]. Due to their architectural direction, numerous medical, sporting, and automotive devices utilize auxetic architectures' distinctive behavior [114].

A number of specific lightweight complex structures with enhanced buckling loads, compression strengths, energy mitigation, and natural frequencies under impact loads were covered in preceding chapters. Although some architectures with promising shape memory capabilities were anticipated, only a few architectural selection or improvisation strategies have been investigated thus far. Due to the distinctive thermomechanical and architectural characteristics of SMP complex structures, computational assessment can be too challenging, and experimental validation requires a lot of time with the complex architectures that comes along with multi-step thermomechanical processes.

This chapter proposes a simple design criterion for identifying primal complex structures with improvements shape memory characteristics. A structure must be resilient enough to tolerate higher programming strain and flexible enough to allow for bigger deformations (pre-strain) during programming in order to function optimally in shape memory. We initially thought about mainly flexural in nature's elements architectures to find a compromise between these two conflicting needs inside the lightweight constructions. The improved flexibility of twisted governed architectures, which has been demonstrated [115, 116], satisfies the criterion for a bigger dislodging. For application in passive morphing airfoils periodic hexagonal honeycomb architectures were examined due to their improved in-plane shear strength and shear strain [117]. It now satisfies the second need by optimizing primarily flexural in nature's component architectures with improvements strength or programmed stress. As a result, designs that emphasize flexural and offer more strength could be more capable of recovering from elastic stress. In order to determine the best architectures with the best strength and elastic stress recovery qualities, design spaces for thin-walled cellular unit architectures and 3D primarily flexural in nature's elements lattice truss unit cellular architectures are examined [126]. Although

stretch-ruled grid architectures and frail walled cell architectures with incredibly low relative thickness can display significant deformation through clasping, we do not evaluate these types of designs since they do not fit the criteria for essential programming load.

To examine design space that is huge, the preceding chapters show that there is a research gap in terms of creating methodologies, despite the fact that several cellular architectures with thin walls, auxetic characteristics and high strength were offered. A data-driven strategy may be substantially nearer to the global optima than topological improvisation strategies, which can result in perfect architectures. This chapter suggests a novel design improvisation method for identifying novel primal cellular architectures with thin walls that are superiorly strong and elastic in their ability to recover from elastic stress by utilizing supervised machine learning prediction models that were previously proposed and correlation analysis tools. Although many previous studies have used the models used in this work, to our knowledge no one has ever suggested combining these tactics for architectural improvisation. We used the ideal 3D lattice truss unit cellular architectures from our earlier study for comparison, where we improved them in terms of uniaxial and multiaxial strengths using machine learning prediction models and GANs. The optimum lattice truss unit cellular architectures for mainly flexural in nature's elements are chosen using Maxwell's stiffness of frames criteria. For the purpose of unit cellular categorization and selection, this criterion is then expanded to include cellular architectures with thin walls. The ideal architectures and recommended framework for inverse design are supported by numerical and experimental comparisons. Lattice truss unit cellular architectures that primarily flex under the influence of nature's elements and thin-walled cellular unit architectures both exhibit improved elastic stress recovery, excellent stretchability, and strength.

Cellular architectures with thin walls have stronger the out plane direction compression strength than lattice truss models like the Octet truss lattice, but they are weaker in the in-plane or lateral orientations (Figure 38). By looking at the cellular walls orientation in various thin-walled architectures, this is simply understood. Only a few walls contribute towards the strength for the in-plane direction, but all walls contribute to compression strength in the out-of-plane direction. Wall twisting or clasping is what causes delicate walled buildings to fail under pressure

loads. While flexural is not as terrible, buckling has the potential to cause catastrophic failure. Improved architectural packing, improved pressure recovery, and improvement stretchability may result from wall flexural. Due to the several ways in which the cell walls may be oriented, a thin-walled cellular structure's in-plane direction offers a wider range of stretchability.

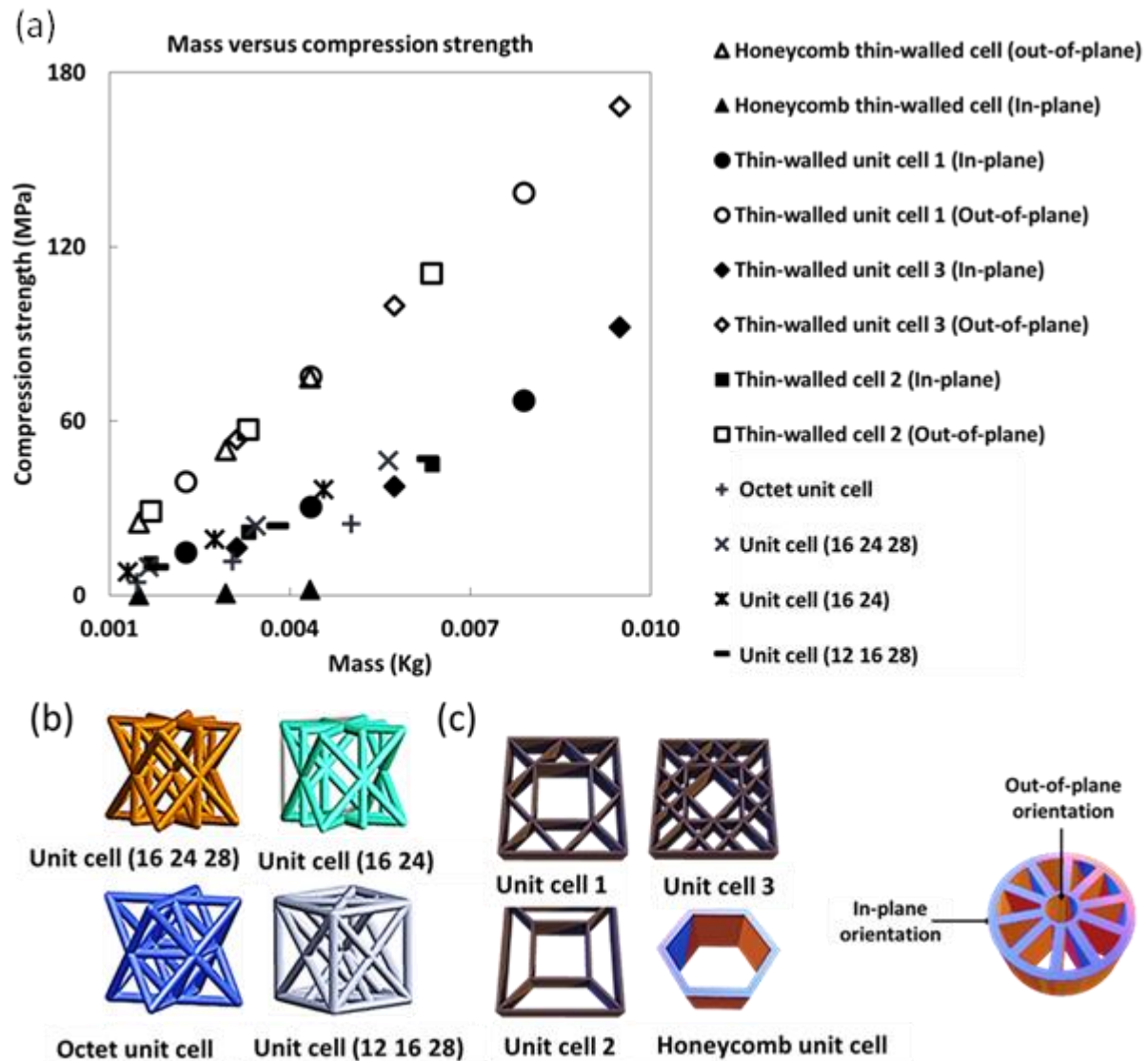


Figure 38. Comparisons of various lattice and cellular architectures under compression load.

Figure 38 compares the compressive yield strengths of different lattice truss unit cellular architectures and thin-walled cellular designs in both orientations. The total volume, rod diameters, and wall thickness of every unit cellular are all the same. A) illustrates how rod diameter and wall thickness improvement the compression strength of all unit cells. In

comparison to lattice truss unit cellular architectures, thin-walled cellular architectures have higher strength in the out-of-plane direction across identical mass ranges, but their strength in the in-plane direction is equivalent. Improved removals in the in-plane direction, which may be used practically in areas like energy retention, influence resilience, and better shape recovery qualities, are possible with delicate walled designs. This is supported by the porous nature of cell walls and the way that wall components deform in an in-plane manner.

In the phases that follow, the behavior of cellular architectures with thin walls in the in-plane direction is investigated and optimized for better stress recovery qualities. In order to examine a bigger area of architectural design, a RVE will first be used to build a database of probable thin-walled cellular architectures inside a design space (RVE). Second, machine learning prediction models that can forecast the FEA of any unit cellular inside the RVE must be created using a training database. The power and processing time required to forecast a property are considerably reduced by the machine learning prediction models. Thirdly, a proposed design criterion for identifying whether unit cells display stretching- or primarily flexural in nature's architectural behavior. In order to anticipate revolutionary lightweight designs with better strength and elastic stress recovery, a design framework based on inverse methodologies built on machine learning prediction models and correlation analysis tools will be created.

7.1. Materials and Methods

7.1.1. Database formation and fingerprinting

The quantity of the training data for machine learning models and correlation analysis tools must be at least a minimum for primordial performance. The input and output variables have a big impact on how big the training database is. The quantity of data necessary to train an effective archetype is more as the number of independent factors that affect the outputs rises. This section discusses the strategies we used to build the training database for predicting the FEA of cellular architectures with thin walls in addition to the fingerprinting strategy.

Certain boundary conditions should be created in order to cover a large range of undiscovered design space with complete FEA without making it too difficult for improvisation work to examine a wide variety of specific architectural designs. In order to do this, a RVE (RVE) with nine points (i.e., 2D points) is taken into account. By connecting any two pairs of neighboring locations, a total of 20 lines, or thin walls in 3D, may be created. Here, just the nearest neighbors are joined together to make a line for the purpose of simplicity. For instance, the line (12) may be formed by connecting locations 1 and 2, however points 1 and 3 cannot be connected because point 2 is among them. The RVE is mirrored into the horizontal and vertical axes for each variation of these lines, resulting in a huge Database with almost a million different thin-walled architectures. If non-nearest neighboring sites like 18, 19, and 19 could be connected, a total of 35 lines would be produced. The training Database would grow as a result, and more primitive topologies may be captured. In this study, we used 20 lines for simplicity and to demonstrate the machine learning framework exclusively.

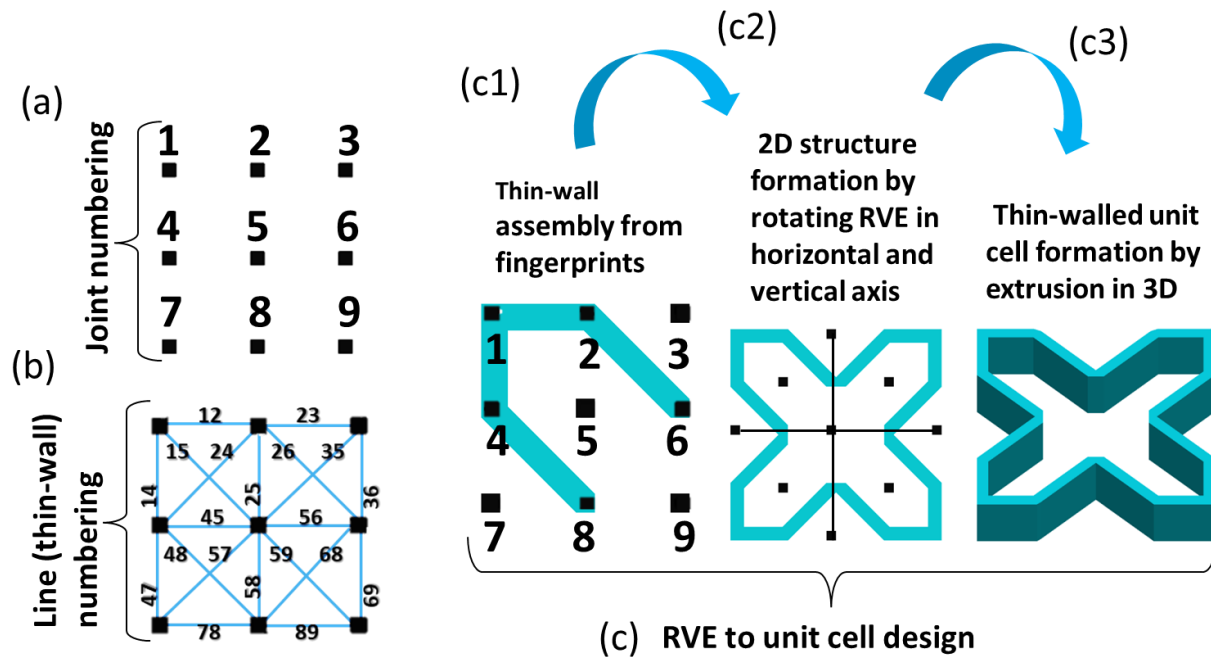


Figure 39. RVE for SMP thin-walled unit cells.

As both the inputs—the architectures—and the outputs—the essential mechanical characteristics of each structure are essential for training database for supervised machine

learning algorithm. Before the machine learning model can evaluate the data, the architectures must first be recognized in a distinctive way. Each structure is converted into a ML model-readable logical pattern of numbers by fingerprinting. The initial identifier of any structure in this study is the total of all the points that constitute the specific unit cellular that it creates inside the RVE. For instance, the thin-walled construction in Figure 2 has the fingerprint (12 14 26 48), where (12) represents the wall or line produced by the points (points) 1 and 2 that link it. Similar walls or lines are shown in figures (14), (26), and (48), which link the points 1 and 4, 2 and 6, and 4 and 8, respectively. Each structure built inside the RVE can have its own distinct logical fingerprint since the location of vertices and their numerical identifications are fixed. Examples of architectures and fingerprints may be found in Figure 40.

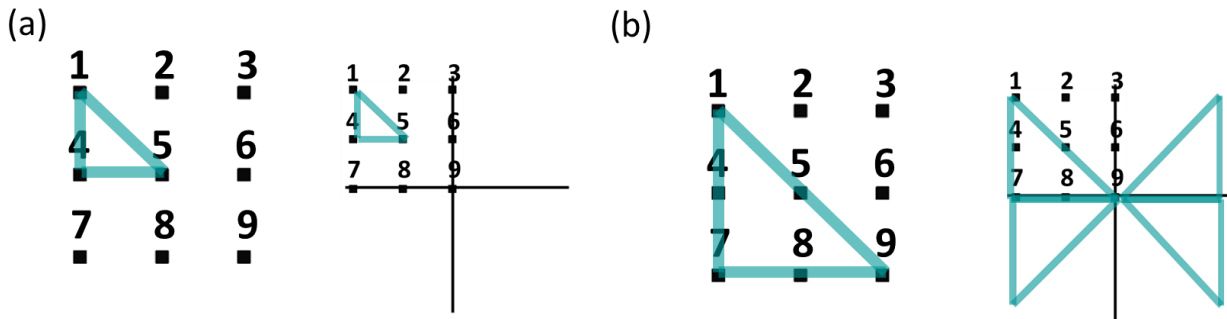
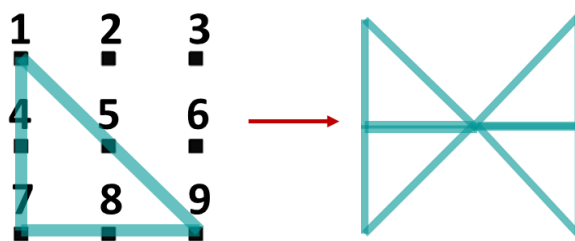
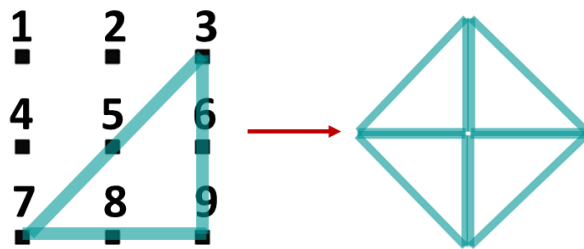


Figure 40. Sample thin-wall structure formation and fingerprinting method.

In Figure 40, (a) would have the fingerprint (15 14 45), but due to the absence of connections, it would not form a structure. Based on the method suggested in the paper, (b) is fingerprinted as (15 59 89 78 47 14) and has a workable structure. (15 59 89 78 47 14) leads to



(35 57 78 89 69 36) leads to



Even though they are distinct architectures, when tessellated to create an endless lattice, they produce the same lattice structure.

The above-mentioned strategy is used to collect fingerprints from all of the study's architectures. To create every potential structure for the RVE into a database, MATLAB's combination function is used. 2000 fingerprints are randomly selected from the untrained database to serve as the machine learning prediction analysis training database. Like "y," MATLAB functions "y = data sample (data, k)" are utilized to extract the training Database.

7.1.2. Forward ML prediction

The primary goal of this work is to anticipate the best thin-walled architectures with the highest elastic stress recovery. As was previously indicated, both experimentally and statistically measuring the elastic stress recovery of these architectures is a challenging and time-consuming operation [44, 45]. Structure production, experimental setup, and multi-phase recovery stress training are all necessary for the experimental analysis, which is time-consuming when there are several samples involved. Due to the multiple representation-fitting parameters, thermomechanical studies, and non-linear material FEA involved in numerical analysis, it can also be rather difficult [46–48]. Any of the traditional approaches cannot be used due to the size of the training Database.

The energy stored during programming and the total strain stored of a structure will highly influence the total elastic stress recovery. For this purpose because this is an architectural improvisation problem and the material characteristics, overall volume, and test boundary conditions for all architectures remain constant. Because the form fixity ratio, shape recovery ratio, and rubbery modulus are all dependent on the SMP, the elastic stress recovery for a certain SMP solely depends on the programming strain. Improvements deformation will result in more strain, which will improvement energy storage and decrease elastic stress recovery, to put it another way [118]. When the structure or one of its components fails, the maximum deformation occurs. to enter the uniaxial compression strengths of each structure in the training database together with their masses. Each of the 2000 thin-walled constructions is displayed and evaluated using the Workbench plan modeler. The training database is processed using a workstation with 32 GB of RAM and an i7 CPU, which takes between 75 and 85 person-hours to complete. For consistent outcomes, mesh convergence analysis is performed, as seen in figure 41. In order to decrease complexity and processing time that would improvement if viscoelastic characteristics were taken into consideration, the numerical analysis merely takes into account the elastic characteristics of the underlying material. After a material has been chosen, the programmable strain of the architectures—which is controlled by the quantity and orientation of their elements—determines their elastic stress recovery. Therefore, the archetype must be applicable independently of the characteristics of the materials.

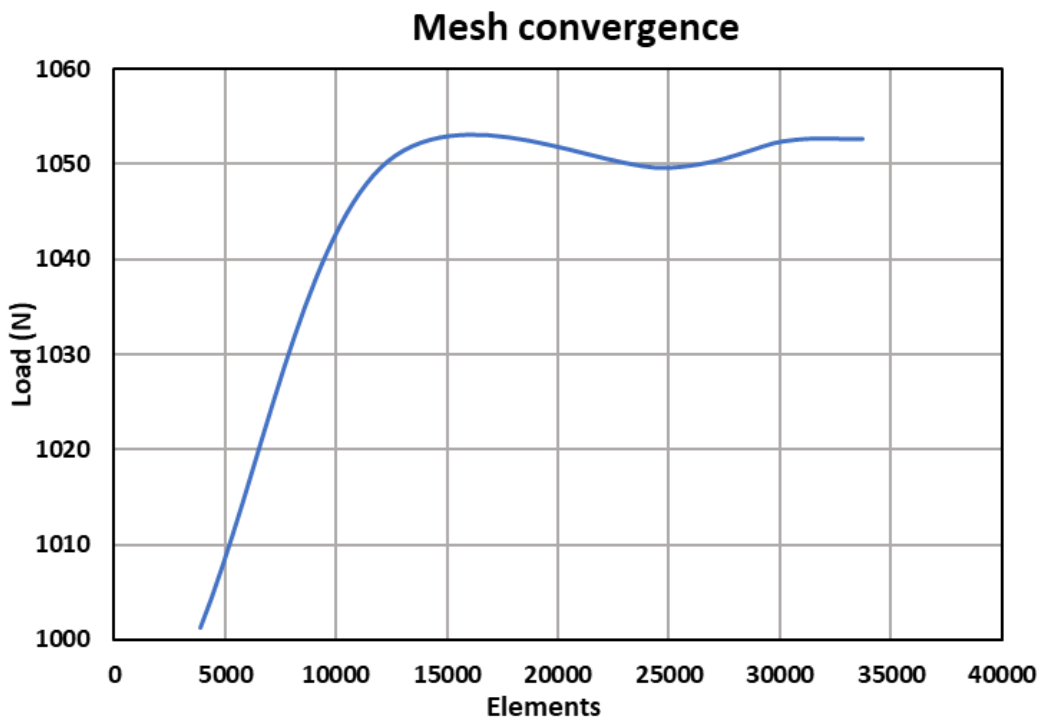


Figure 41. Mesh convergence analysis.

The MATLAB Regression Analysis tool is used to assess the prediction accuracy of various machine learning algorithms with the training Database after creating the training Database with the input fingerprints, output mass, and compression strength parameters. The Gaussian Process Regression (GPR) archetype beat competing machine learning models like ensemble trees and Support Vector Machines (SVM) With an RMSE of less than five percent and an R-squared value of 0.98 for both the mass and compression strength parameters. View Figure 42. The GPR archetype was trained using a training set of 2000 fingerprints, and it now has a prediction accuracy R-squared value of 0.98. The slanted strong lines reflect immaculate figures, while the blue spots (\bullet) show the perceptions. A solid relapse archetype should be visible in the roughly uniform dispersal of the perceptions along the best expectations. See Tables 10, 11 for archetype parameters and comparisons. A set of random variables are utilized by the GPR archetype with a Gaussian distribution to make evaluations. With architectural data and their evaluations of

mechanical property, the GPR models have already been shown to perform better than other supervised machine learning prediction models.

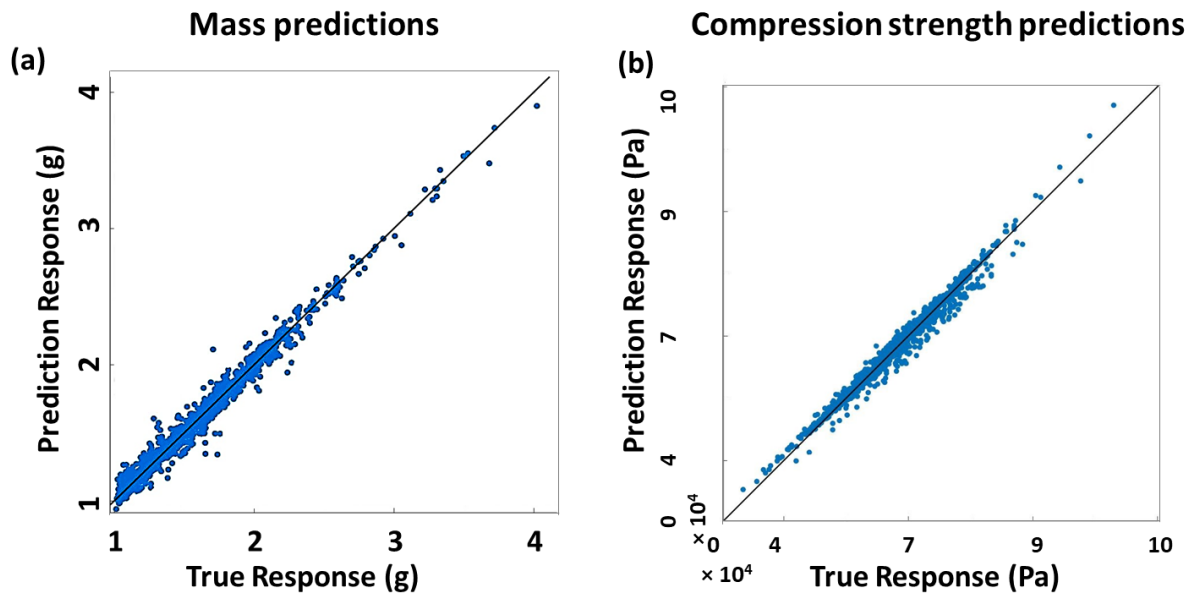


Figure 42. GPR models for (a) mass and (b) compression strength evaluations.

Table 10. Machine learning archetype parameters

Archetype Type	GPR (Gaussian Process Regression)
Basic function	Constant
Kernel function	Matern 5/2
RMSE	Mass - 0.0564, Compression strength – 0.02084
MAE (Mean Absolute Error)	Mass – 0.08, Compression strength – 0.014485
Prediction speed	~5700 orbs/sec
Training time	503.23 sec

Table 11. GPR archetype for mass and compression strength evaluations

Uniaxial compression strength						
Machine learning strategy	Training Database			Testing Database		
	RMSE (Root Mean Square Error)	R ²	MAE (Mean Absolute Error)	RMSE (Root Mean Square Error)	R ²	MAE (Mean Absolute Error)
Matern 5/2 GPR (Gaussian Process Regression)	0.02084	0.98	0.014485	0.021457	NA	0.0189
Ensemble (Bagged Tree)	0.02488	0.92	0.010154	0.028471	NA	0.0154
Cubic SVM (Support Vector Machine)	0.02321	0.89	0.01356	0.035481	NA	0.0245
Mass						
Matern 5/2 GPR (Gaussian Process Regression)	0.0564	0.98	0.08	0.045	NA	0.084
Ensemble (Bagged Tree)	0.0721	0.96	0.1455	0.084	NA	0.1247
Cubic SVM (Support Vector Machine)	0.0785	0.92	0.1487	0.041	NA	0.14

7.1.3. Selection criterion

After selecting the best machine learning models, they can quickly and effectively predict the architectural attributes of the remaining designs from the entire Database. The regression archetype can now be utilized to calibrate the first requirement for primal elastic stress recovery, or any structure's compression strength within the defined design space. The second requirement, the largest deformation of a structure prior to breakdown, also affects the primal elastic stress recovery. For this purpose, we will refer to the study of lattice truss architectures and how they behave depending on the number of points and components. Under axial loading, the columns or elements of a lattice truss structure typically bear the load. Based on Maxwell's criterion for the rigidity of frames, lattice truss architectures can either be dominated by stretching or flexural (Ems. 1, 2) [119, 120]. It is important to point out that pin-jointed architectures were the initial application of Maxwell's criterion. Points that are printed in 3D are not typically pinpoints. Also, the archetype has notable exemptions, and clasping mists Ashby's underlying thinking for picking the rule. A number of researchers have recently expanded Maxwell's criterion to include 3D printed objects with frozen, rigid, or flexible points [121, 122]. Using Maxwell's criterion as a starting point, we selected unit cells that were dominated by flexural or stretching for this study.

$$M=b-2j+3, \text{ 2D architectures (frames)}$$

$$M=b-3j+6, \text{ 3D architectures} \quad (24),$$

where b is the number of truss members and j is the number of frictionless points. In this case, the structure is dominated by stretching if $M > 0$, and by flexural if $M < 0$.

While predominantly flexural in nature's elements architectures fail due to stretching or buckling in the columns or rods, predominantly stretching in nature's elements designs fail mostly due to the rod flexural. The framework's stiffness is the reason predominantly stretching in nature's elements architectures are stronger and more durable than predominantly flexural in nature's elements ones, according to a number of studies. In Chapter 4, we discussed a number of novel lattice truss unit cellular architectures that, in terms of compression strength characteristics, performed better than the standard Octet truss lattice unit cellular. We did not examine the elastic stress recovery qualities of the architectures or SMP print them. Contrary to

what has been written up to this point, additional research has shown that some of the ideal architectures, which are dominated by flexural, have a relative compression strength that is comparable to or even betterer than that of their predominantly stretching in nature's elements counterparts. We adopted a RVE with 162 truss members and 27 points from our previous research [20].

Out of the 550-lattice truss unit cellular architectures that can be created within this RVE, it has been designed that the ideal predominantly flexural in nature's elements lattice truss unit cellular architectures perform better under uniaxial compressive than any other predominantly stretching in nature's elements lattice truss unit cellular architectures, including the Octet unit cellular. More details about the RVE and mass comparisons among various ideal lattice truss unit cellular architectures are provided in our previous work.

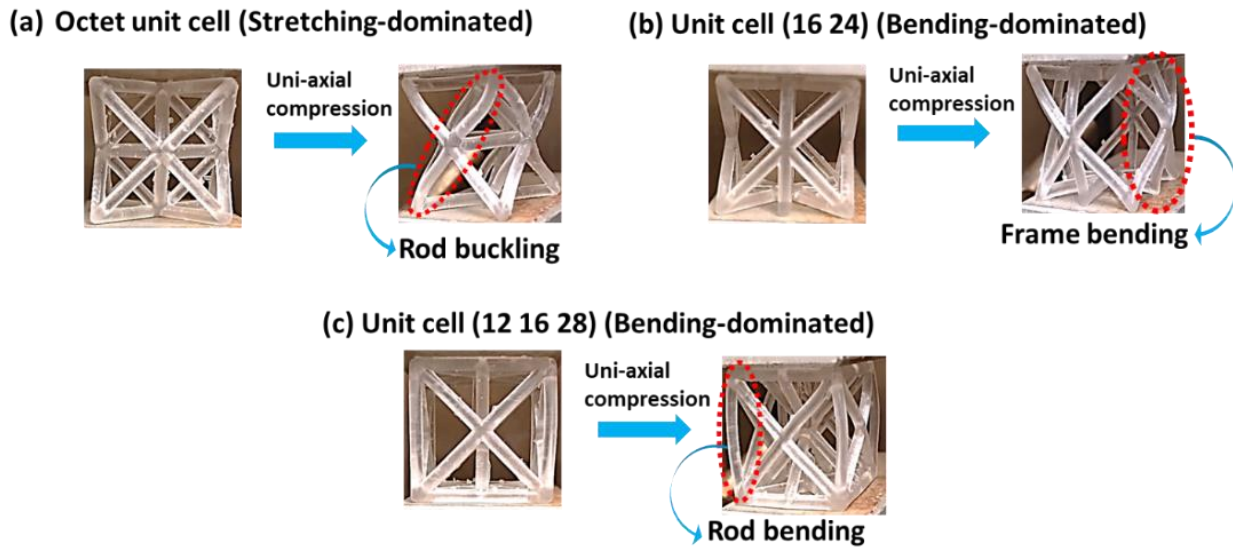
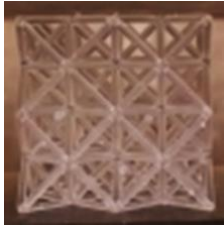
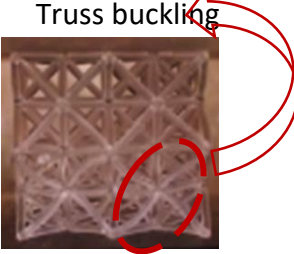
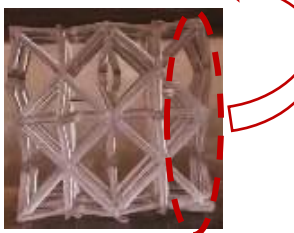
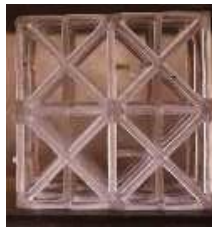
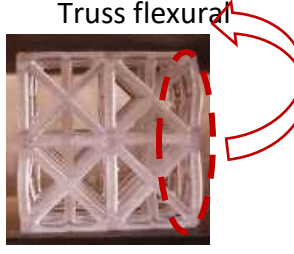


Figure 43. Behavior of predominantly stretching in nature's elements and predominantly flexural in nature's elements.

With predominantly flexural in nature's elements lattice truss architectures, numerical and experimental comparisons are presented in Section 4.1. These ideal unit cells that are dominated by flexural have flexural responses that are strong, light, and flexible, making them particularly useful as shape memory architectures. The undesirable buckling phenomena of the columns or rods in the lattice truss structures can be mitigated by substituting biomimicry

columns with betterer buckling strengths for the typical cylindrical elements [30]. To contrast with the Octet truss lattice structure, we selected a variety of the best predominantly flexural in nature's elements lattice truss unit cellular architectures from section 4.3 of chapter 4. Figure 43 depicts the 3D-printed unit cells prior to (left) and following uniaxial compression-induced deformation (right). The Octet unit cellular demonstrates predominantly stretching in nature's elements behavior with local rod buckling, in contrast to the hypothesized predominantly flexural in nature's elements unit cells, which exhibit either global or local rod flexural. It is important to keep in mind that during testing, abrupt flexural is referred to as buckling; A predominantly flexural in nature's element's structure is one in which the number of flexural raises with load.

Table 12. Stretching dominated vs flexural dominated lattice truss with 4×4-unit cells

Before uniaxial compression	After uniaxial compression
(a) 4×4 Octet truss lattice (Stretching dominated) 	 Truss buckling
(b) 4×4 16 24 lattice (Flexural dominated) 	 Frame flexural
(c) 4×4 12 16 28 lattice (Flexural dominated) 	 Truss flexural

Because of the nearby clasping and twisting way of behaving of the slim walls, particularly in the out-of-plane direction, there are right now no grouping models for meager walled cell unit cells, nor was Maxwell's rule utilized. However, even though local wall flexural, or buckling is more apparent in the in-plane direction, the thin-walled unit cellular may globally behave like a 2D frame. We utilized the 2D Maxwell's criterion for frame stiffness (Eq.) to support this. 23) to construct architectures that were distinguished as thin-walled cellular unit architectures that were flexural- and predominantly stretching in nature's elements while neglecting the local flexural and buckling modes. These cells were characterized by their flexural and stretching dominance. We printed these unit cells with a commercial polymer (Clear) and stereolithographic additive manufacturing (Formlabs, Form 3 model) to observe RVE how they behaved during uniaxial compressive tests (refer to Table 13 for material characteristics).

For each structure, a uniform cell wall thickness and a test speed of 0.5 mm/min are maintained. The structure depicted in Figure 44 (a) is categorized as predominantly stretching in nature's elements because M is greater than zero, while the structure depicted in Figure 44 (b) is categorized as predominantly flexural in nature's elements because M is less than zero ($b=24$, $j=21$). Figure 44(a) depicts architectures that are not improvised; They are merely utilized to demonstrate the architectures' behavior. 4 by 4 cellular architectures exhibit similar behaviors (Table 13). The solid lines represent comparisons of load and deformation, while the dotted lines represent comparisons of deformation and time. The predominantly flexural in nature's elements unit cellular - has lower load bearing capabilities, larger deformations, and flexible behavior in the in. In addition, the unit supports the behavior of flexural cellular in (b) because it takes longer to fail (300 seconds) than the behavior of stretching is simulated by the unit cellular in (a). In addition, while in (a) the load decreased rapidly, indicating the possibility of certain columns breaking, in (b) it decreased gradually, indicating flexural.

The predominantly stretching in nature's elements thin-walled structure in Figure 44 (a) fractures at the peak stress, whereas the predominantly flexural in nature's element's structure fractures both globally and locally in Figure 44 (b). Furthermore, Fig. 44(b) demonstrates that despite having a longer lifespan and greater deformation than the predominantly flexural in nature's element's structure, the predominantly stretching in nature's elements cells have a

lower load carrying capacity. Consequently, cells that have flexural as their predominant FEA true satisfy the requirements for greater deformation. The two designs in Figure 44 are not ideal, as was at that point referenced. They are being utilized merely as examples.

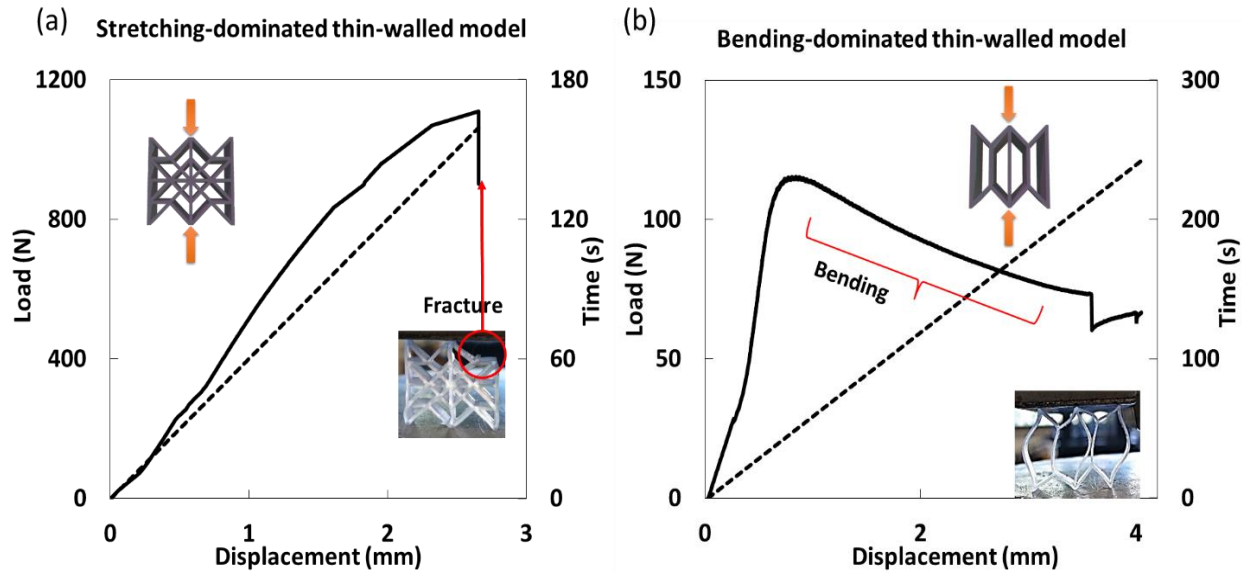
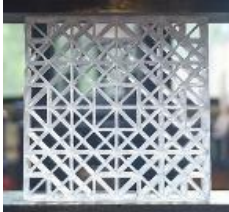
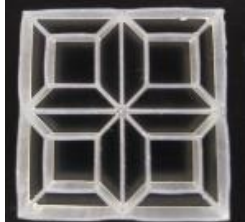
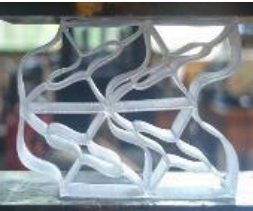


Figure 44. Experimental load, deformation, and time comparisons of thin-walled unit cells under uniaxial compression.

Table 13. Stretching dominated vs flexural dominated thin-wall cells with 4×4-unit cells

Before uniaxial compression	After uniaxial compression
(a) 4×4 Stretching dominated structure 	
(b) 4×4 Flexural dominated structure 	

(table cont'd.)

Before uniaxial compression	After uniaxial compression
(c) 4x4 Stretching dominated structure (From unit cellular – 5) 	
(b) 4x4 Flexural dominated structure (From unit cellular – 2) 	

In this work, the predominantly flexural in nature's elements architectures will be improvised to have betterer strength and deformability, which could lead to betterer elastic stress recovery. The assumption that cellular architectures with thin-walls in the in-plane direction can be included in the 2D Maxwell's criterion for frames to classify cellular architectures with thin-walls as either predominantly flexural in nature's elements or predominantly stretching in nature's elements architectures is supported by these experimental findings. Because it was first suggested for pin-joined architectures, to apply Maxwell's criterion to cellular architectures the forthcoming assumptions were made with thin-walls in the in-plane direction: 1) Any localized buckling or flexural of the thin walls shall be neglected. 2) When evaluating the general architectural behavior in the in-plane direction, the criterion should only be utilized as a preliminary screening method. It is important to point out that predominantly flexural in nature's elements models also exhibit local rod buckling, which is catalyzed by architectural flexural as a

whole. Notwithstanding, the general extending like way of behaving of the design causes the locking of bars in extending overwhelmed frameworks.

By applying this criterion, predominantly flexural in nature's elements architectures with betterer load carrying capacities (compression strengths) can now be constructed, resulting in ideal cellular architectures with thin walls that are flexible and robust. These unit cells could be utilized in practical implementation that require better strength and better recovery from stress. In order to lessen the thin walls local buckling, we developed biomimetic wall architectures that resemble huge clam shell seashell architectures. Figure 45 depicts the biomimicry wall designs and comparisons.

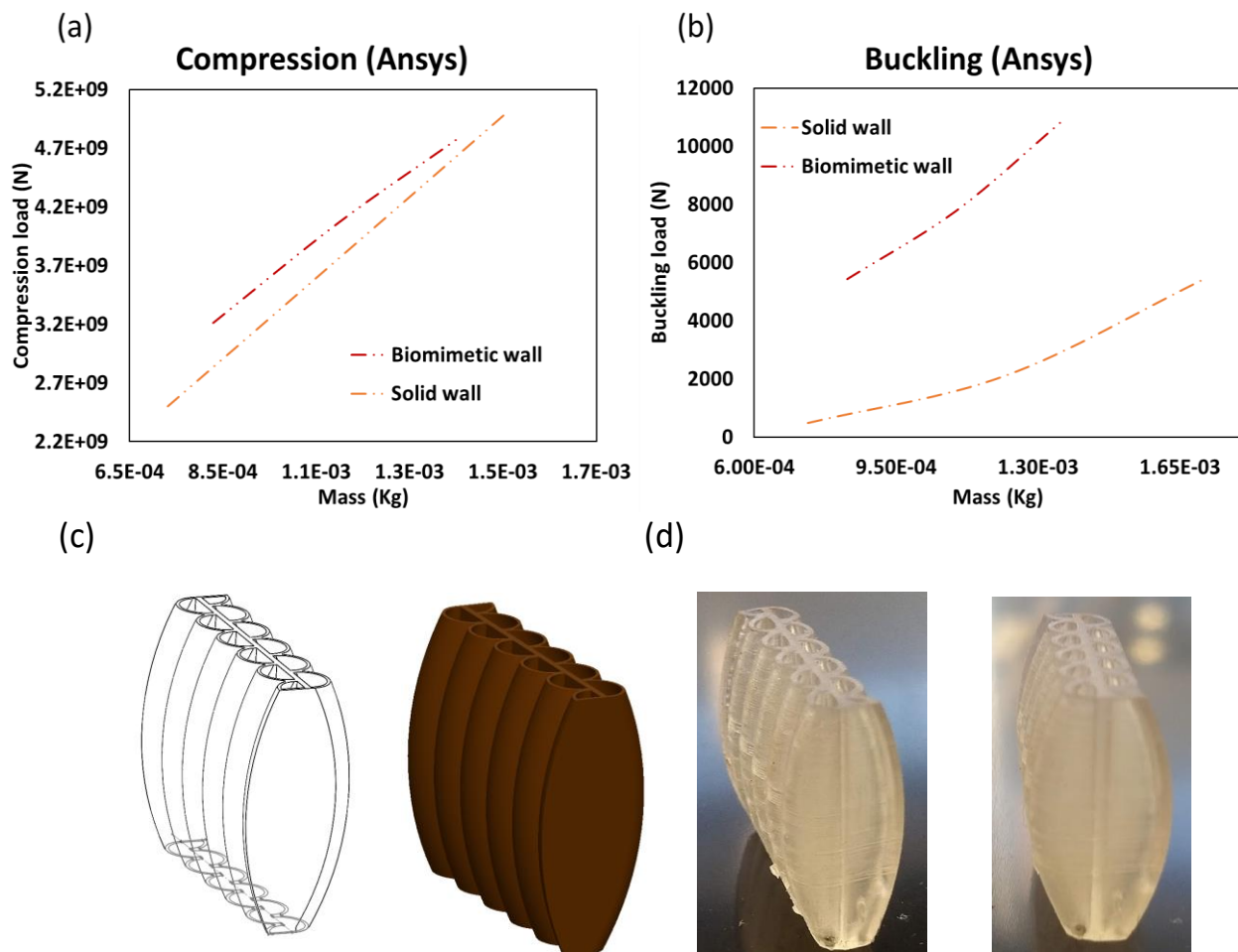


Figure 45. Comparisons of biomimicry wall inspired from gain clam seashell.

7.1.4. Inverse design framework

To produce novel lattice truss unit cellular architectures with better strength and cellular unit architectures with better energy mitigation, we previously developed A design framework using inverse methods. Combining machine learning prediction models with GANs enabled us to accomplish this. GANs offer specific architectures that are closer to the global optimum, whereas machine learning prediction makes property evaluations simpler and faster. Despite the GANs' excellent track record, they may necessitate time-consuming coding and training procedures. In addition, the inverse design framework developed in chapter 4 using GANs would build a set of desirable designs by repeatedly optimizing a set of inputs, necessitating multiple improvisation phases, as opposed to locating the best possible solution within the design space. This study's design space is large, but it is limited by a specific boundary condition (like the RVE, which limits the number of designs to 750k). Consequently, utilizing measurable devices like relationship examination can diminish the intricacy of the opposite plan issue and draw much nearer to the worldwide optima.

For this study, the inverse design framework is created by combining a correlation analysis and ML prediction models for predicting the unit cellular attribute, as shown in Figure 46. The inverted design framework is created by combining the selection criterion, correlation analysis, and ML regression models. Initially, a training Database was utilized to build machine learning prediction models that could predict the mechanical and architectural characteristics of the cellular architectures with thin walls. The inverse design framework is created by utilizing Maxwell's criterion to extract flexible architectures and correlation analysis to produce contemporary designs with the better possible strength. The best thin-walled unit that is flexible and strong will be the framework's output, and its input will be the desired mechanical qualities. See Figure 47 for a flowchart representation.

Correlation analysis is a method (statistical) that looks at how an independent and a dependent variable relate to one another. Spearman correlation analysis has been utilized in the past to study the connection among the mechanical and architectural characteristics of shale (clastic sedimentary rock) and its mineral and elemental composition [123]. The impact of the material qualities has been sure presentative volume alimented utilizing Pearson relationship

investigation (straight), which matched the trial discoveries of fiber supported cementitious materials [124]. With evaluations being 88% accurate [125]. In the healthcare industry the correlation analysis has been widely utilized to identify the variables that have the greatest impact on emergency ward utilization. A better correlation indicates that the independent variable influences the dependent variable in a significant way. In this review, the reliant variable (pressure strength) is the reliant variable, and the free factors (significant primary parts) are the autonomous factors that might influence the reliant variable (pressure strength). Spearman correlation, a monotonic analysis, was utilized in this investigation due to the nonlinear nature's elements of the data. The correlation non-parametric measure among the two variable ranks is taken into consideration when performing a Spearman correlation analysis [61,62]. The Spearman correlation coefficient (R_s) is defined by the following formula:

$$r_s = 1 - \frac{6 \sum d_i^2}{N(N^2 - 1)}, \quad (25)$$

where d is the difference among the two ranks of each observation, and N is the number of observations.

In order to carry out inverse design framework with correlation analysis, the masses and compression strengths of ten sub-Databases comprising one hundred fingerprints that were selected at random are retrieved. In order to identify the components that have a greater impact on the effective compression strength, correlation analysis is applied to all sub-Databases. The elements with the greatest influence (r_s close to 1) may be selected for new cellular architectures with thin walls. As opposed to GANs, which would like to propose a few confined ideal thoughts north of a few cycles, this will concentrate the streamlining model and draw it much nearer and quicker to the worldwide optima. The framework's prediction accuracy on various subsets is evaluated using correlation analysis (10). The end result will be novel, thin-walled, lightweight architectures with raised elastic stress recovery and enhanced strength and stretchability.

Using correlation analysis, the design objective of this work is to predict orthotropic cellular architectures with thin-walls with the better strength within the RVE that are flexural-dominated. Maxwell's criterion (Eq.) is utilized to extract a predominantly flexural in nature's element's structure. 23). Utilize machine learning prediction models to estimate the designs' mass and strength (Maxwell's criteria validations are shown in Table 14).

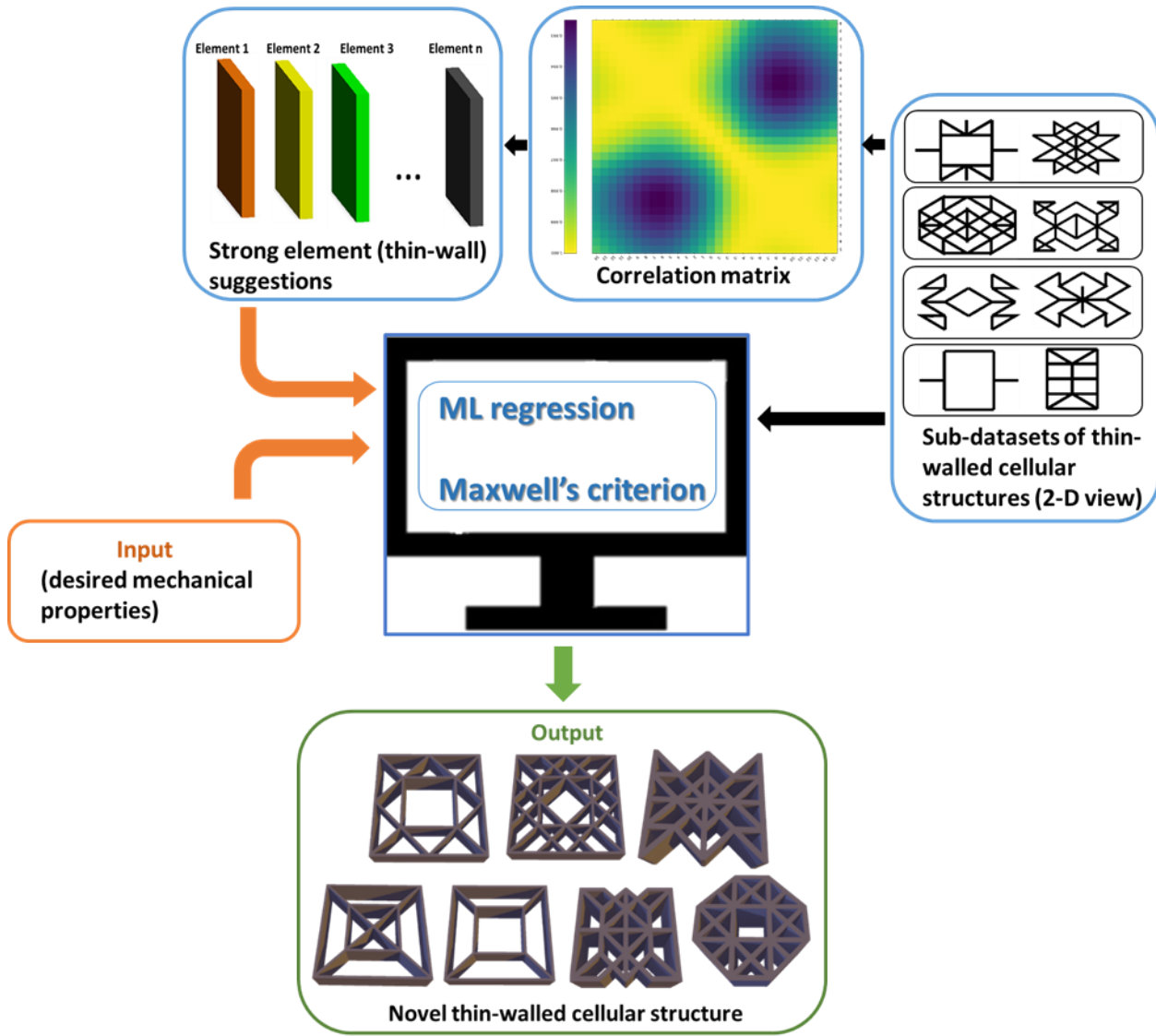


Figure 46. Inverse design framework for thin-walled architectural improvisation.

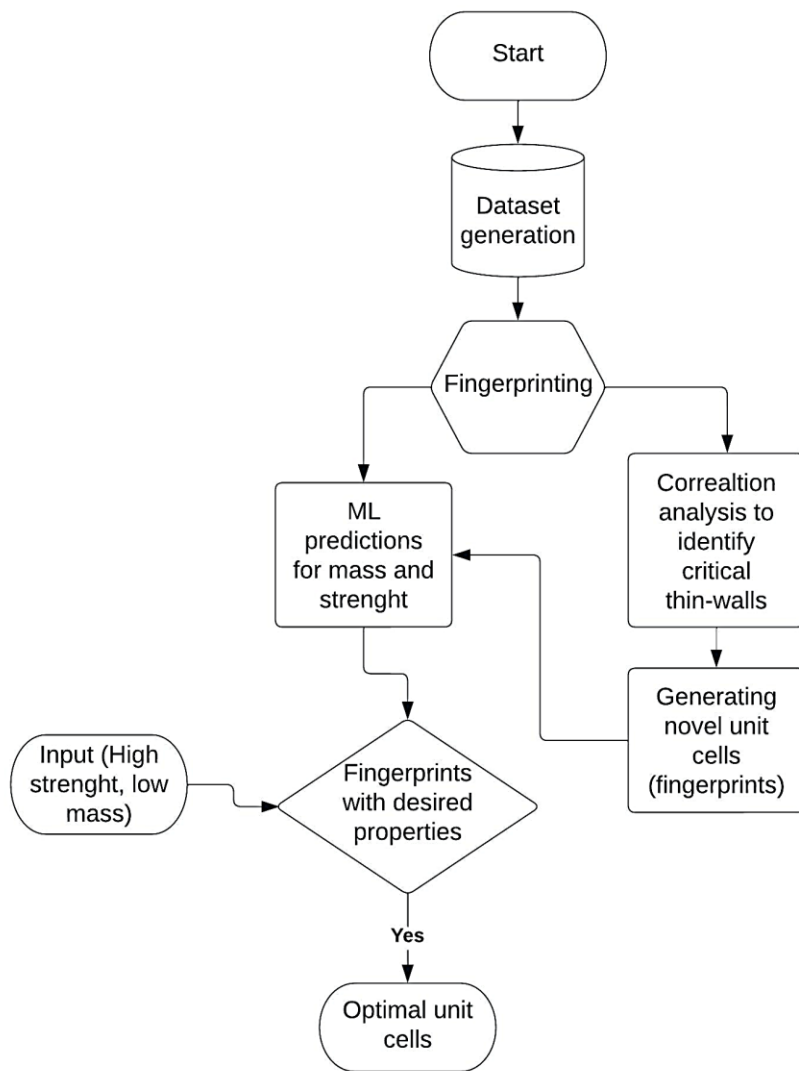


Figure 47. Flow chart for inverse design.

Table 14. Maxwell's criterion validation

Octet	$j = 14, b = 36$ $M = 36 - 42 + 6 = 0$	Stretching dominated ($M = 0$)
16 24	$j = 23$ $b = 48$ $M = 48 - 69 + 6 = -15$	Flexural dominated ($M < 0$)
16 24 28 (table cont'd.)	$j = 22$ $b = 42$	Flexural dominated ($M < 0$)

	$M = 42 - 66 + 6 = -12$	
12 16 28	$j = 23$ $b = 48$ $M = 48 - 69 + 6 = -15$	Flexural dominated ($M < 0$)
Cellular architectures with thin walls		
1	$j = 24$ $b = 36$ $M = 36 - 48 + 3 = -9$	Flexural dominated ($M < 0$)
2	$j = 24$ $b = 28$ $M = 28 - 48 + 3 = -17$	Flexural dominated ($M < 0$)
3	$j = 24$ $b = 36$ $M = 44 - 48 + 3 = -1$	Flexural dominated ($M < 0$)
Hexagonal honeycomb	$j = 11$ $b = 12$ $M = 12 - 22 + 3 = -7$	Flexural dominated ($M < 0$)

The RVE demonstrates that the total number of components condenses to 12 to extract orthotropic symmetry-containing structures. After conducting correlation analysis on 10 subsets, each containing 100 different fingerprints, elements 58, 15, 14, 47, 35, 26, 68, 59, 36, 25, 24, and 69 are projected to have the stronger correlation with the compression strength, to element 58 positioned the better and element 69 ranked the lowest for all the subsets. Now, orthotropic cellular architectures with thin walls are developed and assessed using the first four (58, 15, 14, 47), fifth (58, 15, 14, 47, 35), and seventh (58, 15, 14, 47, 35, 26) elements. These are shown in the following sections. For instance, the cell of the fingerprint (14 47 12 23 15 58 56) designated as "2" in Figure 38 is catalyzed by the first four elements (58, 15, 14, 47). Here, it is assumed that the elements 12, 23 and 14, 47 form an orthotropy. Likewise, 56 is automatically employed to

construct an orthotropic pair with 58. It can be understood as follows for the improvisation statement's analytical representation:

$$yfit = \text{trainedModel.predictFcn}(\text{Corel 1}, \text{Corel 2} \dots \text{Corel n}); \quad (26)$$

$$\text{Max} (\text{Corel 1}, \text{Corel 2} \dots \text{Corel n}) = \text{global optima}. \quad (27)$$

A Function used in the process of predicting mechanical characteristics of new fingerprints produced by Corel 1, Corel 2, and correlation analysis is called "yfit" in this instance. As was said in the paragraph above, correlation analysis produces several subsets of fingerprints. The localized fundamental solution is the highest of each subset produced by the correlation analysis up until no more increase in the mechanical features can be made; at this point, RVE or being global inside the Database is the best answer.

With the help of Python command prompt and Python commands we were able to manually filter the entire Database to hard code and extract the best cellular architectures with thin walls to evaluate the effectiveness of our architecture. It is noted that the unit cellular labeled "1" in Figure 1 is the orthotropic, predominantly flexural in nature's elements unit cellular with the better specific strength within the RVE. This unit cellular is one of the ones that the improvisation framework has suggested. As a result, this framework can be regarded as workable for issues involving this kind of improvisation.

7.1.5. Additively manufacturing

With the utilization of added substance producing, we made a few ideal grid unit cells, 4 by 4 cross section architectures, slender walled unit cells, and 4 by 4 dainty walled cell designs to affirm the hypotheses and models. The thin-walled lattice and cellular designs from the previous section are 3D printed using a shape memory polymer to produce architectures with improved elastic stress recovery due to their strength and stretchability. In addition to a uniform height, each unit cellular is constructed with a distinct element diameter and wall thickness. The size of the lattice truss unit cellular architectures is 101010 mm, whereas the size of the cellular architectures with thin walls is 10104 mm. The dimensions of the four-by-four cellular architectures with thin-walls and the four-by-four lattice truss architectures are 20 by 20 by 20 millimeters, respectively. Additionally, solid cylinders measuring 15 millimeters in height and 8 millimeters in diameter were 3D printed to test the bulk polymer against the cellular

architectures with thin walls. The SMP that was utilized in this investigation is made by combining EPON 826 resin (40%) and tris[2-(acryloyl) ethyl] isocyanurate (60%) together.

A subsequent study will present the testing, characterization, and in-depth synthesis results. The MTS apparatus (QTEST 150 machine, MTS, USA) used for the shape memory training and stress recovery testing has a heated chamber. All of the architectures are printed using the open source DLP (Digital Light Processing) advanced manufacturing machine (Bison 1000) at a temperature of 40 °C. To avoid incorrect readings caused by thermal expansions in the fixtures, the chamber is warmed to 75°C, or the solid polymeric glass transition temperature of 70°C, about an hour before the training procedure. The samples are left in the chamber for 30 minutes once it has heated up and reached the rubbery condition. The samples are then crushed using a 15% strain program with a 0.5 mm/min deformation rate. The samples are quickly cooled to normal temperature while maintaining a constant strain, resulting in their compressed shape, once the predetermined strain percentage has been reached. The load is released to give the structure a temporary form once it reaches room temperature. It turns out that all of the designs' shape fixity ratios (Eq. 28) almost invariably are. The samples are then warmed to 75°C while still retaining zero recovery strain, and the elastic stress recovery for every specimen is then determined from the load cell.

$$F = \frac{\varepsilon_f}{\varepsilon_l} \times 100\% \quad (28)$$

where ε_f is the fixed strain after load removal and ε_l is the measured strain before load removal.

7.2. Results

Together with the lattice truss unit cellular architectures taken from chapter 4, section 4, and the ideal lightweight cellular unit architectures presented utilizing the inverse design framework in the preceding sections. For the sake of computational and experimental validation, 3.2 was modeled and 3D printed.

7.2.1 Model validation

For lattice truss architectures and cellular architectures with thin-walls, respectively, numerical comparisons made with the ANSYS simulation tool and experimental comparisons are depicted in Figures 48 and 8. The proposed lattice truss architectures, while still flexural-

dominated, can be found to provide equivalent or even better relative compression strength characteristics than the conventional Octet truss structure. It ought to be underlined that in Figure 48, correlations were finished according to the cross-section designs' bar distances across. Numerous studies demonstrate that the effectiveness of lattice truss architectures is significantly influenced by their relative densities. Figure 48 expects to give a standardized examination across bar measurements, but part 4 previously covered correlations for the indistinguishable ideal cross section architectures with Octet architectures over relative densities. In terms of relative densities, the best lattice truss unit cellular architectures produced in this study still possess superior specific compression strength characteristics. In addition, it is possible to demonstrate in Figure 49 (a) that the ideal cellular architectures with thin-walls outperform hexagonal honeycomb unit cells in terms of compression strength (in-plane direction). The 44 lattices in Figure 48 (b) and the cellular architectures in Figure 49 (b) both have characteristics that are comparable to those of their unit cells. For comparisons with densities of cellular architectures with thin walls, see Figure 50.

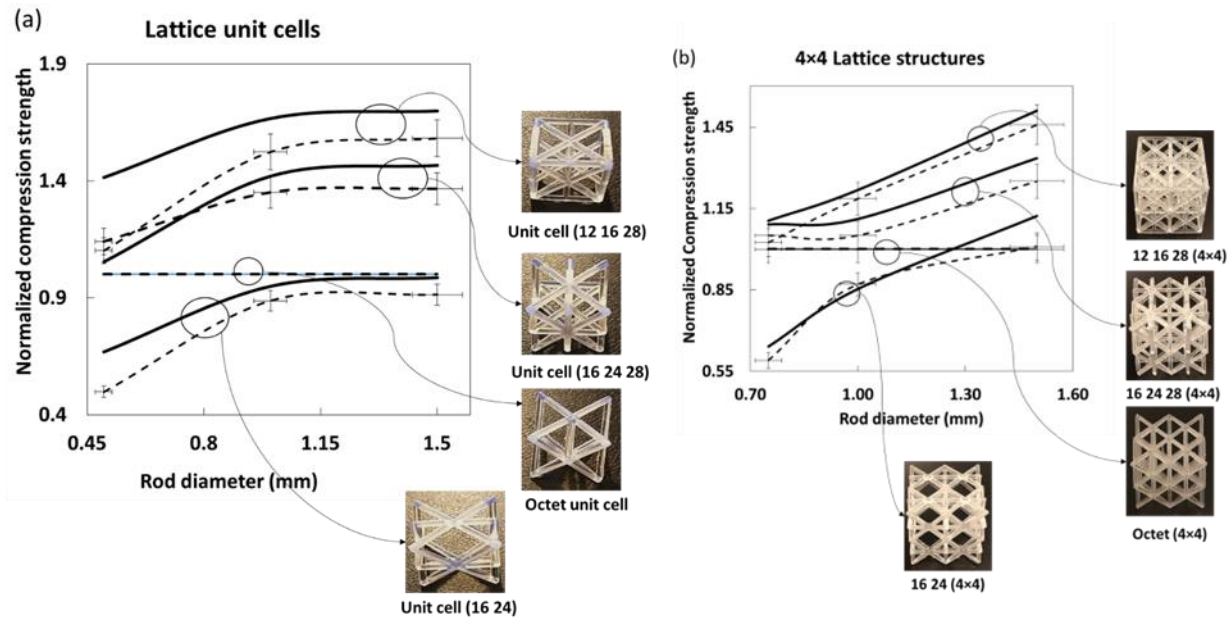


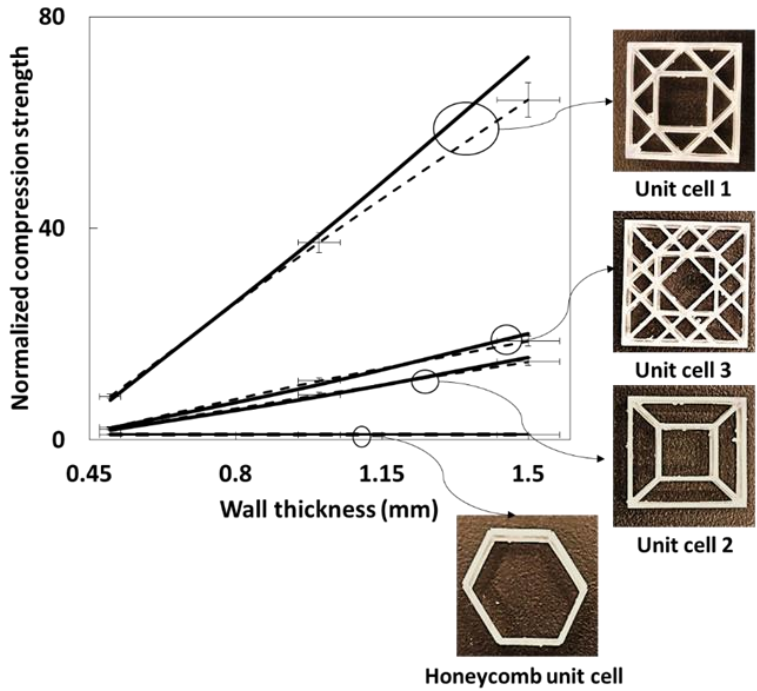
Figure 48. Experimental and numerical comparisons for (a) lattice unit cells, (b) 4x4 lattice cells.

The experiment's standard errors are shown by the thin, solid cross. The narrow circle with the arrow indicates that the same unit ties the experimental and numerical lines cellular. In terms of compression strength, the ideal lattice truss unit cellular architectures (12, 16, 28, and

16-24-28) outperform Octet unit cells in the same overall volume (a). The 4 by 4 lattice truss structures in (b) that were created by using unit cells in (a) can be observed to behave in the same way as their unit cells. The standardized compression strength in this case is calculated as the difference between the compression strengths of each lattice and the cells in an octet unit. The narrow slod cross indicates the experiment error bars. The arrow indicates that the numerical and experimental lines are both part of the same unit cellular, as indicated by the small circle surrounding them. The cellular architectures with thin-walls in (a) (1, 2, and 3) and the four-by-four cellular architectures made from the same unit cellular have significantly better compression strength characteristics than the hexagonal honeycomb structure. The ideal unit cells' superiority is explained by their greater densities and combined connections. The normalized compression strength is the ratio of the compression strengths of individual cellular architectures with thin walls to those of the hexagonal honeycomb structure.

It can be observed from figure 49 that the thin-walled unit cells and lattice thin-walled structures outperformed the honeycomb structure. Since the honeycomb unit cell have comparatively less walls thought the mass is much lower than the optimal unit cells, the strength in the in-plane orientation is much lower. It should be noted that the honeycomb unit cell has excellent out-of-plane load baring properties especially due to its low weight. But in the in-plane orientation, it has much lower strength compared to any other structure in the dataset. It can be observed that the bending dominated thin-walled unit cells optimized through machine learning and correlation analysis optimized inverse design framework are exponentially superior to honeycomb unit cell. In the coming sections more comparison with shape memory effect and stretching dominated optimal unit cells along with bulk polymer shall be presented. All the structures in these comparisons are designed to have same overall volume while the mass changes due to the increase in number of walls and their orientations.

(a)

Thin-walled unit cells

(b)

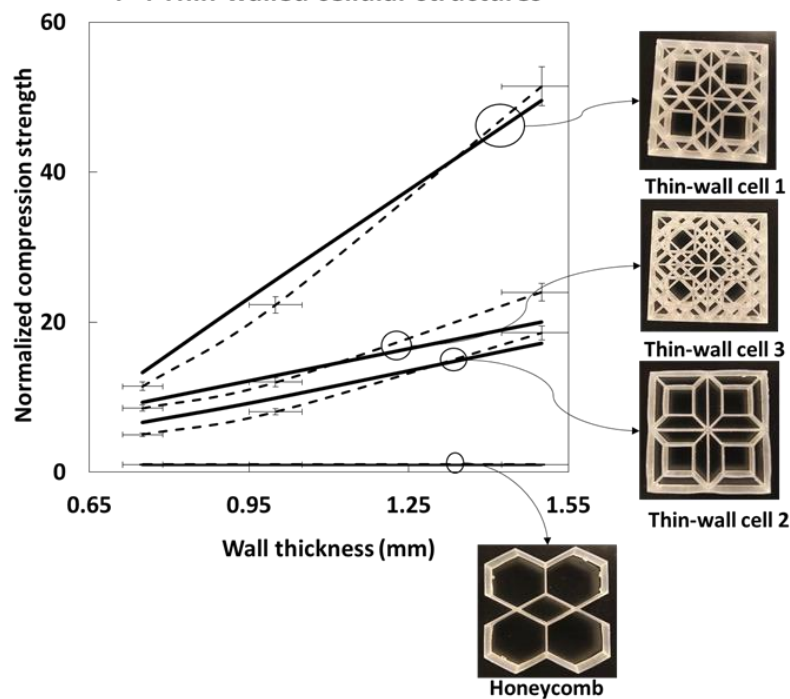
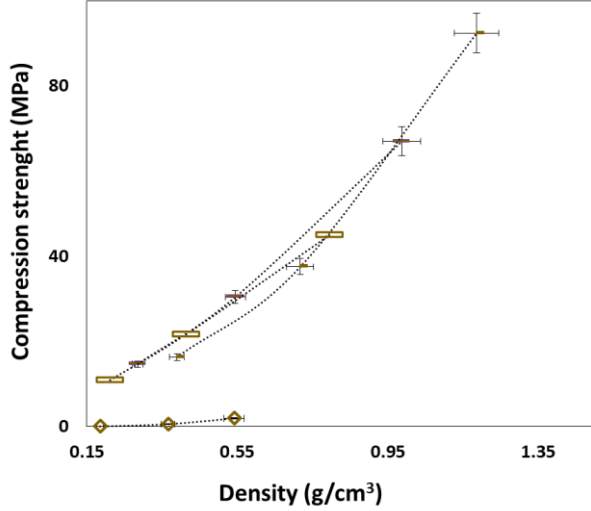
4x4 Thin-walled cellular structures

Figure 49. Numerical and experimental comparisons for (a) cellular architectures with thin-walls, (b) 4×4 cellular architectures with thin-walls under uniaxial compressive tests.

(a)

Density versus Compression strength

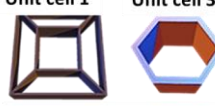


...◊... Honeycomb thin-walled cell (in-plane)

...···... Thin-walled unit cell 1 (in-plane)

...···... Thin-walled unit cell 3 (in-plane)

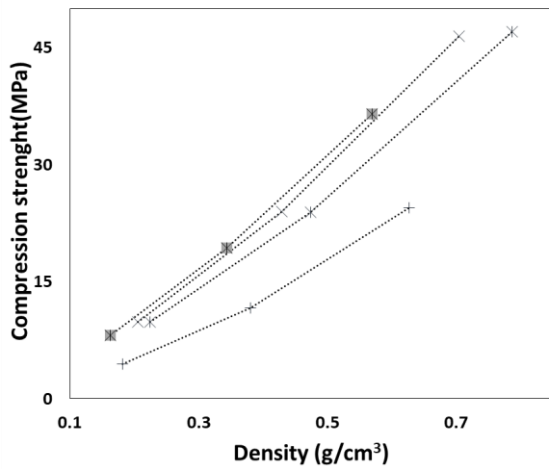
...···... Thin-walled cell 2 (in-plane)



Unit cell 2 Honeycomb unit cell

(b)

Density versus Compression strength



...···... Octet lattice cell

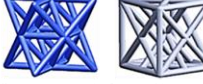
...···... 16 24 28 lattice cell

...···... 16 24 lattice cell

...···... 12 16 28 lattice cell



Unit cell (16 24 28) Unit cell (16 24)



Octet unit cell Unit cell (12 16 28)

Figure 50. Change of compression strength with relative density.

7.2.2. Shape memory analysis

Figures 50 show comparisons between the ideal lattice truss unit cellular structures and the Octet truss lattice, the thin-walled unit cell with the solid samples, and the suggested cellular architectures with hexagonal honeycomb unit cell.

In contrast to Octet unit cells with the same lattice member diameter, the primal predominantly flexural in nature's elements lattice truss unit cellular architectures and 4 by 4 lattice truss architectures, particularly unit cells (12 16 28) and (16 24 28), have 10–30% greater specific elastic stress recovery (elastic stress recovery/overall volume).

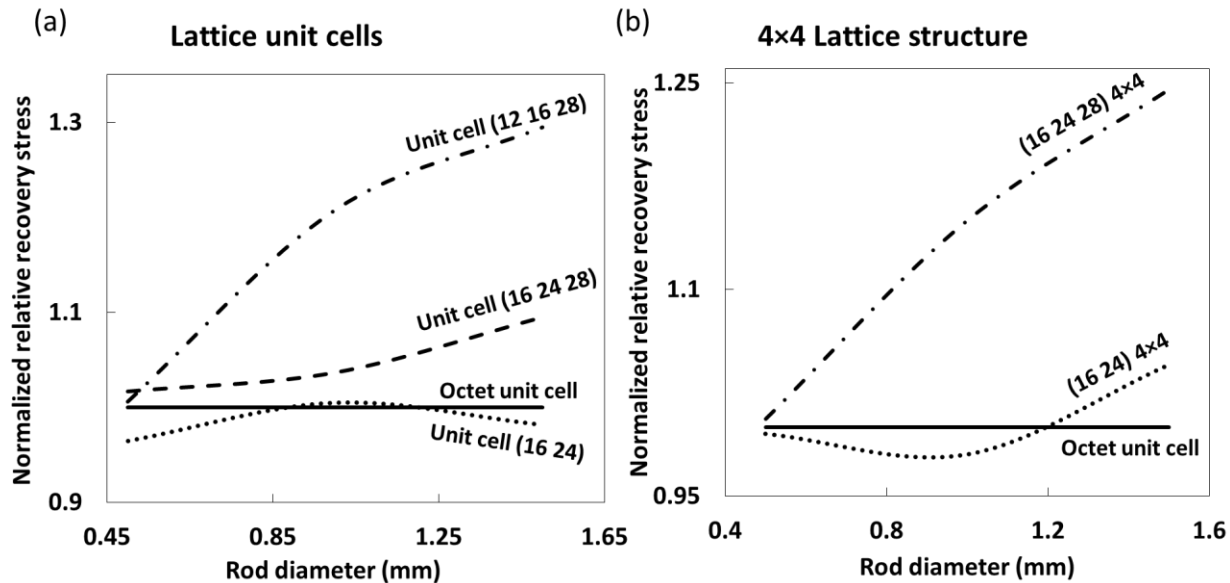


Figure 51. Experimental comparisons for the normalized elastic stress recovery.

The normalized elastic stress recovery in this situation is calculated as the difference between each lattice unit cell's elastic stress recovery and the particular elastic stress recovery of the Octet unit cell under uniform overall volume. When employing a shape memory polymer to 3D print the lattice truss architectures, it can be demonstrated that they have better (by 30%) stress recovery characteristics than the Octet unit cellular.

From Figures 52(a) and 52(b), the elastic stress recovery of the best cellular architectures with thin-walls and 4 by 4 cellular architectures (unit cells 1 and 3) is 200–1000% greater than that of the best hexagonal honeycomb unit cellular and is also 50% greater than that of the best stretching-dominated structure (unit cellular 5). For examples of 3D printed objects, see Figure 53 and Figure S8 for elastic stress recovery vs density).

The ideal cellular architectures with thin-walls can be seen to exhibit 140–200% better elastic stress recovery than the solid structure in Figure 52(c), which compares the mass normalized elastic stress recovery of these two types of materials. The Octet truss lattice unit

cellular and 4 by 4 Octet truss lattice structure are predominantly stretching in nature's elements in nature's elements, it should be mentioned. The behavior of the improvised lattice truss unit cellular architectures is flexural dominated. In comparison to Octet unit cells and 4 by 4 Octet truss lattice truss architectures, the improvised 4 by 4 lattice truss architectures, which are either predominantly flexural in nature's elements or slightly flexural dominated, also show superior elastic stress recovery. Similarly, the improvised cellular architectures with thin-walls and 4x4 cellular architectures, despite being flexural-dominated, still exhibit better elastic stress recovery compared to their predominantly stretching in nature's elements counterparts. This demonstrates that unit cells, which are mostly flexible in nature's components, might be candidates for multifunctional functions including greater strength, stretchability, and recovery stress.

Under uniform overall volume, the normalized elastic stress recovery in this instance is the ratio of each thin-walled structure's specific elastic stress recovery to the hexagonal honeycomb structure's specific elastic stress recovery. The cellular architectures with thin-walls 1 and 3 and the hexagonal honeycomb arrangement were identified as predominantly flexural in nature's elements architectures in this instance. Extending is transcendent in the dainty walled unit cellular number 5. In terms of normalized elastic stress recovery from (a) and (b), the improvised architectures perform significantly better than the hexagonal honeycomb. The elastic stress recovery parameters of the proposed primal predominantly flexural in nature's elements architectures—both the unit cells and the 4 by 4 architectures—are comparable to or even superior to those of the ideal predominantly stretching in nature's elements thin-walled structure.

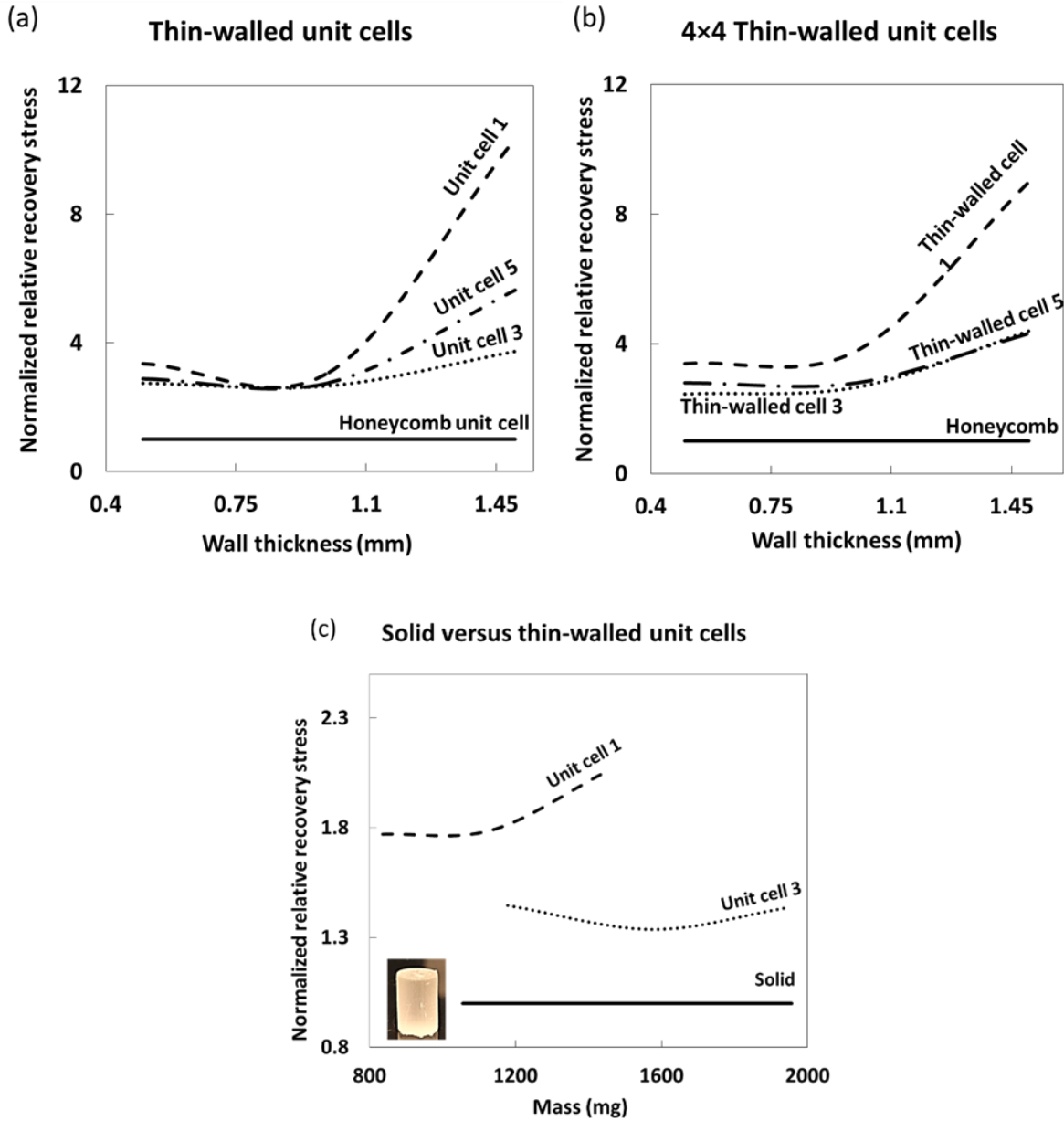


Figure 52. Experimental comparisions for normalized elastic stress recovery.

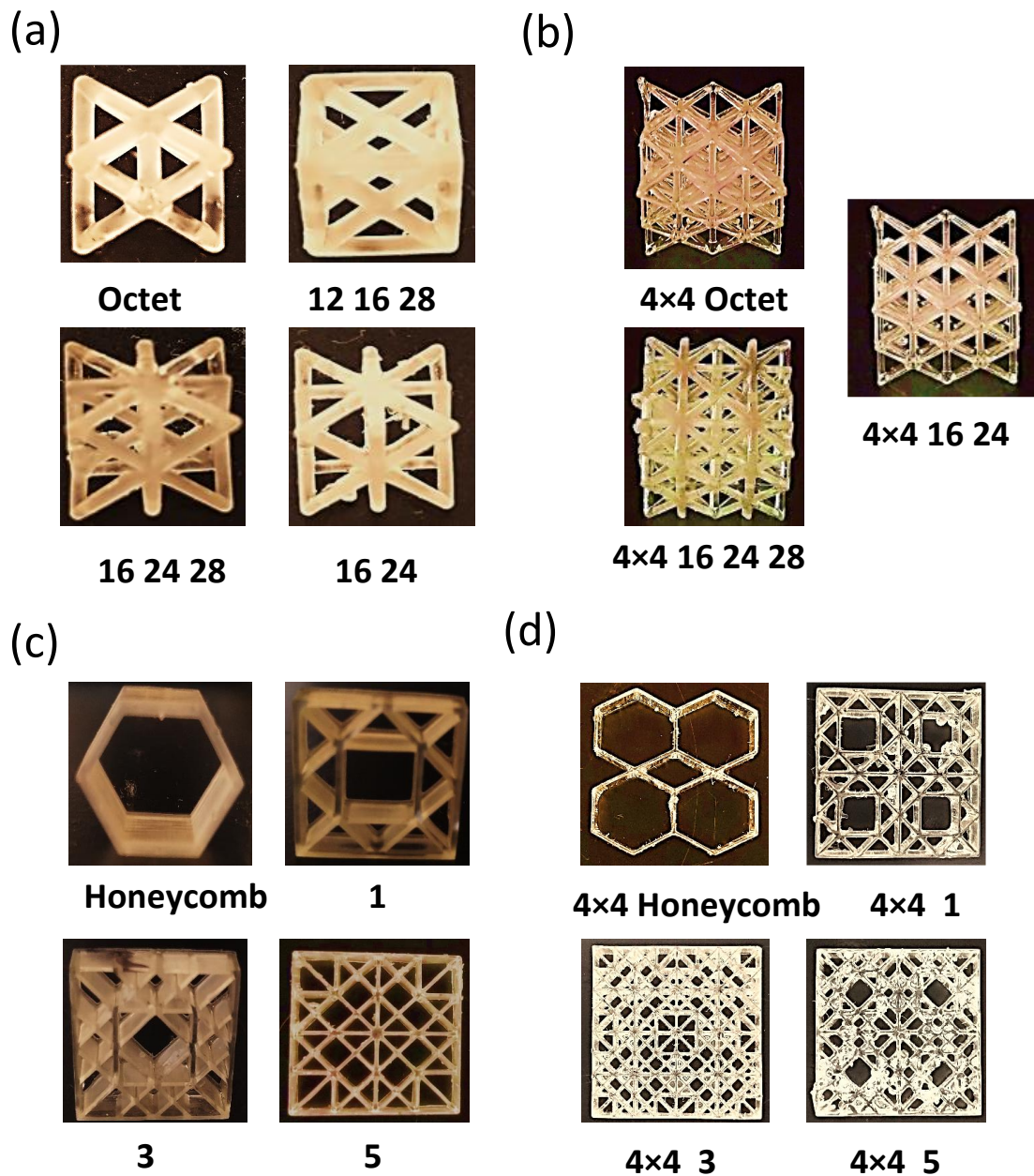


Figure 53. Images of 3D printed cellular architectures.

Because the improvisation procedure is solely based on the architectural behavior of the unit cells, it is important to note that employing various SMPs will have an effect on their architectural performance as well as their impact on shape memory. At room temperature, the SMP utilized in this study is brittle, so there may be fewer total deformations before it breaks. A more ductile SMP can raise the range of deformations that can be utilized to train or program

the architectures. To deliver the preparation Database, our limited component displaying may likewise have to think about the nonlinear way of behaving, viscoelasticity, and viscoelasticity for a more malleable SMP. Since all of the thin-walled cellular unit architectures and lattice truss unit cellular architectures in this study utilized the same brittle SMP for modeling and testing, it is possible that the results will not change if a ductile SMP is utilized instead.

Finally, numerical and experimental analysis performed under uniaxial loading confirm the findings of the earlier studies by showing that predominantly flexural unit cells in nature's elements are flexible and fail mainly due to rod flexural, whereas predominantly stretching unit cells possess greater toughness as well as fail due to component stretching, buckling, or fracture. Due to the element flexural phenomenon, previous research revealed that predominantly flexural in nature's elements architectures are only one third as strong as predominantly stretching in nature's elements architectures. Contrary to this assertion, predominantly flexural in nature's elements unit cells have a relative compression strength within their RVE that is 60% betterer than that of typical Octet units and most predominantly stretching in nature's elements units.

Due to the study's use of Maxwell's criterion and predominantly flexural in nature's elements architectures, some predominantly stretching in nature's elements architectures with greater strength and deformations may have been overlooked. Additionally, it is possible that some lattice configurations that go beyond Maxwell's criterion were overlooked in our research [63, 64].

Chapter 8. Summary

Using biomimicry and machine learning, we look into architectural improvisation to predict new designs with better mechanical and architectural characteristics. Through forward AI relapse, biomimicry poles with unrivaled clasping characteristics were created and refined. A sum of 1500 biomimicry poles were made, and their clasping burden and stress were displayed utilizing ANSYS utilizing the outside shape and inward permeable construction of a few organic frameworks. Following that, some common biomimicry columns were 3D printed and tested to confirm the results of the FE analysis. In order to build a relationship between the buckling capabilities and the fingerprints of the 1,500 inspired by nature columns in the training Database, the bagged ensemble tree approach was used for forward design. Then, 160 new columns were made using machine learning, MATLAB coding, and data filtering to enhance these biomimicry designs. Without significantly increasing stresses, it was designed that the improvised biomimicry columns have buckling loads that are several times greater than those of the conventional solid or hollow cylinders that are frequently utilized in engineering architectures. This study will enable the production of lighter columns with significantly improved buckling load bearing capacity.

A number of previously unknown symmetric, asymmetric, isotropic, and anisotropic lattice truss unit cellular architectures are designed and investigated using machine learning. The amount of computing work and human labor was reduced by machine learning. With the right data management and the right training data sets, it is possible to make reasonable evaluations about the mechanical and architectural characteristics of the ideal lattice truss unit cellular architectures. A subset of the best lattice truss unit cellular architectures are the subject of simulation and experiment-based validations. Compared to octet truss lattice truss unit cellular architectures, symmetric optimum lattice truss unit cellular architectures constructed this way have betterer flexural strengths of 13 to 35 percent and compression strengths of 28 to 67 percent. This study only suggests a subset of the ideal architectures for asymmetric lattice truss unit cellular architectures. The best lattice truss unit cellular architectures were further improvised by including biomimicry columns to improve each cell's capacity to buckle. The study found that when compared to unit cells with solid columns, improved lattice truss unit cellular architectures with biomimicry columns had a 130–160 percent greater relative buckling

capability. The appropriate lattice truss unit cellular architectures can be selected based on the application to produce sandwich panels, uniform lattice truss architectures, and betterer order lattice truss architectures.

Later, a framework for inverse design that is based on machine learning is used to look at a larger spectrum of architectural designs. We suggest novel lattice truss unit cellular structures that beat the octet unit cellular using Generative adversarial networks and forward regression. Under uniaxial compression, the projected unit cells outperform the octet unit cellular by 40–120 percent, as demonstrated by computational and experimental testing. When the improved unit cells were utilized as sandwich cores, the test results and simulations performed well. The inverse design ML framework is able to continuously improvise the lattice truss unit cellular architectures by iteratively utilizing the newly formed unit cells as training data for evaluations of subsequent formations. Various architectural design types can be improved and new architectures with the right combination of mechanical and architectural characteristics can be suggested using this framework. This technique may be used to construct and further improve a variety of biomimetic complex structures with varied properties including stress mitigation, improved flexural or buckling capabilities, and shape recovery. This is supported by the adequate prediction accuracy of the regression models and inverse design framework as well as the excellent performance of the improvised lattice truss unit cellular architectures. These models are utilized to make new complex structures that are more powerful at retaining shocks than their biomimicry partners, like hexagonal honeycomb and other cell architectures.

Using this method, a significant portion of unexplored cellular unit architectures was investigated in order to suggest novel designs with enhanced architectural qualities. The ideal cellular unit architectures suggested by this method have normalized natural frequencies that are 30 to 100 times betterer, load carrying capacities that are 50 to 250 times better, and energy mitigation under impact load that is 300 times better than biomimicry hexagonal honeycomb architectures. The machine learning-designed unit cells are validated using both numerical modeling and experimental testing. An efficient design tool for identifying various kinds of architectures would be provided by the inverse design ML framework. Thin-walled cellular unit architectures and lightweight lattice truss unit cellular architectures are being studied for

improved shape memory characteristics. To further develop the dainty walled unit cells, an extraordinary backwards plan model consolidating AI and connection examination approaches is proposed. To better understand the behavior of lattice truss unit cellular architectures, the Maxwell's criterion for frame stiffness is extended to include cellular architectures with thin walls. the lightweight lattice truss unit cellular architectures and unit cells with thin walls that have primal strength and stretchability.

By ignoring the nearby bowing (or clasping) of flimsy walls, the Maxwell's archetype for firmness of casings is extended to classify slight walled architectures. Because of this, selecting the best cellular architectures with thin walls for flexural was made simpler. The suggested predominantly flexural in nature's elements lattice truss unit cellular architectures have a 30% betterer elastic stress recovery than Octet truss lattice truss unit cellular architectures, which exhibit predominantly stretching in nature's elements behavior. The suggested cellular architectures with thin walls have a normalized specific elastic stress recovery that is up to one hundred times better than that of the hexagonal honeycomb unit cellular in the in-plane direction using the inverse design framework, which is based on Spearman correlation analysis and machine learning prediction models. Figure 10 shows that the cellular architectures with thin walls' elastic stress recovery is up to 200 percent betterer than that of the bulk polymer. The compression strength of these unit cells tends to be comparable, which is used as a screening method for the optimum elastic stress recovery properties. The suggested predominantly flexural in nature's elements unit cells have improved load carrying, elastic stress recovery, and energy mitigation characteristics due to their stretchability. With enough data and control settings, the suggested improvisation framework may be expanded to predict structures with any required mechanical and architectural attributes.

It is important to note that the rod aspect ratios have a significant impact on the complicated mode of deformation experienced by lightweight designs, particularly lattice truss architectures, which can include stretching, buckling, or flexural. Although Maxwell's criterion can be utilized for initial screening, a comprehensive investigation of the lattice behavior is required to fully comprehend the architectural behavior of the lattice under various loading conditions and failure mechanisms. It is important to note that the rod aspect ratios have a

significant impact on the complicated mode of deformation experienced by lightweight constructions, particularly lattice truss architectures, which can include stretching, buckling, or flexural. Although a comprehensive examination of the lattice's behavior under a variety of loading conditions and an investigation into its failure modes are required, Maxwell's criterion can be utilized for preliminary screening.

References

1. Venkayya. V. B. Structural Optimization: A Review and some recommendations. International Journal for Numerical Methods in Engineering, 13, 203-228 (1978).
2. Vanderplaats. G. N. Structural Optimization - Past, Present and Future. Frontiers of Achievement, AIAA-81-0897, (1981).
3. Bendsae. M. P., and Kikuchi. N. Generating optimal topologies in structural design using a homogenization method. Comput. Meth. appl. Mech. Engng. 71,197-224 (1988).
4. Xie. Y. M. and Steven. G. P. A Simple Evolutionary Procedure for Structural Optimization. Computers & Structures Vol. 49, No. 5, pp. W-896. 1993.
5. Tkatchenko, A. Machine learning for chemical discovery. *Nat Commun* **11**, 4125 (2020).
6. Wu, S., Kondo, Y., Kakimoto, Ma. *et al.* Machine-learning-assisted discovery of polymers with high thermal conductivity using a molecular design algorithm. *npj Comput Mater* **5**, 66 (2019).
7. Magoulas G.D., Prentza A. (2001) Machine Learning in Medical Applications. Lecture Notes in Computer Science, vol 2049, ACAI 1999. Springer, Berlin, Heidelberg.
8. V. Sze, Y. -H. Chen, J. Emer, A. Suleiman and Z. Zhang, "Hardware for machine learning: Challenges and opportunities," 2017 IEEE Custom Integrated Circuits Conference (CICC), 2017, pp. 1-8.
9. Challapalli, A., and Li, G. (2020). 3D Printable Biomimetic Rod with superior Buckling Resistance Designed by Machine Learning. *Sci. Rep.* **10**, 20716. doi:10.1038/s41598-020-77935-w
10. Challapalli, A., and Li, G. (2021). Machine Learning Assisted Design of New Lattice Core for Sandwich Structures with Superior Load Carrying Capacity. *Sci. Rep.* **11**, 18552. doi:10.1038/s41598-021-98015-7
11. Challapalli, A., Patel, D., and Li, G. (2021). Inverse Machine Learning Framework for Optimizing Lightweight Metamaterials. *Mater. Des.* **208**, 109937. doi: 10.1016/j.matdes.2021.109937
12. Challapalli, Adithya, Konlan, John Patel, Dhrumil Li, Guoqiang. Discovery of Cellular Unit Cells with High Natural Frequency and Energy Absorption Capabilities by an Inverse Machine Learning Framework, *Front. Mech. Eng.*, 2297-3079, 2021
13. Deshpande, V. S., Fleck, N. A. & Ashby, M. F. Foam topology bending vs stretching dominated architecture. *Acta Mater.* **49**, 1035–1040 (2001).

14. Wen, C. et al. Stiff isotropic lattices beyond the Maxwell criterion. *Sci. Adv.* **5**(9), eaaw1937. (2019).
15. Feng, R., Liu, F. & Xu, W. Topology optimization method of lattice structures based on a genetic algorithm. *Int. J. Steel Struct.* **16**, 743–753 (2016).
16. Moongkhamklang, P., Deshpande, V. S., & Wadley, H. N. G. The compressive and shear response of titanium matrix composite lattice structures. *Acta Materialia* **58**, 2010, 2822–2835.
17. Tobia, M. et al. SLM lattice structures: Properties, performance, applications, and challenges. *Mater. Des.* **183**, 108137. <https://doi.org/10.1016/j.matdes.2019.108137> (2019).
18. Deshpande, V. S., Fleck, N. A. & Ashby, M. F. Effective properties of the octet-truss lattice material. *J. Mech. Phys. Solids* **49**, 1747–1769 (2001).
19. Radek, V., Dane, K., David, P. Impact resistance of different types of lattice structures manufactured by SLM. *MM Sci. J.* **12**, 1579–1585 (2016).
20. Evans, A. G. et al. Concepts for enhanced energy absorption using hollow micro-lattices. *Int. J. Impact Eng.* **37**, 947–959 (2010).
21. Yang, J. S., Ma, L. & Rüdiger, S. Hybrid lightweight composite pyramidal truss sandwich panels with high damping and stiffness efficiency. *Composites Struct.* **148**, 85–96 (2016).
22. Lake, M. S. Stiffness and strength tailoring in uniform space-fling truss structures. NASA TP-3210 (1992).
23. Hill, R. Elastic properties of reinforced solids: some theoretical principles. *J. Mech. Phys. Solids* **11**, 357–372 (1963).
24. Fan, H. L., Jin, F. N. & Fang, D. N. Nonlinear mechanical properties of lattice truss materials. *Mater. Des.* **30**, 511–517 (2009).
25. Challapalli, A., Ju, J. Continuum model for effective properties of orthotropic octet-truss lattice materials. ASME Int. Mech. Eng. Congress Exposition. paper number V009T12A05 (2014).
26. Ullah, I., Elambasseril, J., Brandt, M. & Feih, S. Performance of bio-inspired Kagome truss core structures under compression and shear loading. *Compos. Struct.* **118**, 294–302 (2014).
27. Austermann, J. et al. Fiber-reinforced composite sandwich structures by co-curing with additive manufactured epoxy lattices. *J. Compos. Sci.* **3**, 53 (2019).

28. Xu, G. et al. Response of composite sandwich beams with graded lattice core. *Compos. Struct.* 119, 666–676 (2015).
29. Zhang, G., Ma, L., Wang, B. & Wu, L. Mechanical behavior of CFRP sandwich structures with tetrahedral lattice truss cores. *Compos. B Eng.* 43, 471–476 (2012).
30. L.J. Gibson, M.F. Ashby, *Cellular Solids: Structure and Properties*, (2nd ed.), Cambridge University Press, Cambridge, MA (1997)
31. Qiancheng Zhang, Xiaohu Yang, Peng Li, Guoyou Huang, Shangsheng Feng, Cheng Shen, Bin Han, Xiaohui Zhang, Feng Jin, Feng Xu, Tian Jian Lu, Bioinspired engineering of honeycomb structure – Using nature to inspire human innovation, *Progress in Materials Science*, Volume 74, 2015, Pages 332-400.
32. Ha, N. S., & Lu, G. (2019). A review of recent research on bio-inspired structures and materials for energy absorption applications. *Composites Part B: Engineering*, 107496.
33. Xiyue An, Hualin Fan, Hybrid design and energy absorption of luffa-sponge-like hierarchical cellular structures, *Materials & Design*, Volume 106, 2016, Pages 247-257, ISSN 0264-1275
34. H.H. Tsang, S. Raza, Impact energy absorption of bio-inspired tubular sections with structural hierarchy, *Composite Structures*, Volume 195, 2018, Pages 199-210
35. H.H. Tsang, K.M. Tse, K.Y. Chan, Guoxing Lu, Alan K.T. Lau, Energy absorption of muscle-inspired hierarchical structure: Experimental investigation, *Composite Structures*, Volume 226, 2019, 111250
36. Yu, X., Pan, L., Chen, J. et al. Experimental and numerical study on the energy absorption abilities of trabecular–honeycomb biomimetic structures inspired by beetle elytra. *J Mater Sci* 54, 2193–2204 (2019).
37. Yan Zhang, Liang Gao, Mi Xiao, Maximizing natural frequencies of inhomogeneous cellular structures by Kriging-assisted multiscale topology optimization, *Computers & Structures*, Volume 230, 2020, 106197, ISSN 0045-7949
38. X. Huang, Z.H. Zuo, Y.M. Xie. Evolutionary topological optimization of vibrating continuum structures for natural frequencies, *Computers and Structures* 88 (2010) 357–364
39. Cheng, Q., Zhidong, G., Siyuan, J., Zeng, Li. (2017). A method of determining effective elastic properties of honeycomb cores based on equal strain energy. *Chinese Journal of Aeronautics*, 30, 2.
40. Autar, K., K. Mechanics of Composite Materials. (2006). Taylor & Francis, New York.
41. Akhlesh, L and Raúl J., M. Engineering Biomimicry. Elsevier, 978-0-12-415995-2, 2013.

42. Chen, I.H., Kiang., J.H., Correa, V., Lopez, M.I., McKittrick, J., Meyers, M.A. Armadillo armor: Mechanical testing and micro-structural evaluation. *J. Mech. Behav. Biomed. Mater.*, 4 (5) (2011), pp. 713-722
43. Rawat, P., Zhu, D., Rahman, M.Z., Barthelat, F. Structural and mechanical properties of fish scales for the bio-inspired design of flexible body armors: A review. *Acta Biomaterialia*, Volume 121, February 2021, Pages 41-67.
44. Solga, A., Cerman, Z., Striffler, B. F., Spaeth, M. & Barthlott, W. The dream of staying clean: lotus and biomimetics surfaces. *Bioinspir. Biomim.* 2, 126–134 (2007).
45. Yang, X., Ma, J., Shi, Y., Sun, Y., Yang, J. Crashworthiness investigation of the bio-inspired bi-directionally corrugated core sandwich panel under quasi-static crushing load. *Materials and Design*, Volume 135, 5 December 2017, Pages 275-290.
46. Koch, K., Bhushan, B. & Barthlott, W. Multifunctional surface structures of plants: an inspiration for biomimetics. *Progr. Mater. Sci.* 54, 137–178 (2009).
47. Sze, T.-K.J. Design, and modeling of a light powered biomimicry micropump. *J. Micromech. Microeng.* 25, 065009 (2015).
48. Al-Arabe, K. & Knopf, G. K. Photo responsive hydrogel microvalve activated by bacteriorhodopsin proton pumps. *Proc. SPIE* 7646, 764611 (2010).
49. Manas, S., Jintu, F., Szeto, Y. C. & Tao, X. Biomimetics of plants structures in textile fabrics for the improvement of water transportation properties. *Text. Res. J.* 79, 657–668 (2009).
50. Mazzolai, B., Beccai, L. & Mattoli, V. Plants as model in biomimetics and bio robotics: new perspectives. *Bioeng. Biotechnol.* 2, 2 (2014).
51. Sebastian, F. et al. Pummelos as concept generators for biomimetically inspired low weight structures with excellent damping properties. *Adv. Eng. Mater.* 12, B658–B663 (2010).
52. Tavsan, F. & Sonmez, E. Biomimicry in furniture design. *Soc. Behav. Sci.* 197, 2285–2292 (2015).
53. Li, S. H., Zeng, Q. Y., Xiao, Y. L., Fu, S. Y. & Zhou, B. L. Biomimicry of bamboo bast fibers with engineering composite materials. *Mater. Sci. Eng.* 3, 125–130 (1995).
54. Yang, Q., Fan, J. & Li, G. Artificial muscles made of chiral two-way shape memory polymer fibers. *Appl. Phys. Lett.* 109, 183701 (2016).
55. Fan, J. & Li, G. High performance and tunable artificial muscle based on two-way shape memory polymer. *RSC Adv.* 7, 1127–1136 (2017).

56. Singh, K. & Li, G. Buckling of functionally graded and elastically restrained non-uniform columns. *Compos. B Eng.* 40, 393–403 (2009).
57. Wen, C. et al. Stiff isotropic lattices beyond the Maxwell criterion. *Sci. Adv.* 5(9), eaaw1937. <https://doi.org/10.1126/sciadv.aaw1937> (2019).
58. Thomas, T. D. & Dirk, M. Elastically isotropic truss lattice materials of reduced plastic anisotropy. *Int. J. Solids Struct.* 138, 24–39 (2018).
59. Messner, M. C. Optimal lattice-structured materials. *J. Mech. Phys. Solids* 96, 162–183 (2016).
60. Yang, C. X. & Li, Q. M. Advanced lattice material with high energy absorption based on topology optimization. *Mech. Mater.* 148, 103536 (2020).
61. Yang, Y. H., Zhao, L. B., Qi, D. X., Shan, M. J. & Zhang, J. Y. A fuzzy optimization method for octet-truss lattices. *Rapid Prototyp. J.* 25, 1525–1535 (2019).
62. Nasrullah, A. I. H., Santosa, S. P. & Dirgantara, T. Design and optimization of crashworthy components based on lattice structure configuration. *Structures* 26, 969–981 (2020).
63. Watts, S. Elastic response of hollow truss lattice micro-architectures. *Int. J. Solids Struct.* 206, 472–654 (2020).
64. Song, J. et al. Octet-truss cellular materials for improved mechanical properties and specific energy absorption. *Mater. Design* 173, 107773 (2019).
65. Huang, J., Zhang, Q., Scarpa, F., Liu, Y., and Leng, J. (2018). Multi-stiffness Topology Optimization of Zero Poisson's Ratio Cellular Structures. *Composites Part B: Eng.* 140, 35–43. doi: 10.1016/j.compositesb.2017.12.014
66. Kim, B., Lee, S., and Kim, J. (2020). Inverse Design of Porous Materials Using Artificial Neural Networks. *Sci. Adv.* 6, eaax9324. doi:10.1126/sciadv. aax9324
67. Lu, Y., and Tong, L. (2021). Concurrent Topology Optimization of Cellular Structures and Anisotropic Materials. *Comput. Structures* 255, 106624. doi: 10.1016/j.compstruc.2021.106624
68. Zhang, Y., Gao, L., and Xiao, M. (2020). Maximizing Natural Frequencies of Inhomogeneous Cellular Structures by Kriging-Assisted Multiscale Topology Optimization. *Comput. Structures* 230, 106197. doi: 10.1016/j.compstruc.2019.106197
69. S. Wu, Y. Kondo, Ma. Kakimoto, et al. Machine-learning-assisted discovery of polymers with high thermal conductivity using a molecular design algorithm. *npj Comput. Mater.*, 5 (2019), p. 66

70. A. Tkatchenko. Machine learning for chemical discovery. *Nat. Commun.*, 11 (2020), p. 4125
71. C.-T. Chen, G.X. Gu. Generative deep neural networks for inverse materials design using backpropagation and active learning. *Adv. Sci.*, 7 (2020), p. 1902607
72. C. Yan, X. Feng, C. Wick, A. Peters, G. Li. Machine learning assisted discovery of new thermoset shape memory polymers based on a small training dataset. *Polymer*, 214 (2021), Article 123351
73. M. Aru, P. Ghanshyam, D.H. Tran, L. Turab, R. Rami. Machine learning strategy for accelerated design of polymer dielectrics. *Sci. Rep.*, 6 (2016), p. 20952
74. L. Liang, M. Liu, C. Martin, W. Sun. A deep learning approach to estimate stress distribution: a fast and accurate surrogate of finite-element analysis. *J. R. Soc. Interface*, 15 (2018), p. 20170844
75. Z. Qi, N. Zhang, Y. Liu, W. Chen. Prediction of mechanical properties of carbon fiber based on cross-scale FEM and machine learning. *Compos. Struct.*, 212 (2019), pp. 199–206
76. G. Capuano, J. Julian. Smart finite elements: a novel machine learning application. *Comput. Methods Appl. Mech. Eng.*, 345 (2019), pp. 363–384
77. Aru, M., Ghanshyam, P., Tran, D. H., Turab, L. & Rami, R. Machine learning strategy for accelerated design of polymer dielectrics. *Sci. Rep.* 10, 20952 (2016).
78. Cao, Y. F., Wu, W., Zhang, H. L. & Pan, J. M. Prediction of the elastic modulus of self-compacting concrete based on SVM. *Trans. Technol. Publ.* 357, 1023–1026 (2013).
79. Chen, H., Qian, C., Liang, C. & Kang, W. An approach for predicting the compressive strength of cement-based materials exposed to sulfate attack. *PLoS ONE* 13, 0191370 (2018).
80. Qi, Z., Zhang, N., Liu, Y. & Chen, W. Prediction of mechanical properties of carbon fiber based on cross-scale FEM and machine learning. *Compos. Struct.* 212, 199–206 (2019).
81. Capuano, G. & Julian, J. Smart finite elements: a novel machine learning application. *Comput. Methods Appl. Mech. Eng.* 345, 363–384 (2019).
82. Matrinez, F., Moreno, M. J., Matrinez, M., Solves, J. A. & Loreta, D. A finite element-based machine learning approach for modeling the mechanical behavior of the breast tissues under compression in real-time. *Comput. Biol. Med.* 90, 116–124 (2017).
83. Wilt, J. K., Yang, C. & Gu, G. X. Accelerating auxetic metamaterial design with deep learning. *Adv. Eng. Mater.* 22, 1901266 (2020).

84. Kumar, S., Tan, S. & Zheng, L. Inverse-designed spinodoid metamaterials. *NPJ Comput. Mater.* 6, 73 (2020).
85. Ma, W., Cheng, F. & Liu, Y. Deep-learning-enabled on-demand design of chiral metamaterials. *ACS Nano* 12, 646–6334 (2018).
86. ASTM International (D695–15). Standard Test Method for Compressive Properties of Rigid Plastics (ASTM, West Conshohocken, 2015).
87. Smola, A. & Vishwanathan, S. V. N. *Introduction to Machine Learning* (Cambridge University Press, Cambridge, 2010).
88. Huang, X., Zuo, Z. H., and Xie, Y. M. (2010). Evolutionary Topological Optimization of Vibrating Continuum Structures for Natural Frequencies. *Comput. Structures* 88, 357–364. doi: 10.1016/j.compstruc.2009.11.011
89. Vapnik, V. (1995). *The Nature of Statistical Learning Theory*. Springer, New York.
90. Rasmussen, C. E., Williams, C. K. I. (2006). *Gaussian Processes for Machine Learning*. MIT Press. Cambridge, Massachusetts.
91. Christensen, T., Loh, C., Picek, S., Jakobović, D., Jing, L., Fisher, S., Ceperic, V., Joannopoulos, J.D., Soljačić, M. Predictive and generative machine learning models for photonic crystals. *Nanophotonics*, Volume 9, Issue 13, 1 October 2020, Pages 4183-4192
92. Dan, Y., Zhao, Y., Li, X., Li, S., Hu, M., Hu, J. Generative adversarial networks (GAN) based efficient sampling of chemical composition space for inverse design of inorganic materials, *npj Computational Materials*, Volume 6, Issue 1, 1 December 2020, Article number 84.
93. Dong, y., Li, D., Zhang, C., Wu, C., Wang, H., Xin, M., Cheng, J., Lin, J. Inverse design of two-dimensional graphene/h-BN hybrids by a regression and conditional GAN. *Carbon*, Volume 169, 2020, Pages 9-16, ISSN 0008-6223.
94. Tibbits, S., 4D printing: multi-material shape change. *Architectural Design* 84, 116-121, (2014).
95. Khoo Z.X., Teoh J.E.M., Liu Y., Chua C.K., Yang S., An J., Leong K.F., Yeong W.Y., 3D printing of smart materials: A review on recent progresses in 4D printing. *Virtual and Physical Prototyping* 10, 103-122, (2015).
96. Regehly, M., Garmshausen, Y., Reuter, M. et al. Xolography for linear volumetric 3D printing. *Nature* 588, 620–624 (2020).
97. Kelly B.E., Bhattacharya, I., Heidari H., Shusteff M., Spadaccini C., Taylor H., Volumetric additive manufacturing via tomographic reconstruction. *Science* 363, 2019, 1075–1079.

98. Liu Y., Du H., Liu L., Leng J., Shape memory polymers and their composites in aerospace applications: a review. *Smart Materials and Structures* 23, 2014, 023001.
99. Lan X., Liu Y., Lv H., Wang X., Leng J., Du S., Fiber reinforced shape-memory polymer composite and its application in a deployable hinge. *Smart Materials and Structures* 18, 2009, 024002.
100. Li G., Nettles D., Thermomechanical Characterization of a Shape Memory Polymer Based Self-Repairing Syntactic Foam. *Polymer* 51, 2010, 755-762.
101. Li G., Uppu N., Shape Memory Polymer Based Self-Healing Syntactic Foam: 3-D Confined Thermomechanical Characterization. *Composites Science and Technology* 70, 2010, 1419-1427.
102. Lai, S. M., Lan, Y. C., Shape memory properties of melt-blended polylactic acid (PLA)/thermoplastic polyurethane (TPU) bio-based blends. *Journal of Polymer Research* 20, 2013, 140.
103. Soleyman, E. et al., *Smart Materials and Structures* 31, 2022, 085002.
104. Hashmi S.A.R., Prasad H.C., Abishera R., Bhargaw H.N., Naik A., Improved recovery stress in multi-walled-carbon-nanotubes reinforced polyurethane. *Materials and Design* 67, 2015, 492-500.
105. Koerner H., Price G., Pearce N.A., Alexander M., Vaia R.A., Remotely actuated polymer nanocomposites—stress-recovery of carbon-nanotube-filled thermoplastic elastomers. *Nature Materials* 3, 2004, 115.
106. Fan J., Li G., High Enthalpy Storage Thermoset Network with Giant Stress and Energy Output in Rubbery State. *Nature Communications* 9, 2018, 642.
107. Feng, X., and Li, G., High-Temperature Shape Memory Photopolymer with Intrinsic Flame Retardancy and Record-High Recovery Stress. *Applied Materials Today* 23, 2021, 101056.
108. Keshavarzan M., Kadkhodaei M., Forooghi F., An investigation into compressive responses of shape memory polymeric cellular lattice structures fabricated by vat polymerization additive manufacturing. *Polymer Testing* 91, 2022, 106832.
109. Li, A., Challapalli, A. & Li, G. 4D printing of recyclable lightweight architectures using high recovery stress shape memory polymer. *Scientific Reports* 9, 2019, 7621.
110. Yang, C., Boorugu, M., Dopp, A., Ren, J., Martin, R., Han, D., Choi, W., Lee, H., 4D Printing Reconfigurable, Deployable and Mechanically Tunable Metamaterials. *Materials Horizon* 6, 2019, 1244-1250.

111. Ming, L., Wei, H., Zeang, Z., Craig, H., Mingji, C., Haibao, L., and Jerry, H., 3D Printing of Auxetic Metamaterials with Digitally Reprogrammable Shape. *ACS Applied Materials & Interfaces* 11, 2019, 22768-22776.
112. Berwind, M.F., Kamas, A., Eberl, C., A Hierarchical Programmable Mechanical Metamaterial Unit Cell Showing Metastable Shape Memory. *Advanced Engineering Materials* 20, 2018, 1800771.
113. Matheus, B. F., Luiz, J. P., Guilherme, A. O., Lucas, R. S., Sebastião, S. C., Guilherme, F. G. A review on the energy absorption response and structural applications of auxetic structures, *Mechanics of Advanced Materials and Structures*, 2021, 1537-6494.
114. Matheus, B. F., Luiz, J. P., Guilherme, A. O., Sebastião, S. C., Guilherme, F. G. Multi-objective design optimization of double arrowhead auxetic model using Lichtenberg algorithm based on meta-modelling, *Structures* 45, 2022, 1199-1211.
115. Ju, J., Summers, J.D., Compliant hexagonal periodic lattice structures having both high shear strength and high shear strain. *Materials & Design* 32, 2011, 512-524.
116. Evans, A. G., Hutchinson, J. W. Ashby, M. F., Multifunctionality of cellular metal systems. *Progress in Materials Science* 43, 1998, 171–221.
117. Heo, H., Ju, J., Kim, D., Compliant cellular structures: Application to a passive morphing airfoil. *Composite Structures* 106, 2013, 560-569.
118. Li, G., Wang, A., Cold, Warm, and Hot Programming of Shape Memory Polymers. *Journal of Polymer Science Part B: Polymer Physics* 54, 2016, 1319-1339.
119. Zhang, P., Heyne, M.A., To, A.C., Biomimetic staggered composites with highly enhanced energy dissipation: Modeling, 3D printing, and testing. *Journal of the Mechanics and Physics of Solids* 83, 2015, 285-300.
120. Panda, B., Leite, M., Biswal, B. B., Niu, X., & Garg, A, Experimental and numerical modelling of mechanical properties of 3D printed honeycomb structures. *Measurement* 116, 2018, 495–506.
121. Sha, Y., Jian, L., Haoyu, C., Robert, O. R., Jun, X., Design and strengthening mechanisms in hierarchical architected materials processed using additive manufacturing. *International Journal of Mechanical Sciences* 149, 2018, 150-163.
122. Tan, X. P., Tan, Y.J., Chow, C.S.L., Tor, S.B., Yeong, W.Y., Metallic powder-bed based 3D printing of cellular scaffolds for orthopedic implants: A state-of-the-art review on manufacturing, topological design, mechanical properties, and biocompatibility. *Science and Engineering C* 76, 2017, 1328-1343.

123. Gang, Z., Wenlong, D., Jing, T., Jingshou, L., Yang, G., Siyu, S., Ruyue, W., Ning, S., Spearman rank correlations analysis of the elemental, mineral concentrations, and mechanical parameters of the Lower Cambrian Niutitang shale: A case study, Journal of Petroleum Science and Engineering (Part C) 208, 2022, 109550.
124. Lin, W. T., Wu, Y. C., Cheng, A., Chao, S. J., & Hsu, H. M., Engineering Properties and Correlation Analysis of Fiber Cementitious Materials. Materials 7, 2014, 7423–7435.
125. Tummala, R., Predictive Modeling of FMOL Health System Utilization Using Machine Learning Algorithms and Retrospective Study of COVID Tested Patients, LSU Master's Theses, 2021.
126. Challapalli, A., Konlan, J., Li, G., Inverse Machine Learning Discovered Metamaterials with Record High Recovery Stress. International Journal of Mechanical Sciences, 108029, 2022, 0020-7403. <https://doi.org/10.1016/j.ijmecsci.2022.108029>.

Vita

Adithya Challapalli is a graduate student, anticipated to graduate from the Engineering Science department at Louisiana State University, Baton Rouge by January 2023. His major area of concentration is in lightweight architectural design and improvisation using novel data driven tools. Adithya have extensive knowledge and experience in the implementation of biomimicry, machine learning, inversion design, additively manufacturing and experimental comparisons for architectural improvisation. His work has been published in several international journals as research articles and book chapters. Prior to his PhD, Adithya went to University of North Texas for his master's in mechanical and Energy Engineering and got his bachelor's degree in mechanical engineering from Acharya Nagarjuna University, India. Adithya have keen interest in design and implementation of smart strategies to explore complex architectural architectures.